ABSTRACT

Title of Dissertation:	SI3N4/SIO2 ARRAYED WAVEGUIDE GRATINGS AND PEROVSKITE BASED SOLAR CELLS
	Wei-Lun Hsu, Doctor of Philosophy, 2023
Dissertation Directed By:	Professor Mario Dagenais, Department of Electrical and Computer Engineering

In the first part of this thesis, we discuss the design and fabrication of arrayed waveguide gratings implemented on the Si_3N_4/SiO_2 integration platform. Arrayed waveguide gratings (AWGs) are widely applied in telecommunication systems as multiplexers/demultiplexers and signal routers, as well as in optical sensing, quantum computing and spectroscopy. It is believed to be a promising solution to some major challenges in observational astronomy. Our AWG design and devices are based on 100-nm Si_3N_4 on SiO_2 platform. Three-stigmatic-point (TSP) AWGs are designed and demonstrated to feature flat output image surface, which can be cleaved to apply cross-dispersion optics for astronomical observation. V-shaped and crossover structures have been introduced. A V-shaped structure is based on the structure used in Rsoft while the crossover structure overlaps two free spectral range (FSRs) and shorten the lengths of arrayed waveguides. For a lower resolving power design with V-shaped structure, the peak transmission reaches -1.9 dB and the highest resolving power is around 5,300. For

the higher resolving power design with crossover structure, the peak transmission is -2.0 dB and the maximum resolving power goes above 18,000. The performance of all three input channels is very consistent despite prominent side lobes due to larger phase error. The degradation of resolving power within one FSR is only 6%.

A cascaded AWG is developed to broaden the FSR without increasing the footprint. The design approach used in the project is a small primary AWG with broad FSR and multiple large secondary AWGs. However, the cascaded AWGs require a flat response for the primary AWG (flat-top AWG) to prevent large losses at the outer channels as well as at the position of the channel cross-points. The design of flat-top primary AWG is based on modifying the power profile along the input aperture and the phase distribution along the output aperture, creating a sinc function as input signal into the output FPR.

A three stigmatic point (TSP) AWG is used as the secondary AWG for achieving better cross-dispersion performance. One-top-hat or two-top-hat layouts are utilized in the design. Experimental results demonstrate that the Rowland primary AWG has higher peak transmission but suffer significant loss at the channel cross-points while a flat-top primary AWG features slightly lower peak transmission but has a huge improvement at the channel cross-points, improving significantly in transmission by more than 12 dB experimentally. However, phase errors generate prominent side lobes and deteriorate the crosstalk. A cascaded AWG with a flat-top primary stage shows a flat output response within the passband, but Rowland primary AWG performs better in terms of filtering out unwanted signals outside the passband.

In part 2 of this thesis, we present our work on realizing high performance perovskite based solar cells.

A $FA_xMA_{(1-x)}PbI_3$ perovskite solar cell with a tunable bandgap from 1.59 to 1.50 eV is proposed. A superstrate configuration with an inverted planar structure is adopted. The structure of our $FA_xMA_{(1-x)}PbI_3$ perovskite solar cell is FTO glass/PTAA with m-MTDATA/Perovskite/PCBM/Ag. Sequential PTAA doping and solvent-assisted annealing techniques are used to improve the performance of $FA_xMA_{(1-x)}PbI_3$ perovskite solar cell.

SEM images clearly show that $MAPbI_3$ (x=0) film has the highest degree of crystallinity with an average grain size over 2 μm. As the FAI proportion increases, the degree of crystallinity decreases, resulting in smaller grain size. $FA_{0.33}MA_{0.67}PbI_3$ perovskite material is the optimized ratio for single-junction solar cell and the corresponding power conversion efficiency (PCE) is 16.5%, with an open circuit voltage (V_{oc}) of 1.02 V and a short-circuit current (J_{sc}) of 24.5 mA/cm^2. A fill factor (FF) of 66% is extracted and it reflects a lower crystallinity. The external quantum efficiency (EQE) of $FA_{0.33}MA_{0.67}PbI_3$ perovskite solar cell is measured to be above 90% of efficiency over a broad spectral range from 400 to over 600 nm and remains above 80% around 760 nm, and the absorption onset is pushed to 820 nm due to a lower optical bandgap of 1.54 eV.

$MAPbI_3$ solar cell with optical bandgap of 1.59 eV is a great fit as the top cell paired with copper indium selenide (CIS) bottom cell with bandgap of 1 eV. A four-terminal perovskite-CIS tandem solar cell is proposed. I-V characteristics and EQE are taken to investigate the performance. The champion cell demonstrates a PCE of 19.5%

which improves the optimized single-junction $FA_{0.33}MA_{0.67}PbI_3$ perovskite solar cell by 3%. If a freshly fabricated bottom CIS solar cell was used for tandem solar cell, the overall PCE would be expected to be above 20%.

SI3N4/SIO2 ARRAYED WAVEGUIDE GRATINGS AND PEROVSKITE BASED SOLAR CELLS

by

Wei-Lun Hsu

Dissertation submitted to the Faculty of the Graduate School of the
University of Maryland, College Park, in partial fulfillment
of the requirements for the degree of
Doctor of Philosophy,
2023

Advisory Committee:
Professor Mario Dagenais, Chair/Advisor
Professor Martin Peckerar,
Professor Yanne Chembo,
Professor Avik Dutt,
Professor Sylvain Veilleux, Dean's Representative

Acknowledgements

During my years at the University of Maryland, I have been extremely lucky to work with some talented people. The environment has inspired me and supported me along this journey which is filled with challenges and fulfillment. First of all, I would like to express my greatest gratitude to my advisor, Prof. Mario Dagenais, for his guidance and support. His encouragement continually propels me to investigate deeper into my research. His strong aspiration to make meaningful contributions to the field of photonics and photovoltaics has triggered my enthusiasm to a greater degree. Even during some challenges, he has granted me some time and space to recalibrate and offered me opportunities to perform. In addition, he has guided me to have a positive attitude towards life and keep a sense of humor which has helped me build up a stronger and tougher mindset through difficulties and adversities. I would also like to give my sincere appreciation to Prof. Sylvain Veilleux from the department of astronomy. His expert guidance, insightful advice, and constructive critique from the perspective of an astronomical scientist have profoundly helped my research toward its intended objectives.

Besides my advisor, Prof. Mario Dagenais, I would also like to thank the members of my proposal defense committee for their time and advice, namely Prof. Martin Peckerar, and the late Prof. Christopher Davis. Their suggestions have led me to a better understanding of the fundamentals. In addition, I would like to extend my appreciation to the members of my dissertation defense committee, Prof. Martin

Peckerar, Prof. Yanne Chembo and Prof. Avik Dutt, along with Prof. Sylvain Veilleux and Prof. Dagenais for providing constructive feedback and criticism to my thesis.

My gratitude also goes to all my colleagues for their feedback from our group meetings and discussions in the office. The supportive and encouraging environment in the office has allowed me to work more productively. Dr. Jiahao Zhan led me into arrayed waveguide gratings, showing me the fabrication procedure and the design background. I have collaborated with Dr. Yangyi Yao on perovskite solar cells. We proposed a sequential doping technique and modified solvent-assisted annealing technique. Dr. Yang Zhang provided his CIS solar cell as a bottom cell paired with my perovskite top cell. His knowledge in photonics devices has always inspired me to innovate and corrected my errors in a timely fashion. Our discussions have covered everything from simulation software, fabrication tips to device designs and characterization techniques. His generosity to share his experiences and suggestions has motivated me to think further and explore more.

Then, I would like to thank the engineers in UMD NanoCenter, including Dr. John Abraham, Dr. Thomas Loughran, Dr. Mark Lecates, Dr. Jonathan Hummel and Dr. Nam Kim from Fablab, Dr. Sz-Chian Liou from AIMLab, Dr. Zhiwei Peng from NanoChemLab, and Dr. Peter Zavalij from X-ray Crystallographic Center as well, for their precious time and effort in the fabrication and characterization of my samples. Their generosity to share their experience in fabrication and characterization paves a smoother way for my research. In addition, this work cannot be done without the support by the National Science Foundation under grant 1711377 and National

Aeronautics and Space Administration under grant 16-APRA 16-0064 and 21-APRA 21-0116.

And last, I am grateful to my family for their endless support, especially during my struggling time. I cannot imagine how life would be without their support. This journey so far has taught me how to face challenges and solve problems, as well as how to collaborate with others, and coordinate a team. I am extremely grateful for what I have got. Thank you.

Table of Contents

List of Tables

List of Figures

List of Publications

- Y. Zhang, W.-L. Hsu, P. Gatkine, S. Veilleux and M. Dagenais, "High Resolving Power Arrayed Waveguide Grating with Spiral Reusable Delay Lines (SRDL-AWG)," 2023 CLEO: Conference on Lasers and Electro-Optics, SW30.4, San Jose, California, May. 7-12, 2023.

  (Collaborating with Dr. Yang Zhang; discussing the SRDL AWG design and providing suggestions)

- W.-L. Hsu, J. Zhan, Y. Zhang, S. Veilleux and M. Dagenais, "Simulation, Fabrication and Characterization of a Si_3N_4 based Three Stigmatic Point Array Waveguide Grating with Multiple Input Channels by Using Aberration Theory," 2023 IEEE Silicon Photonics Conference, FC-5, Arlington, Virginia, Apr. 4-7, 2023.

  (Collaborating with Dr. Jiahao Zhan from design to simulation, and contributing to all of fabrication and characterization)

- J. Zhan, Y. Zhang, W.-L. Hsu, S. Veilleux, and M. Dagenais, "Design and Implementation of a Si_3N_4 Three-Stigmatic-Point Arrayed Waveguide Grating with a Resolving Power over 17,000," Opt. Express, vol. 31, no. 4, pp. 6389, 2022.

  (Collaborating with Dr. Jiahao Zhan from design to simulation as well as contributing to all of fabrication and characterization of the AWG with resolving power over 17k)

- Y. Yao, W.-L. Hsu, M. Dagenais “High Efficiency Perovskite Solar Cells with Sequentially Doped PTAA,” IEEE Journal of Photovoltaics, vol. 9, no. 4, pp. 1025, 2019.

  (Collaborating with Dr. Yangyi Yao to develop sequential doped PTAA and modifying solvent-assisted annealing technique, as well as fabricating and characterizing the solar cell performance)

- Y. Yao, W.-L. Hsu, M. Dagenais “High Efficiency Perovskite Solar Cells by a Modified Low-Temperature Solution Process Inter-Diffusion Method,” 44th IEEE Photovoltaic Specialist Conference, District of Columbia, 2017.

  (Collaborating with Dr. Yangyi Yao to develop the whole fabrication technique, as well as contributing to half of fabrication and characterization of the solar cell)

- Y. Liang, Y. Yao, W.-L. Hsu, M. Dagenais and I. Takeuchi, "Fabrication of organic-inorganic perovskite thin films for planar solar cells via pulsed laser deposition,” AIP Advances, vol. 6, no. 1, pp. 015001, 2016.

  (Receiving PbI_2 on substrate from Dr. Yangang Liang and then completing fabrication and characterization with Dr. Yangyi Yao)

- Y. Yao, W.-L. Hsu, M. Dagenais,” Low-Temperature Solution-Processed Hysteresis-Free Perovskite Solar Cell with High Energy Conversion Efficiency,” Entrepreneurship Award on 2016 NanoDay Conference Poster Presentation at the University of Maryland.

(Collaborating with Dr. Yangyi Yao to develop the whole fabrication technique, as well as contributing to half of fabrication and characterization of the solar cell)

Chapter 1 Dissertation Outline

This thesis encompasses two main subjects; the first part focuses on arrayed waveguide gratings and the application in on-chip spectrometer for astronomical instrumentation, and the second part focuses on perovskite solar cell and its application toward tandem solar cells. There are several key points in this dissertation. The arrayed waveguide gratings (AWG) with multiple inputs have been realized with high resolving power. A cascaded AWG with novel approach to fulfill flattened output transmission level with broader free spectral range (FSR) has been realized to proof of concept. In addition, perovskite solar cells with tunable bandgap by mixed organic cations have been achieved and a four-terminal configuration of perovskite tandem solar cells with a copper indium selenide (CIS) bottom cell has been proposed. The following paragraphs will briefly describe the outline of the thesis.

First part: Si_3N_4/SiO_2 Arrayed Waveguide Gratings.

In chapter 2, an overview of arrayed waveguide gratings (AWGs) will be introduced, followed by the in-depth exploration of the working principle, device fabrication and the characterization techniques. Subsequently, two distinct types of AWGs will be discussed, including Rowland AWG and three-stigmatic-point (TSP) AWG. Rowland AWG, known for its widespread usage, features circular image surface with no first- or second- order aberrations. TSP AWG, with its flat image surface, emerges as the preferred choice for applications in astrophotonics. Within this chapter, the design and layout of both Rowland and TSP AWG will be demonstrated in detail, offering a comprehensive understanding of their structural configurations. And finally, simulation

and experimental results will be given and a thorough analysis and discussion of the findings will be discussed.

In chapter 3, cascaded AWG, a configuration that encompasses a primary AWG coupled with multiple secondary AWGs, will be introduced and thoroughly examined. A meticulous dissection of the design process for the primary AWG, particularly one with a flat-top output, will be presented, accompanied by comprehensive simulations and a comparative analysis with the Rowland AWG. Secondary AWG is also designed to be a TSP AWG, renowned for its flat image surface. Top-hat layout structure will be introduced to make the output free propagation regions (FPRs) precisely aligned with each other in a compact design. Finally, simulation and experimental results will be provided and discussed. Performance comparison between different styles of cascaded AWGs will be given to conclude this chapter.

Second part: Perovskite Based Solar Cell.

In chapter 4, the background of the perovskite material used in photovoltaic application will be introduced. Then, perovskite material properties, including composition, crystal structure, and bandgap tunability will be discussed, followed by the perovskite solar cell structures and the various fabrication methods.

Next, the fabrication of our perovskite solar cell will be demonstrated, including the chemicals, tools and equipment used, accompanied by a comprehensive breakdown of the fabrication stages. Subsequently, all analysis and characterization techniques will be included, followed by the corresponding characterization results. It starts from the perovskite solar cell structure alongside the corresponding energy band diagram, and then

the optical bandgap measurement, followed by X-ray diffraction (XRD), and scanning electron microscope (SEM) characterization. And finally, the performance evaluation of the perovskite solar cells will be presented which includes the current-voltage (I-V) characteristics, the external quantum efficiency (EQE) analysis, and a comprehensive exploration of hysteresis effects.

Chapter 5 brings us into the realm of perovskite-CIS tandem solar cells. Initially, the background of tandem solar cell with perovskite top cell will be introduced. Given the well-established fabrication expertise within our group for CIS solar cells and the bandgap alignment of perovskite and CIS solar cell, a four-terminal perovskite-CIS tandem design will be presented, as well as the fabrication process of CIS solar cell. Finally, some preliminary findings from I-V and EQE measurement of our four-terminal perovskite-CIS tandem cell will also be presented.

Chapter 6 will summarize my research and offer a glimpse into the prospective endeavors lying ahead which includes new design of cascaded AWG and polarization-independent AWG as well as stability and encapsulation of perovskite solar cell and the design of two-terminal monolithic peroskite-CIS tandem solar cell.

Chapter 2 Rowland and Three-Stigmatic-Point Arrayed Waveguide Gratings

2.1 Introduction of Arrayed Waveguide Gratings

2.1.1 Overview of Arrayed Waveguide Gratings

Recently, arrayed waveguide gratings (AWGs) have been widely applied in telecommunication systems as multiplexers/demultiplexers and signal routers, as well as in optical sensing, quantum computing and spectroscopy [1-6]. The main functionality of AWGs is to separate different wavelengths spatially, as they image the field of an input waveguide onto an array of output waveguides in a dispersive way. It is believed to be a promising solution to some major challenges in observational astronomy in which the advanced on-chip astronomical instrumentations play an important role in improving observation of faint light sources from outer space. And this is a novel application of AWGs in astrophotonics where AWGs can be used as part of on-chip spectrographs [7].

Traditionally, an AWG is constructed with input/output waveguides, input/output free propagation regions (FPRs) and an array of waveguides (arrayed waveguides), which are elucidated in Fig. 2.1. The meticulous calculation of each arrayed waveguide's length is pivotal, as it determines an optical path length difference between adjacent arrayed waveguides that precisely matches an integer multiple of the center wavelength. This optical path, a product of effective refractive index and path length, will be discussed in the following sections. Here is the brief introduction of the operation principle of AWGs. A light source is coupled into the input waveguide before it enters the input FPR, where

the optical mode diverges and expands due to the lack of lateral confinement in the FPR. The diffracted beam is subsequently coupled into the arrayed waveguides at input aperture and continues to propagate through each arrayed waveguide. As the light reaches the output aperture, the phases at each arrayed waveguide are the same for central wavelength, which results in all beams converging precisely onto the center of the image surface. However, for all other wavelengths, the beams' phase fronts exhibit slight tilts because of some variations in the optical path length difference between adjacent arrayed waveguides, stemming from their different refractive indices. Consequently, the beams are focused onto some other off-center locations on the image surface. The output waveguides are positioned with some separation to collect the focused light. This is how AWGs can spatially separate lights with different wavelengths.

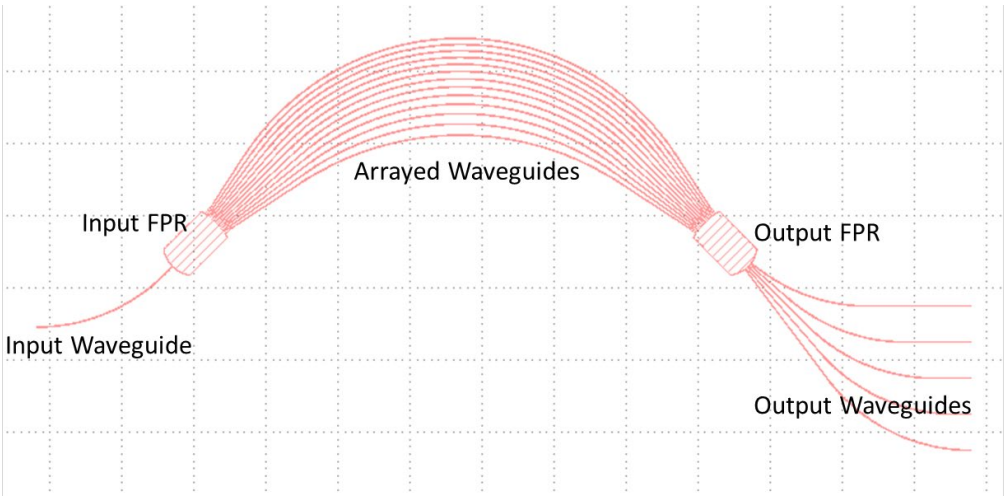

Fig. 2.1. An arrayed waveguide gratings and its composition is labeled.

Integrated photonics demonstrates a great potential in providing a promising approach for solving some major challenges in observational astronomy, especially in advanced on-ship astronomical instrumentations due to the ability to manipulating or

guiding light on a micro scale in these integrated photonics devices. Nowadays, extremely large telescopes (ELTs) with diameters of the main mirror almost 40 m is currently under construction in Chile [8]. With the cost of building instruments for these large telescopes being proportional to the square or even cube of the diameter of the telescope [5], constructing an ELT is extremely costly, not to mention the maintenance of those huge optics and the thermal stability across all the optical components. To miniaturize the astronomical instrumentation, an AWG is used as the light-dispersing component in an integrated photonic spectrograph (IPS) [7]. Some previous research has demonstrated that AWGs can be a suitable solution for astronomical spectroscopy [5-7] and that these integrated photonic devices possess a great potential towards the miniaturization of on-chip astronomical instrumentations.

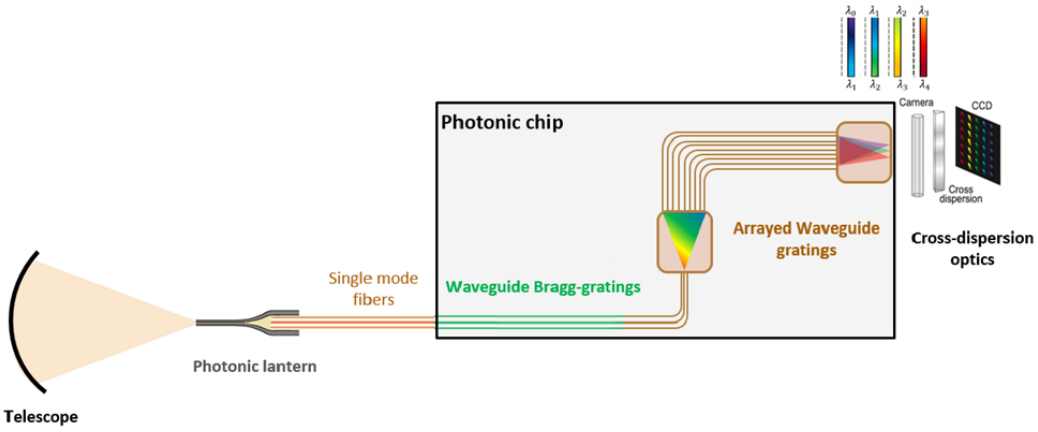

Fig. 2.2. The schematic of the proposed integrated photonic spectrograph

An integrated photonic spectrograph, as shown in Fig. 2.2 (image source: [7]), had been proposed to target this issue. This spectrograph is composed of a photonic lantern, several single-mode fibers, waveguide Bragg gratings, an arrayed waveguide gratings and

cross-dispersion optics components. The photonic lantern is used to guide the light collected from a telescope by converting an adiabatic tapered multimode fiber into several single-mode fibers which couple the light to a chip with waveguide Bragg grating and an AWG on it. The waveguide Bragg gratings had been developed with carefully designed multiple notch filters to eliminate the OH emission lines in the near-infrared region which is a long-time issue for ground-based telescopes [9-10]. Functioning as a light-dispersion component, the AWG effectively separates light based on varying wavelengths. With several different spectral orders of light being diffracted onto the image surface of the AWG, a set of cross-dispersion components serve to orthogonalize the overlapping light, effectively untangling their interference. The overlapping light is separated in wavelength by free spectral range (FSR), which will be elucidated in the subsequent section. Finally, the dispersed light is subjected to analysis by a detector array, thereby yielding a seamless and continuous two-dimensional spectrum image.

For this proposed spectrograph application, a continuous spectrum is preferred in the realm of astronomy. Through the elimination of output waveguides and the direct collection of dispersed light at the image surface, this spectrograph gains the advantage of getting a continuous output spectrum. The output spectrum is no longer measured through multiple output waveguides. In addition, concerns about crosstalk between output waveguides and additional losses arising from factors like sidewall roughness-induced scattering, bending, and taper losses are altogether mitigated. Therefore, this approach holds the potential to enhance the overall throughput of the AWG.

In order to realize the aforementioned cross-dispersion arrangement, it is required to cleave the chip along the output image surface of the AWG. However, conventional

Rowland AWGs possess a circular image surface, rendering them unsuitable for the proposed spectrograph application. As a result, this discrepancy prompts the design of three-stigmatic-point (TSP) AWGs to have a flat image surface to overcome the defocus aberration. Both Rowland AWGs and TSP AWGs will be discussed in the following sections, offering a comprehensive elucidation of their attributes and functionalities.

2.1.2 Aberration Theory

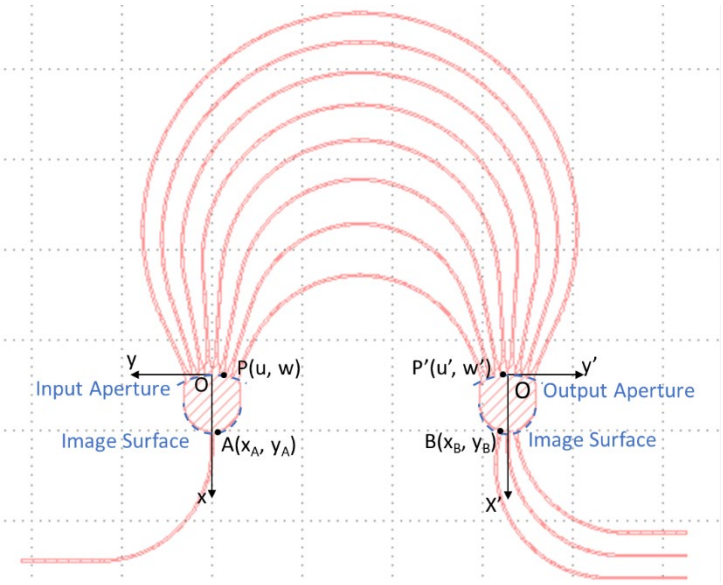

Fig. 2.3. The schematic of an AWG with coordinate system included

In 2001, a detailed derivation of aberration theory had been proposed by Wang et al to realized flat focal surface of AWGs [11]. In this section, a concise overview of aberration theory is illustrated before further discussion of Rowland and TSP AWGs.

Assuming an AWGs with $N \times N$ input/output waveguides and M arrayed waveguides in a rectangle coordinate, *XOY,* such that the center of the input aperture is the origin *O*. The x-axis is along the direction from center of input aperture to center of the

central input waveguide. And another rectangle coordinate, *X'O'Y'*, is set up in a similar way at the output aperture. The schematic can be found in Fig. 2.3. Thus, the input/output aperture can be expressed in a Taylor series:

$$u(w) = u(0) + u'(o)w + \frac{1}{2}u"(0)w^2 + \cdots + \frac{1}{n!}u^{(n)}w^n + \cdots \qquad (2.1)$$

A beam is injected into an input waveguide at $A(x_A, y_A)$, and propagates through input FPR to input aperture at $P(u, w)$ before it continue to propagate along one of the arrayed waveguide with length of $L(w)$ to reach the output aperture at $P'(u', w')$. Then, the beam is diffracted by the tilted phase front to be focused onto the output image surface at $B(x_B, y_B)$.

The optical path function (OPF) can be expressed as

$$F(w) = n_s r_A(w) + n_{AW} L(w) + G(w)m\lambda + n_s r_B(w) \qquad (2.2)$$

where n_s and n_{AW} are the effective index of the FPRs and the arrayed waveguides, respectively. $r_A(w)$, $r_B(w)$ represent the distance between *A* and *P*, *B* and *P'* and can be expressed as the following equations:

$$r_A(w) = \sqrt{(u - x_A)^2 + (w - y_A)^2} \qquad (2.3)$$

$$r_B(w) = \sqrt{(u' - x_B)^2 + (w' - y_B)^2} \qquad (2.4)$$

m is the spectral order; $L(w)$ is the length of the waveguide between *P* and *P'*; $G(w)$ is the number of waveguides from the center arrayed waveguide. In numerical calculations, $G(w) = i$ is used corresponding to the i^{th} arrayed waveguide counted from the center. Besides, the OPF can also be expressed in a Taylor series:

$$F(w) = F(0) + F'(0)w + \frac{1}{2}F"(0)w^2 + \cdots + \frac{1}{n!}F^{(n)}(0)w^n + \cdots \quad (2.5)$$

where the n^{th} aberration coefficient is

$$F^{(n)}(0) = n_s {r_A}^{(n)}(0) + n_{AW}L^{(n)}(0) - G^{(n)}(0)m\lambda + n_s {r_B}^{(n)}(0) \quad (2.6)$$

$F(0)$ is the constant term; By letting $F'(0)$ be 0, the aperture equation can be obtained at the origin *O*. $F^{(2)}(0)$, $F^{(3)}(0)$ and $F^{(4)}(0)$ represent defocus, comatic and spherical aberrations, respectively. Ideally, to achieve an aberration-free AWGs, all orders of $F^{(n)}(0)$ are required to be 0. However, lower orders of aberration coefficient contribute to most of the aberration. Therefore, to cancel out lower orders of aberration coefficients is crucial in terms of the AWG design.

2.1.3 Rowland Arrayed Waveguide Gratings

The Rowland geometry stands as the prevailing design choice for AWGs across diverse applications. By using Rowland AWG, the FPRs are defined by two curves, which are R_a as the radius of input/output aperture and ${R_a}/{2}$ as the radius of input/output image surface. The geometrical function of $u(w)$, $G(w)$ and $L(w)$ can be written as

$$u(w) = R_a - \sqrt{R_a^2 - w^2} \quad (2.7)$$

$$G(w) = \frac{R_a}{d} sin^{-1}(\frac{w}{R_a}) \quad (2.8)$$

$$L(w) = L_0 + \Delta L \cdot G(w) \quad (2.9)$$

where d is the separation between adjacent arrayed waveguide along the input/output aperture and L_0 is the length of central arrayed waveguide. The length

difference between adjacent arrayed waveguide is presented as ΔL, which can also be expressed by grating order m and center wavelength λ_c.

$$\Delta L = {m\lambda_c}/{n_{AW}} \tag{2.10}$$

The grating equation for AWG can be written as

$$n_s d sin\theta_i + n_s d sin\theta_o - n_{AW}\Delta L = m\lambda \tag{2.11}$$

In comparison to the conventional grating equation, there is an additional term $-n_{AW}\Delta L$ which is contributed by the length difference between adjacent arrayed waveguides. From Eq. (2.6), the first and second order of aberration coefficients can be derived as

$$F'(0) = n_s r_A'(0) + n_{AW} L'(0) - G'(0)m\lambda + n_s r_B'(0) \tag{2.12}$$

$$F''(0) = n_s r_A''(0) + n_{AW} L''(0) - G''(0)m\lambda + n_s r_B''(0) \tag{2.13}$$

To evaluate the first order aberration coefficient $F'(0)$, we can plug Eq. (2.3), (2.4) and (2.7) to (2.10) into Eq. (2.12), we can get

$$F'(0) = -n_s \frac{y_A}{r_A} + n_{AW} \frac{\Delta L}{d} + \frac{m\lambda}{d} - n_s \frac{y_B}{r_B} \tag{2.14}$$

where r_A is the distance between *O* and *A*, so $u = w = 0,\ r_A = r_A(0) = \sqrt{x_A^2 + y_A^2}$ and similarly, $r_B = r_B(0) = \sqrt{x_B^2 + y_B^2}$. Thus, $\frac{y_A}{r_A}$ can be expressed as $sin\theta_i$ and similarly $\frac{y_B}{r_B}$ can be expressed as $sin\theta_o$. Eq. (2.14) can be reduced to

$$-n_s sin\theta_i - n_{AW} \frac{\Delta L}{d} + \frac{m\lambda}{d} - n_s sin\theta_o = 0 \tag{2.15}$$

Comparing Eq. (2.11) and (2.15), we can deduce that $F'(0) = 0$.

In terms of second order aberration coefficient $F''(0)$, just like the case of first order $F'(0)$, we can plug the same Eq. (2.3) and (2.4) into Eq. (2.13). Both $n_{AW}L''(0)$ and $G''(0)m\lambda$ terms are gone since $L''(0) = G''(0) = 0$. Therefore, only $n_s{r_A}''(0)$ and $n_s{r_B}''(0)$ terms are left. Eq. (2.13) can be written as

$$F''(0) = -n_s(-\frac{y_A^2}{r_A^3} - \frac{x_A}{R_a r_A} + \frac{1}{r_A} - \frac{y_B^2}{r_B^3} - \frac{x_B}{R_a r_B} + \frac{1}{r_B}) \tag{2.16}$$

Since point A is on the image surface, it satisfies the following equation.

$$(x_A - \frac{R_a}{2})^2 + y_A^2 = (\frac{R_a}{2})^2 \tag{2.17}$$

Plugging Eq. (2.17) back to Eq. (2.16), the first three terms on the right-hand side can be canceled out. Similarly, point B is on the output image surface. It also satisfies the following expression,

$$(x_B - \frac{R_a}{2})^2 + y_B^2 = (\frac{R_a}{2})^2 \tag{2.18}$$

After plugging Eq. (2.18) back to Eq. (2.16), the other three terms on the right-hand side can be erased. As a result, the second order aberration coefficient can be obtained, $F''(0) = 0$.

The derivation above demonstrates that Rowland AWG inherently lacks first- and second-order aberrations, accounting for their widespread preference in AWG design. Nevertheless, in the field of astrophotonics, a cross-dispersion setup or detector array is attached to the output image surface to acquire a continuous transmission spectrum. The

curved image surface characteristic of Rowland AWGs renders them less ideal as a design choice.

2.1.4 Three-Stigmatic-Point Arrayed Waveguide Gratings

The concept of three-stigmatic-point (TSP) AWG was proposed in 2003 by Lu et al [12], as an application of the aberration theory by Wang et al in 2001. This innovative design of the TSP AWG has been explored. By strategically selecting three distinct wavelengths as the stigmatic points and aligning the focus positions according to these wavelengths, the geometries of the input/output free propagation regions (FPRs) can be restructured, especially to be a flat image surface. This overview demonstrates the fundamental design approach of the TSP AWG.

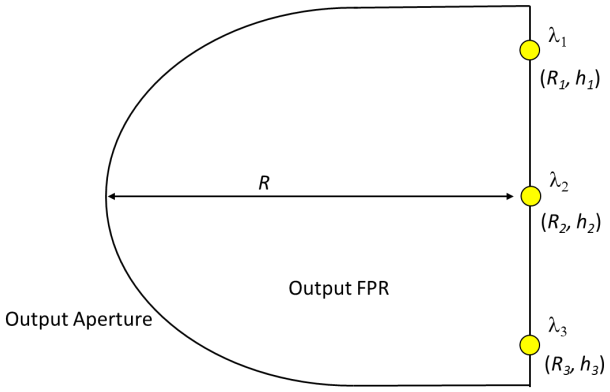

Fig. 2.4. The schematic of output FPR of a TSP AWG

As mentioned in the previous sections, there are three free parameters in the design of AWG, which are $u(w)$ as the input/output aperture function, $G(w)$ as the number of arrayed waveguide from the center and $L(w)$ as the length of the arrayed waveguide. The AWG design can accommodate a maximum of three constraints. For a Rowland AWG, the

three restraints are R_a as the radius of input/output aperture, the evenly distributed arrayed waveguides along the input/output aperture, and the constant length difference between adjacent arrayed waveguides. Now, three stigmatic points are introduced as three restraints to create a flat image surface of input/output FPRs. Three different wavelengths are chosen as λ_1, λ_2 and λ_3 with their corresponding focus point (R_1, h_1), (R_2, h_2) and (R_3, h_3), as demonstrated in Fig. 2.4. If λ_2 is set to be the center wavelength λ_C, R_2 is set to be R_a and proper $\lambda_1 = \lambda_C + \Delta\lambda$ and $\lambda_3 = \lambda_C - \Delta\lambda$, in order to achieve flat image surface, the three stigmatic points are set to be (R_a, h), $(R_a, 0)$ and $(R_a, -h)$. $u(w)$, $G(w)$ and $L(w)$ are needed to be solved in an iterative method.

The first iteration is carried out with the following initial conditions:

$$u(0) = 0 \tag{2.19 a}$$

$$u'(0) = 0 \tag{2.19 b}$$

$$G(0) = 0 \tag{2.19 c}$$

$$G'(0) = {}^{1}/_{d} \tag{2.19 d}$$

$$L(0) = constant \tag{2.19 e}$$

$$L'(0) = G'(0)\Delta L = {}^{\Delta L}/_{d} \tag{2.19 f}$$

where d is the separation between adjacent arrayed waveguides. ΔL is the length difference between adjacent arrayed waveguides. Both parameters are carried over here from the Rowland structure. From Eq. (2.3) and (2.6), we have

$$n_s {r_A}^{(n)}(0) + n_{AW} L^{(n)}(0) - G^{(n)}(0) m\lambda_i + n_s {r_i}^{(n)}(0) = 0 \tag{2.20}$$

$$r_i(w) = \sqrt{(u - x_i)^2 + (w - y_i)^2} \tag{2.21}$$

where $i = 1,2,3$, representing three stigmatic points. $u^{(n)}(0)$ can be expressed as

$$u^{(n)}(0) = \frac{(\lambda_1-\lambda_2)\left(\Psi_1^{(n)}-\Psi_3^{(n)}\right)-(\lambda_1-\lambda_3)(\Psi_1^{(n)}-\Psi_2^{(n)})}{(\lambda_1-\lambda_3)\left(\frac{x_2}{r_2}-\frac{x_1}{r_1}\right)-(\lambda_1-\lambda_2)(\frac{x_3}{r_3}-\frac{x_1}{r_1})} \tag{2.22}$$

where $r_i = r_i(0) = \sqrt{x_i^2 + y_i^2}$, and $\Psi_i^{(n)}$ can be expressed as

$$\Psi_i^{(n)} = \frac{1}{2}\sum_{k=1}^{n-1} C_k^n \left[u^{(k)}(0)u^{(n-k)}(0) - r_i^{(k)}(0)r_i^{(n-k)}(0)\right]/(r_i + \delta(n-2)/r_i) \tag{2.23}$$

Thus, $r_i^{(1)}(0)$ can be derived as $\Psi_i^{(1)}(0) - u^{(1)}(0)\frac{x_i}{r_i}$

Moving on to the second iteration, $u^{(2)}(0)$ and $r_i^{(2)}(0)$ can be derived from $u^{(1)}(0)$ and $r_i^{(1)}(0)$. After numerous iterations, $u^{(n)}(0)$ and $r_i^{(n)}(0)$ can be derived from all the $u^{(j)}(0)$ and $r_i^{(j)}(0)$, where $j = 1,2,\dots,n-1$. And then, $L^{(n)}(0)$ and $G^{(n)}(0)$ can be solved by using Eq. (2.6) and all the $u^{(n)}(0)$ and $r_i^{(n)}(0)$. Finally, $u(w)$ can be solved by using Eq. (2.1) as well as $L(w)$ and $G(w)$ in a similar way.

2.2 Fabrication Details of Arrayed Waveguide Gratings

The AWGs discussed in the following sections are mostly fabricated in-house at the Fablab in the Maryland NanoCenter except the e-beam lithography system which is located in the Physical Sciences Complex building. Our proposed AWGs are based on Si_3N_4/SiO_2 platform with a thickness of 100 nm. This choice offers distinct advantages over the silica platform, primarily due to the higher refractive index difference ratio.

Consequently, AWG devices can be realized with a more compact footprint, rendering them less susceptible to issues like flexure or thermal drift which are critical aspects within the realm of astrophotonics. It's noteworthy that our group has demonstrated the potential of achieving remarkably low propagation losses on the Si_3N_4/SiO_2 platform. In fact, on a 100-nm Si_3N_4/SiO_2 platform, the propagation loss can be achieved as low as 0.018 dB/cm with output waveguides tapered down to 600 nm in width [13]. In addition, compared to Ge doped SiO_2 platform [14], Si_3N_4/SiO_2 platform suffers less chromatic aberration, leading to a more consistent performance across a broader bandwidth for the AWG.

2.2.1 Device Fabrication

A commercial Si wafer with 5-um thermal silicon dioxide (SiO_2) is employed as device substrate, which is first cleaned in a sequence of acetone, methanol, and isopropanol for 5-10 mins each in an ultra-sonic cleaner. Then, a 100-nm silicon nitride (Si_3N_4) is deposited via low-pressure chemical vapor deposition (LPCVD, by Tystar LPCVD). Positive e-beam resist, ZEP-520A, is spin-coated onto the substrate with the spin rate of 4500 rpm for 1 min, with the corresponding thickness of around 325 nm. After a soft bake at 180^{o}C for 2 min, aquaSAVE, an antistatic agent, is also spin-coated with the spin rate of 4500 rpm for 1 min. The purpose of aquaSAVE is to prevent electrons from accumulating on the surface of the e-beam resist during e-beam lithography process. E-beam lithography (by Elionix G100 system) is conducted with dosage of 300 $\mu C/cm^2$ to pattern the device followed by developing process to remove exposed resist. The e-beam-exposed substrate is soaked in water for 30 s to remove aquaSAVE and then is developed in ZED-N50 for 1 min immediately followed by MIBK/IPA (1:3) solution and IPA for 30 s each. Next, a 3-nm chromium layer is deposited via e-beam evaporation as a hard mask. Lift-off is

conducted by soaking the substrate into heated Remover PG on a hot plate with temperature of 85ºC for at least 30 min. To get cleaner substrate, an ultra-sonic bath or overnight soaking in Remover PG is preferred to ensure all residual resist is completely removed. By using CHF_3/O_2-based plasma dry etching system (by Oxford Instruments Plasmalab System 100), the device pattern is transferred to Si_3N_4 layer. After the chromium hard mask has been removed with etchant, a 3-um SiO_2 top cladding is deposited with plasma-enhanced chemical vapor deposition (PECVD, by Oxford Instruments Plasmalab System 100). The schematic of the fabrication process is summarized in Fig. 2.5.

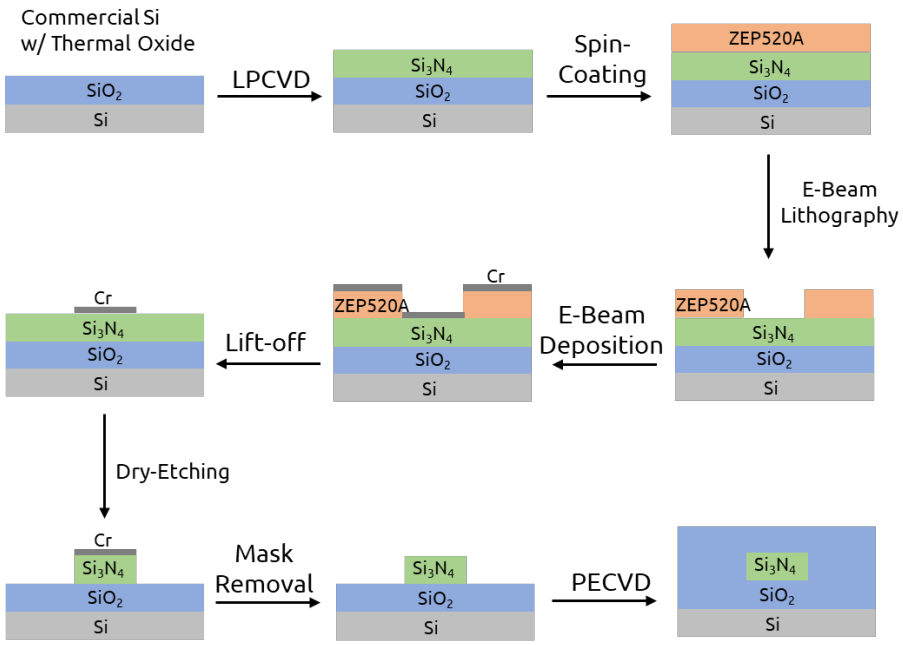

Fig. 2.5. Fabrication process on 100-nm Si_3N_4 platform with ZEP-520A positive resist

Positive e-beam resist is adopted because of the consistent performance of the devices. Despite potential concerns like residual chromium contamination and increased sidewall roughness due to chromium lift-off, positive resist processing consistently yields

devices that perform reliably across various batches. In contrast, the utilization of negative resist (ma-N 2403) results in inconsistent device performance. This variance is attributed to the need for distinct e-beam dosages optimized for pattern geometries of varying feature sizes. Larger pattern requires lower dosage to prevent overdose while smaller pattern requires higher dosage to ensure a vertical sidewall. Therefore, negative e-beam resist is not suitable for arrayed waveguide gratings since the size of FPRs can reach hundreds of micrometers while the size of waveguides is only several micrometers or even sub-micrometer.

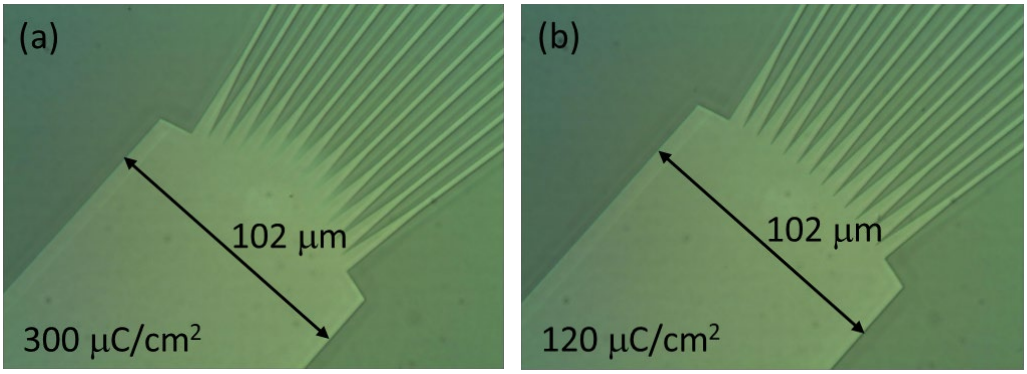

Fig. 2.6. Microscope images of FPRs with various dosage. (a) 300 $\mu C/cm^2$ and (b) 120 $\mu C/cm^2$

Figure 2.6 shows microscope image comparison between a higher-dosed (300 $\mu C/cm^2$) FPR and a lower-dosed (120 $\mu C/cm^2$) FPR fabricated with negative resist process. All other regions are exposed with dosage of 300 $\mu C/cm^2$. An evident case of overexposed FPR can be observed in Fig. 2.6 (a), resulting from using an identical dosage as that applied to the waveguide region. In addition, even if the dosage is lowered in FPR regions, the numerous interfaces between input/output waveguides and FPRs, as well as between

arrayed waveguides and FPRs, introduce uncertainty concerning the profiles and shapes of these connecting elements with distinct dosages.

2.2.2 Characterization Techniques and Tools

For measurement purposes, a fiber-chip butt-coupling technique is employed. Consequently, every chip undergoes cleavage on both sides to unveil the input/output waveguide facets intended for coupling. The scanning spectrum covers from 1450 nm to 1640 nm from a tunable laser source (Agilent Technologies 8164B). The input light source is coupled into a polarization-maintaining (PM) fiber, which is further edge-coupled into the chip. The simulated coupling efficiencies can reach around 90% for 100-nm Si_3N_4 platform by using a straight waveguide linearly tapered down to the optimized width of 600 nm for the best coupling efficiency [13]. To ensure precise input polarization, a fiber rotator with an angle accuracy of 5 degrees is employed. Index matching liquid is required at input/output facets of the cleaved fibers to minimize the reflection at those cleaved facets. Another PM fiber is used to edge-couple the output light from the chip, and finally the output signal is characterized by a multi-channel power meter (Keysight Technologies N7744A). Both input/output PM fibers are mounted on motorized three-axis stage controlled by LabView program.

2.3 Simulation of Arrayed Waveguide Gratings

In this section, the simulation procedure for both Rowland and three-stigmatic-point (TSP) AWGs are demonstrated, as well as the simulation results.

2.3.1 Simulation of Rowland Arrayed Waveguide Gratings

A commercial software, RSoft Photonics Design Suite by Synopsys, is used in Rowland AWGs simulation. Device geometry and layout design are completed on 100-nm Si_3N_4 platform in Rsoft. The designs of two different devices are proposed here; the first one features lower resolving power (~ 5,000) and the other shows higher resolving power (~ 17,000). The definition of the resolving power (R) is $\lambda/\Delta\lambda$, where λ is the peak wavelength; $\Delta\lambda$ is the 3-dB bandwidth. The design parameters are listed in Table I. The two values correspond to lower/higher resolving power design.

TABLE I ROWLAND AWGS SIMULATION PARAMETERS

Parameters	Description	Value (Lower R/Higher R)
N_{in}	Number of input channels	1/3
N_{out}	Number of output channels	31/101
N_{aw}	Number of arrayed waveguides	65/201
λc	Central wavelength	1550/1550 nm
$\Delta\lambda$	Wavelength spacing	0.5/0.15 nm
w	Width of arrayed waveguides	2/2 μm
d_{aw}	Arrayed waveguide spacing	6/6 μm
d_{io}	Input/Output waveguide spacing	6/6 μm

Straightforward V-shaped layout is generated in Rsoft with minimum bending radius set to 1,000 μm to prevent bending loss. The simulation tool used here is BeamPROP, which leverages a finite difference beam propagation method. This tool offers comprehensive simulations for computing light propagation in diverse waveguiding geometries. Prior to conducting the transmission spectrum simulation, the effective refractive index of the arrayed waveguide is calculated by using Beam Propagation Mode Solver (BPM Solver), which numerically resolves the monochromatic wave equations. By subsequently integrating the obtained effective refractive index data back to the BeamPROP and using Effective Index Method (EIM), the accuracy of simulation is greatly improved from 2-D simulation and close to full 3-D simulation without sacrificing the simulation speed. As a result, 3-D with EIM in BeamPROP is employed in the following simulation.

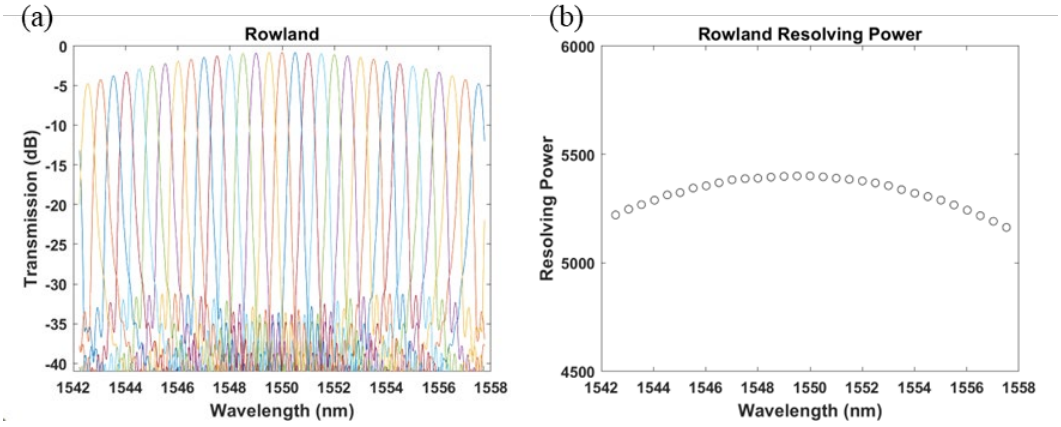

Fig. 2.7. (a) The simulated transmission spectrum of Rowland AWG (lower resolving power) and (b) its corresponding resolving power

The simulated transmission spectra and corresponding resolving power are shown in Fig. 2.7. The results of the AWG with lower resolving power are demonstrated in (a)

and (b). The peak transmission is about -0.9 dB for central channels and the transmission is reduced to around -5.0 dB for outer channels. The crosstalk is more than 25 dB lower and the noise level is -30 to -35 dB.

The resolving power for each output channel is calculated by extracting the 3-dB bandwidth obtained by finding the two nearest data points with 3-dB transmission on both sides of each peak and conducting linear interpolation. The resolving power starts at about 5150 at outer channels while it gradually increases to almost 5400 at central channels. Rowland AWG features a very consistent performance across the spectrum because it suffers from no first- and second-order aberration. The dispersed light with different wavelengths is focused on the circular image surface.

The spectrum in Fig. 2.7 (a) shows one free spectral range (FSR), which can be expressed as

$$FSR = \frac{n_{AW}\lambda_C}{mn_g} \tag{2.24}$$

where m is the grating order and n_g is the group effective index of arrayed waveguide, which is defined as

$$n_g \approx n_{AW} - \lambda \frac{\partial n_{AW}}{\partial \lambda} \tag{2.25}$$

n_g gradually decreases as the increasing wavelength. Therefore, FSR gradually becomes slightly larger at increasing wavelength.

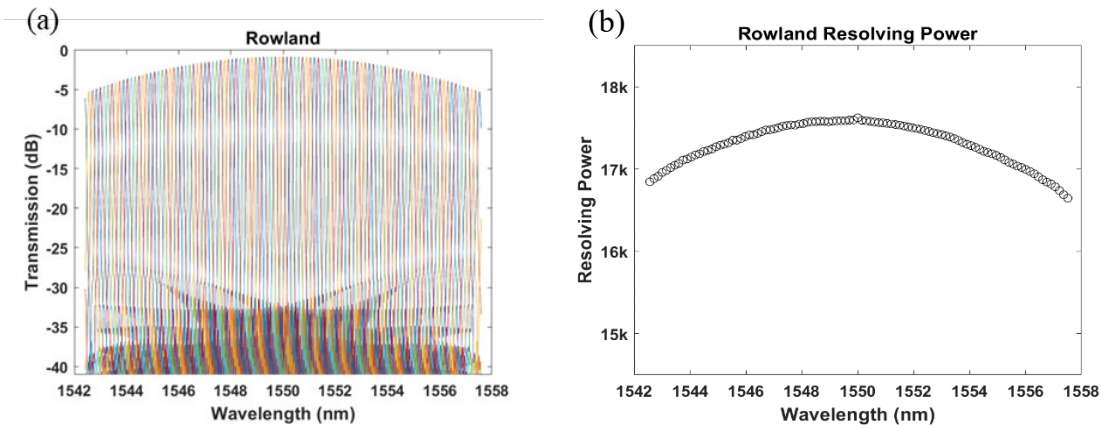

Fig. 2.8. (a) The simulated transmission spectrum of Rowland AWG (higher resolving power) and (b) its corresponding resolving power

Regarding the higher resolving power AWG, the simulated results from the central input channel are displayed in Fig. 2.8 (a) and (b). The peak transmission is about -1.0 dB for central channels and the transmission is observed 4 to 5 dB lower for the outer channels. The crosstalk is still more than 20 to 25 dB lower and the noise level is also -30 to -35 dB. The highest resolving power can reach over 17,600 and it remains above 16,600 across all output channels. Similar to the previous case, the consistent performance of Rowland AWG still can be observed.

2.3.2 Simulation of Three-Stigmatic-Point Arrayed Waveguide Gratings

A MATLAB program is meticulously crafted from the aberration theory discussed in the previous sections. For performance comparison, the simulation parameters for TSP AWGs are the same as those for Rowland AWGs, listed in Table I. As a result, two cases are simulated in this section. To solve the geometry of the input/output FPRs, three output channels are chosen to be the three stigmatic points. For lower resolving power AWG,

there are 31 output channels, and the channels 3, 16 and 29 are chosen to be the three stigmatic points. The iterative solution of Equation (5.20) guides the determination of u(w), L(w), and G(w) until a flat image surface is achieved. Optical path function $F(w)$ is used to determine if more iterations are needed before reaching the flat image surface.

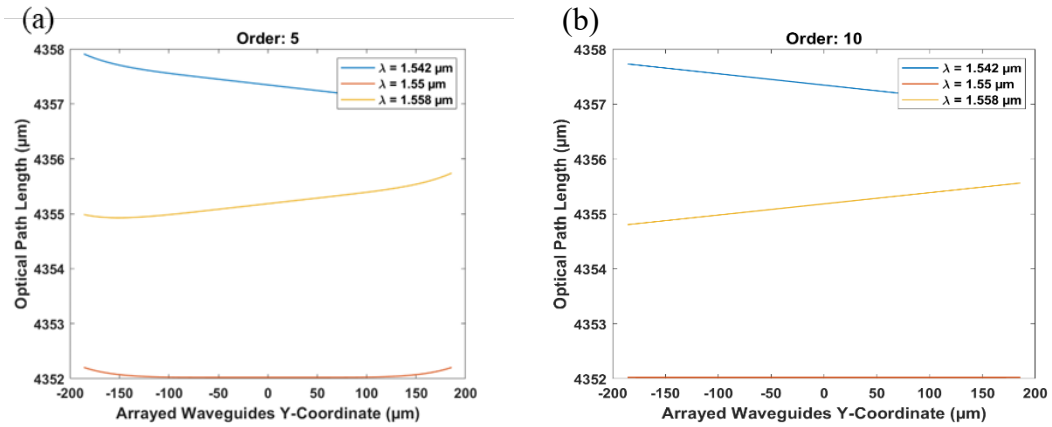

Fig. 2.9. The optical path function of TSP AWG (lower resolving power) for three stigmatic points; (a) after 5 orders of iterations and (b) after 10 orders of iterations.

The optical path function $F(w)$ for three stigmatic points is plotted in Fig. 2.9. $F(w)$ is supposed to be constant for all w, which is the y-coordinate at output image surface. After undergoing 5 iterations, the behavior of $F(w)$, depicted in Fig. 2.9 (a), unveils curvature along the edges of the image surface. This outcome, evidently, deviates from the intended outcome, implying the necessity for further iterations. However, as indicated in Fig. 2.9 (b), after 10 rounds of iteration, $F(w)$ exhibits straight-line profiles across all three wavelengths. However, only central wavelength, 1.55 μm, can reach perfect flat at image surface. For the remaining wavelengths, a discrepancy of approximately 1 μm is observed, signifying the presence of slight defocus aberration in the TSP AWG. The

corresponding input/output aperture and extra lengths for arrayed waveguides are calculated and plotted in Fig. 2.10 (a) and (b), respectively.

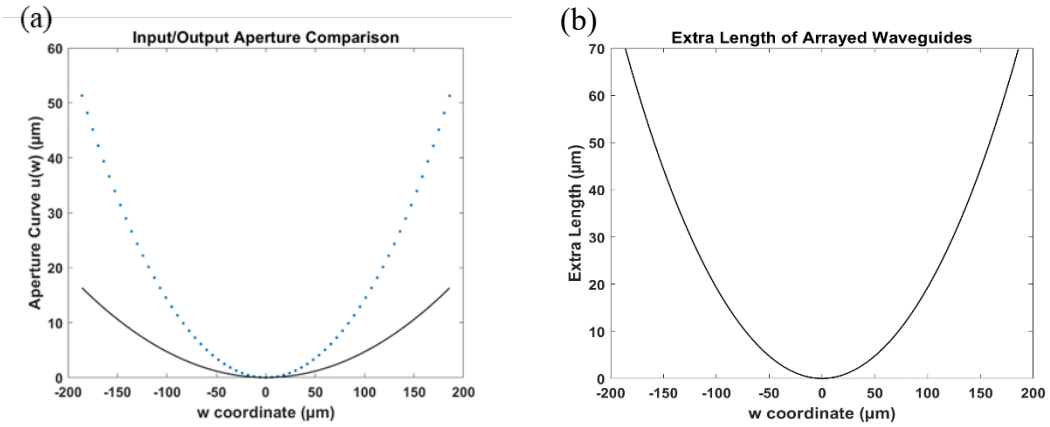

Fig. 2.10. (a) The input/output aperture comparison; solid line represents Rowland structure and dots represents TSP structure. (b) The extra lengths needed for arrayed waveguides to compensate the geometry difference of FPRs between Rowland and TSP AWGs.

The solid line in Fig. 2.10 (a) shows the circular aperture of FPRs of Rowland AWG and the dots represent the polynomial aperture of FPRs of TSP AWG. In addition, the length difference between adjacent arrayed wavelength is no longer constant since there is some extra length for arrayed waveguides required to compensate the geometry difference of FPRs between Rowland and TSP AWGs.

Besides, for the case of higher resolving power TSP AWG, the optical path function $F(w)$ for three stigmatic points is plotted in Fig. 2.11. Now, there are 101 output channels and channels 11, 51 and 91 are chosen to be three stigmatic points. After 5 iterations, curved edges persist within $F(w)$ across all three wavelengths, indicating the requirement for further iterations. Only after 20 iterations does $F(w)$ exhibit the desired straight-line profiles for all three wavelengths. Compared to the case of lower resolving power TSP

AWG, the variation in image surface is well within 1 μm range, indicating that this TSP AWG suffers little defocus aberration. The corresponding aperture comparison and extra lengths of arrayed waveguides are plotted in Fig. 2.12.

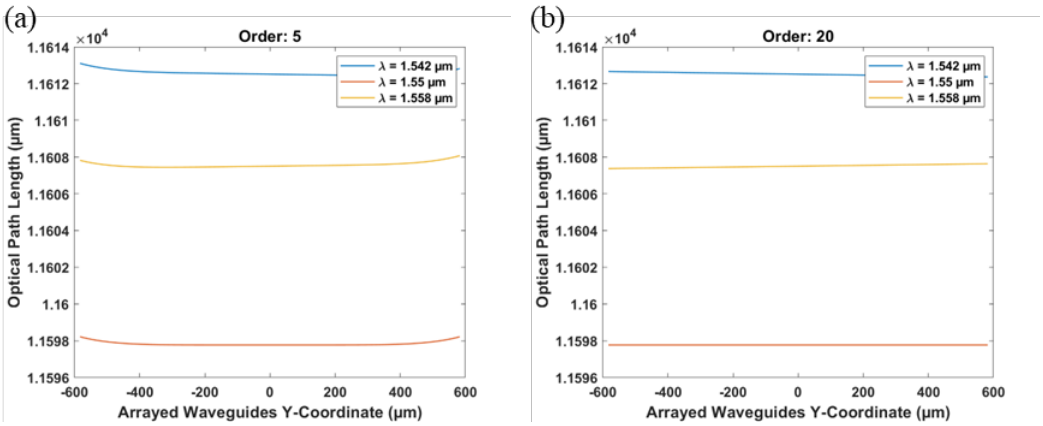

Fig. 2.11. The optical path function of TSP AWG (higher resolving power) for three stigmatic points; (a) after 5 orders of iterations and (b) after 20 orders of iterations.

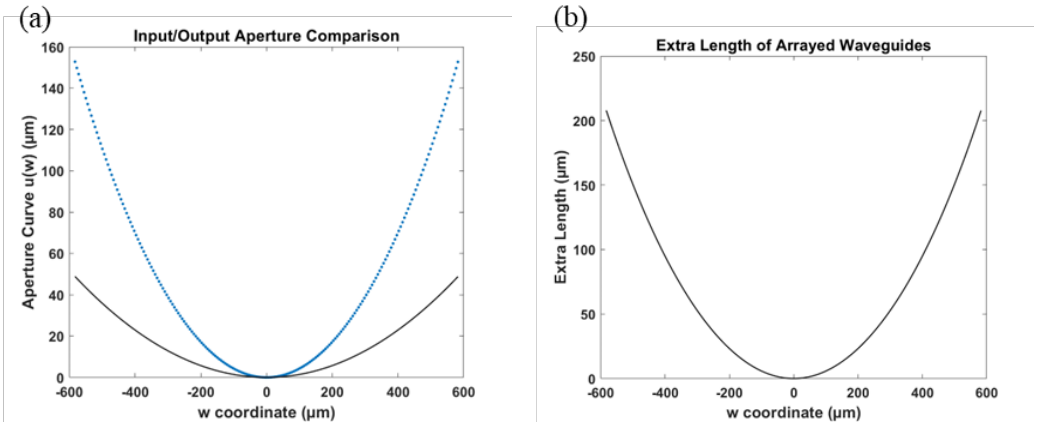

Fig. 2.12. (a) The input/output aperture comparison; solid line represents Rowland structure and dots represents TSP structure. (b) The extra lengths needed for arrayed waveguides to compensate the geometry difference of FPRs between Rowland and TSP AWGs.

Again, the solid line in Fig. 2.12 (a) shows the circular aperture of FPRs of Rowland AWG and the dots represent the polynomial aperture of FPRs of TSP AWG. The

compensation length of arrayed waveguides can reach several hundreds of micrometers in this case for some outer arrayed waveguides.

In order to simulate the transmission spectrum of TSP AWG in Rsoft, some additional procedures are necessary, primarily because Rsoft employs a Rowland structure for AWGs. First, a Rowland AWG counterpart with the same parameters is created in Rsoft. Subsequently, the input FPR is substituted with the computed TSP AWG structure. Upon designating each arrayed waveguide as an individual pathway and implementing a pathway monitor for each, the BeamPROP tool facilitates separate simulations to extract power and phase information at each arrayed waveguide. The input FPR of TSP AWGs of both lower/higher resolving power is demonstrated in Fig. 2.13 (a) and (b), respectively. The scales for Fig. 2.13 (a) and (b) are different; the actual size of FPR with higher resolving power is more than three times longer.

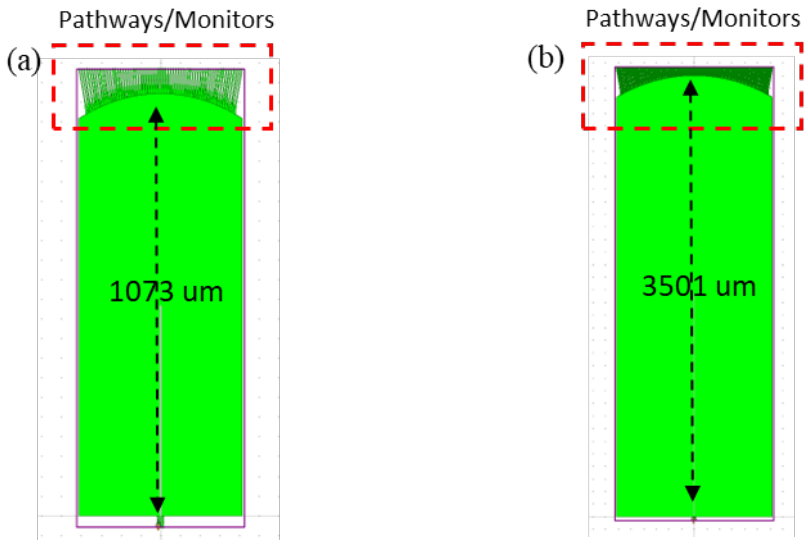

Fig. 2.13. The input FPR of TSP AWGs in Rsoft for simulation with calculated geometry and pathways and monitors are added to all arrayed waveguides; (a) lower resolving power case and (b) higher resolving power case.

And then, power is assumed to be the same along the arrayed waveguides and propagation loss in arrayed waveguides are neglected. Phase information at the output aperture of output FPR can be calculated by using the following expression,

$$\frac{\Delta\theta}{2\pi} = \frac{L}{\lambda/n_{AW}} \tag{2.26}$$

where $\Delta\theta$ is the phase difference at the beginning and the end of the arrayed waveguide. Before simulating the output spectrum, the output FPR is replaced by the calculated structure, as plotted in Fig. 2.14 for both lower resolving power case (a) and higher resolving power case (b). And then each output waveguide is assigned as a pathway while pathway monitors are applied to all pathways.

In addition to the phase difference after light guided along the arrayed waveguides, there exists another pertinent phase error to be addressed. While Eq. (2.26) stays true for a point source of light, it's important to note that real light sources possess a specific mode size, rather than being point sources. Consequently, the phase information obtained through our MATLAB calculations, based on aberration theory, will inherently differ from that obtained via Rsoft's BeamPROP tool. Therefore, this phase error must be compensated by adding or subtracting the corresponding effective length of arrayed waveguides. The failure to adequately address this phase error would significantly compromise the AWG's performance, particularly in terms of its resolving power.

Next, a launch field is prepared by using the power information acquired by the simulation earlier and phase information calculated by using Eq. (2.26). The launch field is then injected into arrayed waveguides. The final step is to run BeamPROP for the output

FPR by our MATLAB script to get the power information for all wavelengths at every output waveguide.

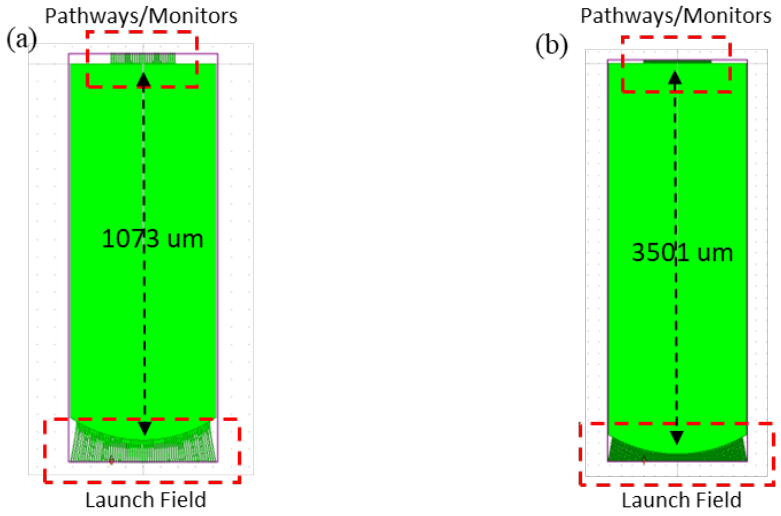

Fig. 2.14. The output FPR of TSP AWGs in Rsoft for simulation with calculated geometry; pathways and monitors are added to all output waveguides and launch field are injected into the arrayed waveguides; (a) lower resolving power case and (b) higher resolving power case.

If the phase error contributed from the disparity between the calculation from aberration theory and the Rsoft simulation is not taken care of, it can lead to a shift of the actual focal image surface. This shift could involve the focal image surface moving either closer to or further away from the output aperture. To address this concern, a series of simulations has been conducted to determine the actual focal image surface by using higher resolving power TSP AWG as an example. In this test, different position of focal plane has been chosen from 50 μm closer to the output aperture (presented as -50 μm) to 50 μm further away from the output aperture (presented as +50 μm). The resolving power of the original designed TSP AWG is shown in Fig. 2.15. The central channels demonstrate a resolving power around 14,000, which is a significant decrease from its Rowland AWG

counterpart. The Rowland AWG of the same simulation parameters features a resolving power of over 17,500 at the central channels, meaning the TSP AWG suffers a 20% decrease in resolving power.

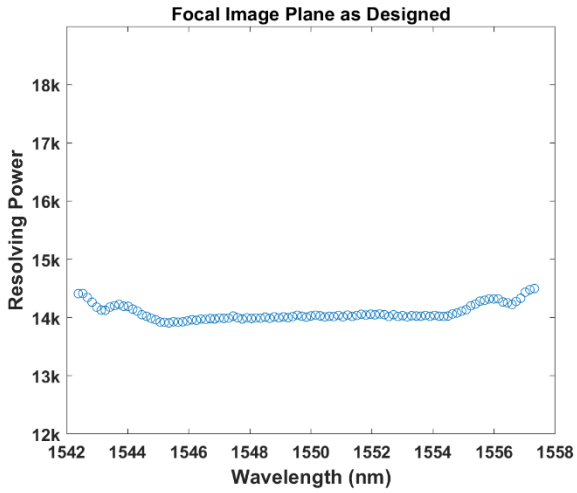

Fig. 2.15. The resolving power of TSP AWG without compensating extra phase error induced by the difference between aberration theory and Rsoft simulation.

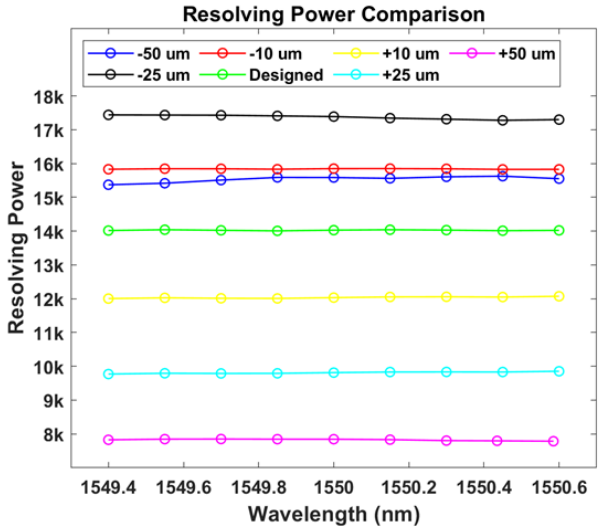

Fig. 2.16. The resolving power comparison between a series of TSP AWG without compensating extra phase error induced by the difference between aberration theory and Rsoft simulation. "+" represents further away from output aperture while "-" means closer.

In addition, the resolving power of the central several channels of each case have been calculated and plotted in Fig. 2.16. The best performance from the series is obtained from the case of -25 μm, and the resolving power reaches around 17,400, which is comparable to the performance of the Rowland AWG. Therefore, the focal image surface moves 25 μm closer to the output aperture when the phase errors are not compensated in this specific case.

The stimulated transmission spectrum of TSP AWG with lower resolving power is presented in Fig. 2.17 (a) and the corresponding resolving power is shown in Fig. 2.17 (b).

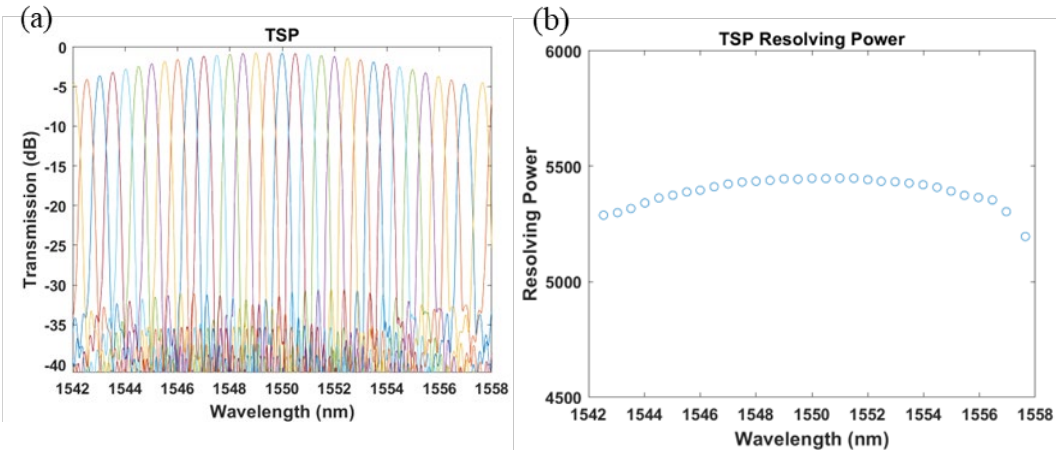

Fig. 2.17. (a) The simulated transmission spectrum of TSP AWG (lower resolving power) and (b) its corresponding resolving power

The peak transmission at the central channels is around -0.8 dB, which is even better than the Rowland counterpart while the transmission from the outer channels is 4 to 5 dB lower. The crosstalk is about 30 dB lower and the noise level is at -30 to -35 dB. The largest resolving power obtained is around 5,450 near the central channel, and it gradually reduced to around 5,200 at outer channels. Comparing the results between TSP and

Rowland AWG, the throughput of both AWGs is similar. The performance is pretty much the same, and even slightly higher resolving power can be observed from TSP AWG. Even though there is still some defocus aberration in TSP AWG from the MATLAB calculation, the variation in flat focal image surface is merely 1 μm, which has little to no influence on the TSP AWG performance based on the simulation results.

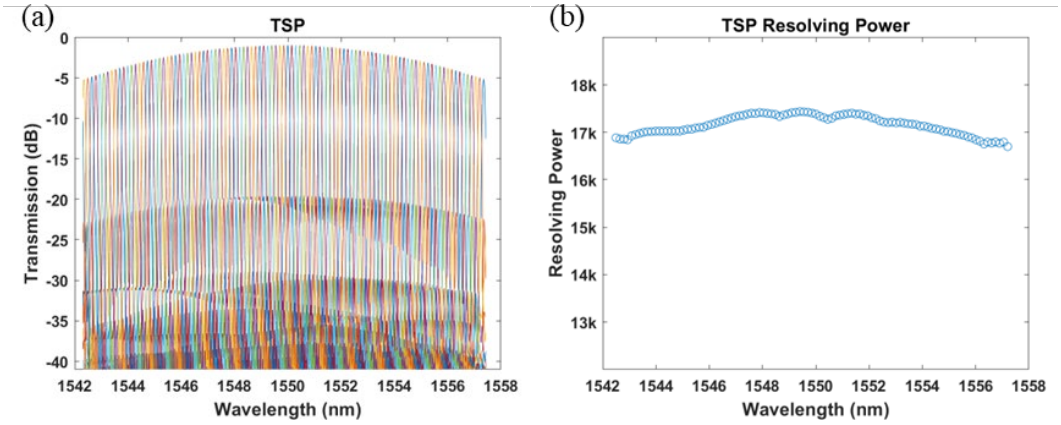

Fig. 2.18. (a) The simulated transmission spectrum of TSP AWG (higher resolving power) and (b) its corresponding resolving power

In the case of TSP with higher resolving power, the transmission spectrum and corresponding resolving power is demonstrated in Fig. 2.18 (a) and (b), respectively. The transmission of the central channel is -1.0 dB and the transmission of the outer output channels are 4 to 5 dB lower. There are side lobes observed around -20 dB, leading that the crosstalk is reduced to 18 to 20 dB lower. The highest resolving power can reach over 17,400 and it remains above 16,700 across all output channels. The performance between TSP AWG and Rowland counterpart is very similar, and even at some output channels, higher resolving power can be obtained, but the difference is very limited and can be negligible. This simulation verifies that by using aberration theory to design the geometry

of input/output FPRs, an AWG with flat image surface can be realized without sacrificing any performance.

2.4 Layout Design of Arrayed Waveguide Gratings

Before moving forward to fabricate physical devices and conduct experimental characterizations, the meticulous layout design of AWGs is important. Throughout the simulation process, the configuration of FPRs for Rowland or TSP AWGs has been solidified. Specifically, the FPRs for Rowland AWGs are generated via Rsoft, while the FPRs for TSP AWGs are calculated using aberration theory. Therefore, the layout of arrayed waveguides and input/output waveguides are left to be determined. When designing the input/output waveguides, there are several key considerations to adhere to. First, the minimum bending radius is set to be 1000 μm to ensure the bending loss is minimized and it will not affect the throughput. The other is the gap between adjacent input/output waveguides. This gap denotes the separation between neighboring waveguides from sidewall to sidewall. To gain a comprehensive grasp of waveguide gaps that prevent coupling between each other, FIMMWAVE is used to simulate several straight waveguides as directional couplers. There are five straight waveguides with width of 2 μm and height of 100 nm thoughtfully arranged in parallel with the spacing between them varying from 4 μm to 12 μm. Notably, only the central waveguide (referred to as waveguide #N in the simulation) is subjected to light injection. The coupling result is displayed in Fig. 2.19 (a), indicating that no coupling effect emerges between neighboring waveguides when the gap exceeds 6 μm. If the gap is chosen to be 7 μm, as illustrated in Fig. 2.18 (b), the central waveguide impressively retains over 97% of its initial power even

after propagating 50,000 μm. This outcome significantly affirms its potential to ensure efficient power transmission across considerable distances.

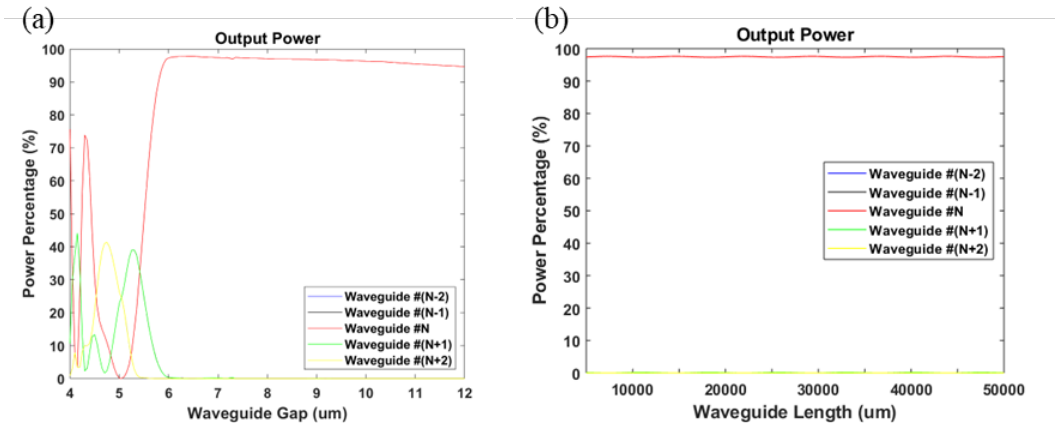

Fig. 2.19. The coupling test between adjacent waveguides. (a) shows the coupling effect vs. waveguide gap. (b) shows the power percentage in each waveguide after propagating up to 50,000 μm.

2.4.1 Layout Design of Rowland Arrayed Waveguide Gratings

The layout of arrayed waveguides of Rowland AWG is generated by Rsoft. When aiming to design the arrayed waveguide layout for the TSP AWG, gaining a comprehensive understanding of the Rowland AWG's layout proves particularly advantageous. In Fig. 2.20, the arrayed waveguide of Rowland AWG can be decomposed into three parts. A bend with angle of $2\theta_i$ and radius of zR_i connects two straight waveguides with length of zL_i on both ends. This geometry is referred to as a V-shaped AWG due to its distinctive configuration. For different arrayed waveguides, the angle θ_i , radius zR_i and length zL_i can be determined by the placement of input/output FPRs, including the separation and rotation. The following expressions can be used to calculate zR_i and zL_i,

$$zR_i sin\theta_i + (R_a + zL_i)cos\theta_i = L_g \tag{2.27}$$

$$(zR_i\theta_i\frac{\pi}{180}+zL_i)-(zR_1\theta_1\frac{\pi}{180}+zL_1)=\Delta L\frac{i-1}{2} \quad (2.28)$$

where R_a is the radius of input/output aperture, L_g is half the separation between two FPRs, and ΔL is the length difference between adjacent arrayed waveguide. The only unknowns are zR_i and zL_i, and by using Eq. (2.27) and (2.28), zR_i and zL_i can be solved. Thus, the layout of V-shaped Rowland AWG can be realized. If the rotation angle of input/output FPRs is chosen to be 90°, the layout becomes more like a U-shaped or horseshoe structure. This arrangement boasts the advantage of having the smallest footprint and the shortest arrayed waveguide length. However, it's worth noting that this design also possesses the largest bending angle and longest bend, which indicates a higher susceptibility to bending losses. On the other hand, opting for a smaller rotation angle for the input/output FPRs, such as 20 degrees, results in a layout characterized by a shorter bend and a smaller bending angle. Nonetheless, this comes at the cost of a larger overall footprint and an extended length of arrayed waveguides. The V-shaped AWG proposed in this work features rotation angle of FPRs around 45° to 60°, as a compromised choice between the aforementioned cases.

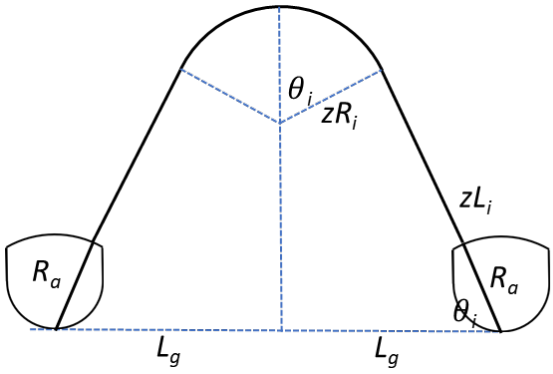

Fig. 2.20. Layout parameters of a V-shaped Rowland AWG

2.4.2 Layout Design of Three-Stigmatic-Point Arrayed Waveguide Gratings

In the case of TSP AWG, it has been addressed that R_a is no longer constant for each arrayed waveguide, it can be calculated once the geometry is determined by aberration theory, and it is presented as R_{TSPi}. Besides, there is an extra length to compensate the geometry difference, a new parameter Δl_i is introduced, representing the extension length of zL_i. The layout schematic for a V-shaped TSP AWG is plotted in Fig. 2.21 (a). The total length of arrayed waveguide before and after extension can be expressed as

$$L_{Ti} = 2(R_{TSPi} + zL_i + zR_i \frac{\pi}{180}\theta_i) \tag{2.29}$$

$$L_{Ti}{}' = 2(R_{TSPi} + zL_i + \Delta l_i + zR_i{}' \frac{\pi}{180}\theta_i) \tag{2.30}$$

where L_{Ti} and $L_{Ti}{}'$ represent the total length of arrayed waveguide, including the distance inside both FPRs. The relation between zR_i and $zR_i{}'$ can be written as

$$zR_i{}' - zR_i = -{}^{\Delta l_i}/_{tan\theta_i} \tag{2.31}$$

Also, $L_{Ti}{}' - L_{Ti} = L_{exi}$, as the extra length of arrayed waveguide after extension. By solving $zR_i{}'$ and Δl_i, the layout of V-shaped TSP AWG can be realized. The layout of a V-shaped TSP AWG with lower resolving power is provided in Fig. 2.21 (b).

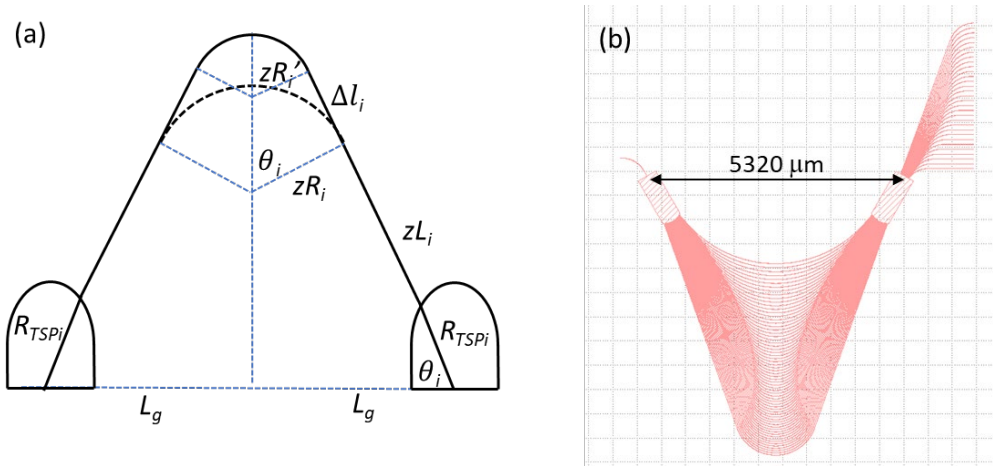

Fig. 2.21. (a) The layout parameters of V-shaped TSP AWG and (b) the final layout of the V-shaped TSP AWG with lower resolving power

To further minimize the required footprint, an alternative layout structure is employed, known as the crossover TSP AWG. The underlying principle here involves the overlap of both input and output FPRs, leading to a reduction in the arrayed waveguide area. This reduction is facilitated by the increased proximity of the apertures of both FPRs, enabling a more compact design overall. The layout schematic of crossover TSP AWG is provided in Fig. 2.22 (a). Similar to the V-shaped case, the arrayed waveguide is also defined by a bend with angle of $180+2\theta_i$ and radius of zR_i connects two straight waveguides with length of zL_i on both ends. The most inner arrayed waveguide is set to be composed of only the bend, meaning $zL_1 = 0$. Thus zR_1 can be derived as

$$zR_1 = {-(L_g + R_{TSP1} cos\theta_1')}\Big/{sin\theta_1'} \tag{2.32}$$

Where $\theta_i' = \theta_i + 90^o$ since the proposed crossover design has both FPRs perpendicular to each other. For other arrayed waveguides, $zL_i \neq 0$, and in a similar way, the bending radius zR_i and length of straight waveguide zL_i can be derived as

$$zR_i = \frac{L_g + (R_{TSPi} + (i-1)\frac{\Delta L}{2} + zR_1 \frac{\pi}{180}\theta_1')cos\theta_i'}{-sin\theta_i' + \frac{\pi}{180}\theta_i' cos\theta_i'} \tag{2.33}$$

$$zL_i = (i-1)\frac{\Delta L}{2} + zR_1 \frac{\pi}{180}\theta_1' - zR_i \frac{\pi}{180}\theta_i' \tag{2.34}$$

Thus, the layout of crossover TSP AWG can be achieved. The layout of a crossover TSP AWG with higher resolving power is provided in Fig. 2.22 (b).

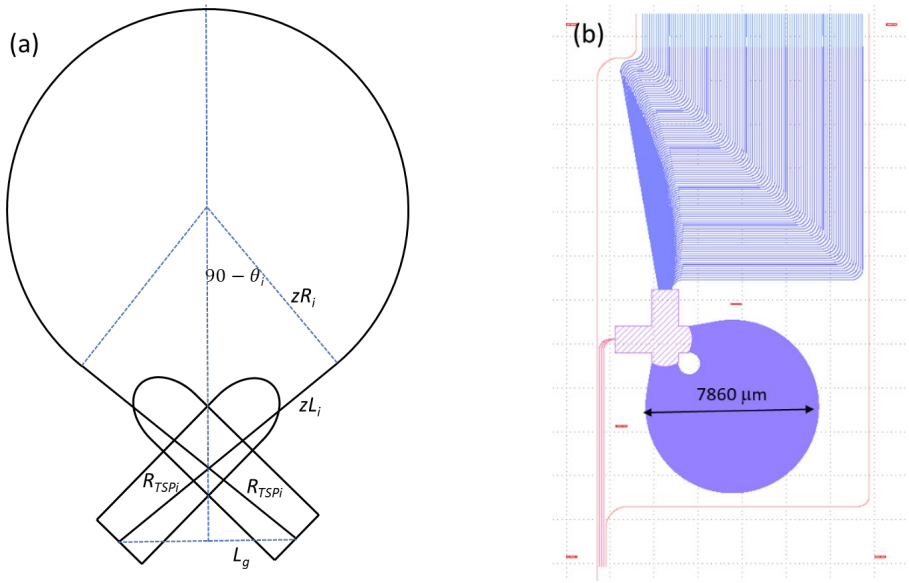

Fig. 2.22. (a) The layout parameters of V-shaped TSP AWG and (b) the final layout of the crossover TSP AWG with higher resolving power

2.5 Experimental Results of Arrayed Waveguide Gratings

A V-shaped TSP AWG with lower resolving power and a crossover TSP AWG with higher resolving power has been fabricated based on the layout discussed in the previous section. The output transmission spectrum and corresponding resolving power of the V-shaped TSP AWG is demonstrated in Fig. 2.23.

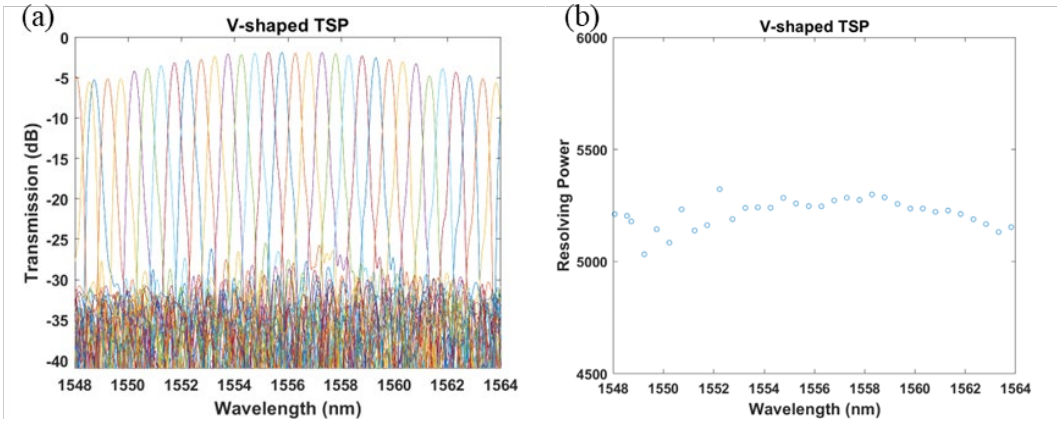

Fig. 2.23. (a) The measured transmission spectrum of V-shaped AWG (lower resolving power) and (b) its corresponding resolving power

The peak transmission at central channels is about -1.9 dB and it gradually decreases by 3 to 4 dB for outer channels. The crosstalk is more than 20 dB lower and the noise level is about -25 to -30 dB. The resolving power peaks at approximately 5,300 and devreases to just over 5,000 at the outer channels. Comparing the measured result to simulation, the spectrum is about 1 dB down across the FSR. Despite the observed increase in crosstalk and higher noise levels in the measured results, it's noteworthy that the result is still in good agreement with the simulation. The defocus aberration stemming from the slight tilt of the flat image surface results in a minor impact on the outer channels. Consequently, the wavelength spacing in these outer channels experiences a slight expansion, leading to a marginal overlap with adjacent channels. It can be observed at the wavelength around 1548.5 nm. Regarding the resolving power, the impact is more pronounced on the outer channels compared to the central ones. The resolving power experiences a decrease from 5,150 to slightly above 5,000 at the outer channels.

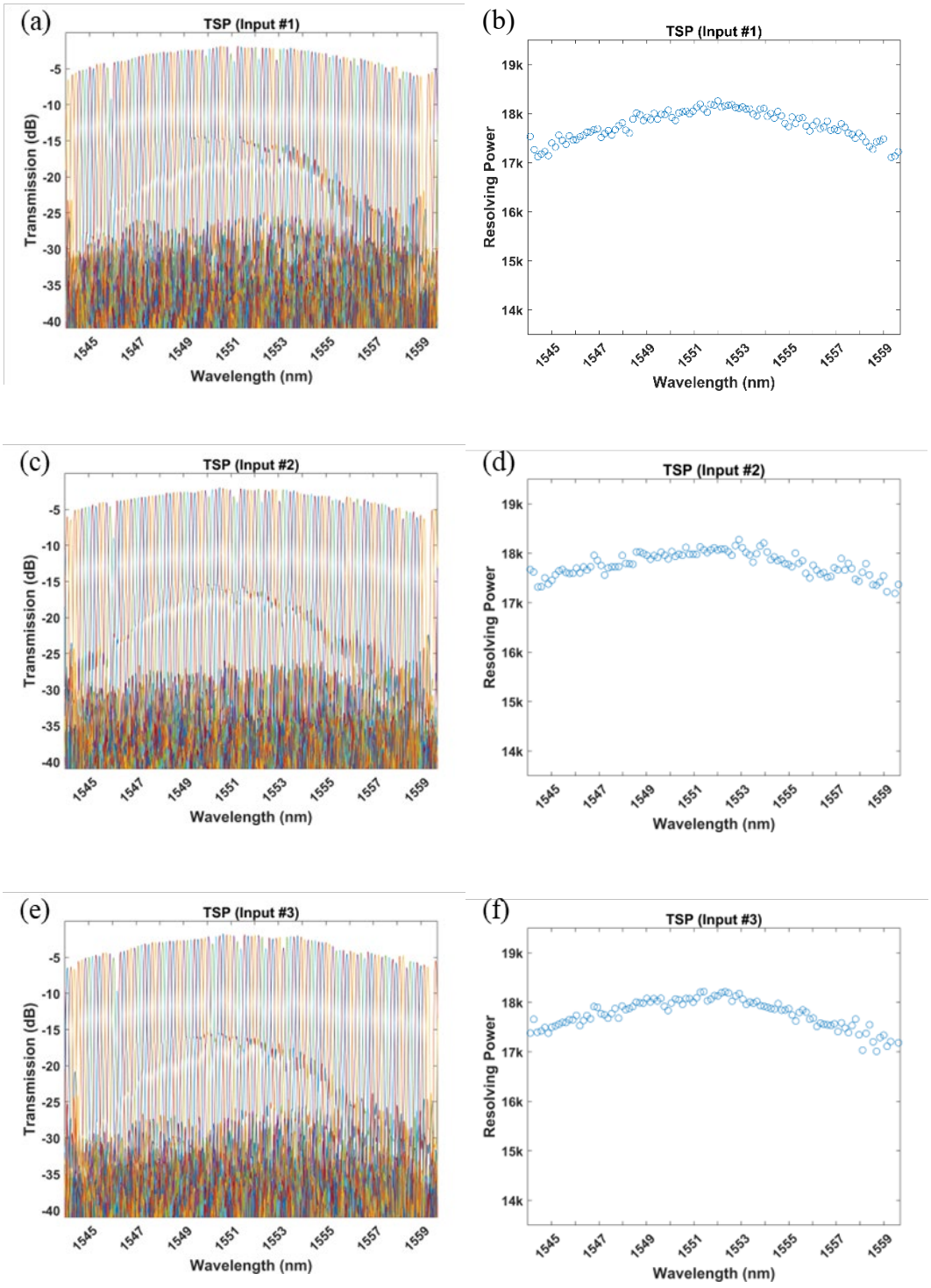

Fig. 2.24. The measured transmission spectra of crossover TSP AWG with higher resolving power. (a), (c) and (e) correspond to input channel #1 to #3; #2 represents the central input. The corresponding resolving power is shown in (b), (d) and (f).

The transmission spectrum of crossover TSP AWG with higher resolving power is displayed in Fig. 2.24 as well as its corresponding resolving power. There are three input channels in this particular design to evaluate the influence of the injection position from the source. The result from input #1 is shown in Fig. 2.24 (a) and (b); the result from input #2, which is the central input channel, is shown in Fig. 2.24 (c) and (d) and the result from input #3 is shown in Fig. 2.24 (e) and (f).

The performance of the central input (#2) and two outer inputs (#1 and #3) is very similar with no evident variation. Among all three input channels, the transmission of the central output channel is around -2.0 dB and transmission of the outer output channels are 4 to 5 dB lower. The side lobes are about 14 to 16 dB lower than the peak transmission and the noise level is near -25 to -30 dB. The slightly lower transmission from some channels is the result of fabrication defects; it is not related to our design.

Among all three input channels, the highest resolving power reaches over 18,000 for the central channels and it remains above 17,000 across all channels. Interestingly, the measured resolving power exceeds that of the simulated one. Again, the measured outcomes closely mirror the simulations, even though the transmission across FSR suffers by approximately 1 dB. The side lobes in the measured spectrum are more prominent which can be attributed to the greater phase error present in the arrayed waveguides.

As for the performance of the TSP AWG in a wider scanning bandwidth, the transmission spectrum, and the resolving power from the central input channel (#2) from 1450 to 1640 nm is illustrated in Fig. 2.25 (a) and (b), respectively. The transmission across the whole range is very consistent without any evident decrease can be observed. There is

a decreasing trend in resolving power with increasing wavelength. This phenomenon indicates that the TSP AWG continues to experience comatic aberration (a form of chromatic aberration) which is in line with expectations, considering that the FSR geometry of the TSP AWG is specifically designed to cancel defocus aberration while other forms of aberration remain. The degradation in resolving power is only 6% across all output channels within one FSR, and slightly increased to over 10% across the whole scanning range if some outlier data are ignored. Compared our Si_3N_4/SiO_2 platform to a similar design based on Ge doped silicon oxide platform, the latter demonstrates about 25% decrease in resolving power across a scanning range from 1500 to 1680 nm which suffer two times more degradation in resolving power [14]. Therefore, Si_3N_4/SiO_2 platform demonstrates higher performance tolerance in terms of resolving power due to smaller comatic aberration.

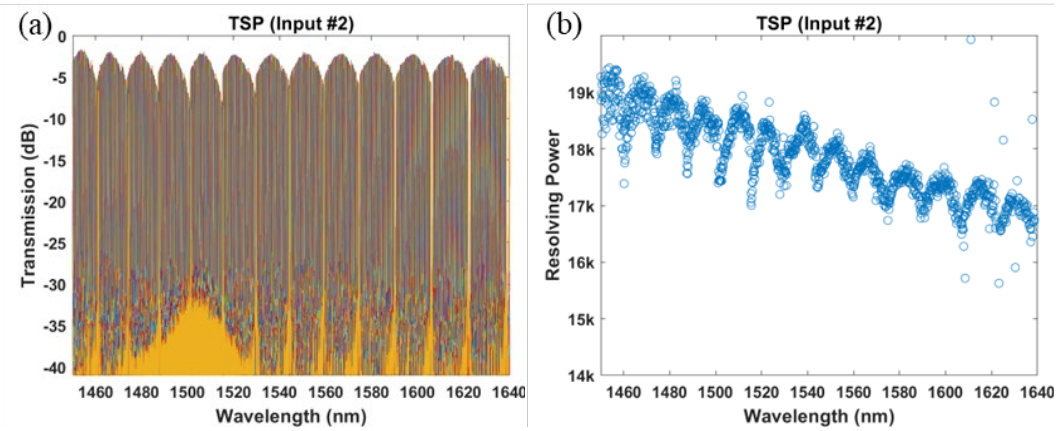

Fig. 2.25. (a) The measured transmission spectrum across the whole scanning range of crossover from central input channel of TSP AWG with higher resolving power and (b) its corresponding resolving power

One major difference in transmission spectrum between the three inputs is the occurrence of a wavelength shift approximately equivalent to one wavelength spacing. The TSP AWG is designed with aberration theory in which the optical path function (OPF) is the core principle. Now, two specific optical paths are proposed; the first one is the light being injected into channel #2 (central channel) and guided through the output channel just next to the central channel. The other optical path is the light being injected into channel #1 and guided through the central output channel. These two optical paths are effectively symmetrical, sharing identical OPFs. Consequently, the output wavelength is anticipated to remain consistent, giving rise to a wavelength shift equivalent to one channel. As for the outer channels, despite not having the exact same optical path due to the polynomial, not circular, apertures of FPRs, the wavelength shift is very close to one wavelength spacing.

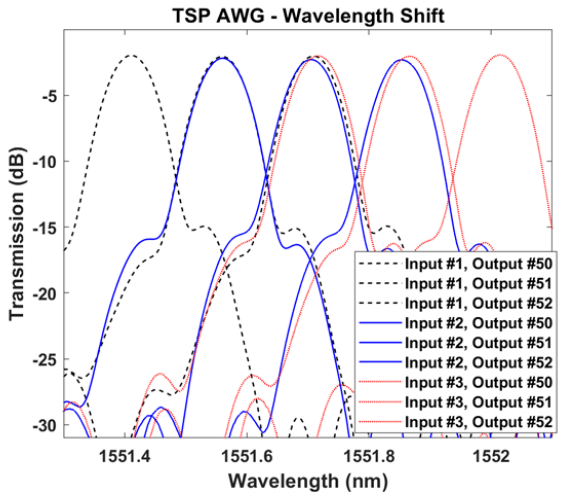

Fig. 2.26. Measured transmission spectrum of crossover TSP AWG from central three output channels. Black dash lines represent input channel #1; blue solid lines represent input channel #2 and red dots represent input channel #3.

To illustrate the wavelength shift, transmission spectrum from the central three output channels is demonstrated in Fig. 2.26. Black dash lines represent the light injected

from input #1; blue solid lines represent input #2 and red dots represent input #3. The wavelength shift about one wavelength spacing can be easily observed. When input signals are simultaneously injected through all three input channels, the resultant output transmission spectrum becomes a composite of three distinct peaks, each separated by one wavelength spacing. This inevitably leads to a significant widening of the 3-dB bandwidth, probably more than three times. As a result, the resolving power experiences a reduction of no less than threefold.

2.6 Summary

Arrayed waveguide gratings (AWGs) are introduced in this chapter, starting from the working principle, the aberration theory to Rowland AWGs and three-stigmatic-point (TSP) AWGs. While Rowland AWGs find extensive application in optical communication, the proposed integrated photonic spectrograph requires the utilization of TSP AWGs due to their characteristic flat image surface.

Our AWG design and devices are based on 100-nm Si_3N_4 on SiO_2 platform. By using the aberration theory, a MATLAB program has been developed to design the geometry of the FPRs of TSP AWGs to minimize the defocus aberration. Moreover, the corresponding length difference of arrayed waveguides and the phase error are all considered into the design process. The simulation of TSP AWG is realized by using another MATLAB script to run BeamPROP tool in Rsoft.

Two kinds of layout have been discussed, including V-shaped and crossover structure. V-shaped structure is based on the structure used in Rsoft while the crossover

structure can further reduce the footprint by overlapping two FSRs and shorten the lengths of arrayed waveguides.

The transmission spectrum of TSP AWGs has been demonstrated and the corresponding resolving power has been calculated. For the lower resolving power design, the wavelength spacing is 0.5 nm and V-shaped structure is adopted. The peak transmission can reach -1.9 dB and the highest resolving power is around 5,300. For the higher resolving power design, the wavelength spacing is 0.15 nm and the crossover structure is used. There are three input channels in this device. The peak transmission is -2.0 dB and the maximin resolving power goes above 18,000 and can remain above 17,000 across all channels. The side lobes are prominent due to larger phase error. The performance from all three input channels is very consistent, and no significant decrease in transmission or resolving power can be observed. Also, Si_3N_4/SiO_2 platform proves to be a great platform for AWG because of larger performance tolerance, suffering less comatic aberration. However, wavelength shift of one wavelength spacing has been noticed.

Chapter 3 Cascaded Arrayed Waveguide Gratings

3.1 Introduction of Cascaded Arrayed Waveguide Gratings

3.1.1 Overview of Cascaded Arrayed Waveguide Gratings

The applications of arrayed waveguide gratings (AWGs) have been discussed in the previous chapter, such as multiplexers/demultiplexers and signal routers in optical networks, optical sensing, quantum computing and spectroscopy. One of the advantages of developing miniaturized optical systems, including integrated AWGs, is to reduce footprint while maintaining performance and therefore, it gathers increasing attention in the development of integrated on-chip photonic devices [15-16].

However, there is a limitation in designing AWG with high resolving power as well as large free spectral range (FSR) at the same time due to the physical constraints and increased optical loss at the outer channels. To address these challenges and transcend limitations, researchers have pioneered a range of techniques in the design of AWGs [17-19]. Among the prominent strategies is the adoption of cascaded AWGs, where the device comprises two AWG stages with distinctive FSRs and resolving powers. The initial stage is referred to as the primary stage AWG, while the other one is referred as the secondary AWG. There are two major design approaches in cascaded AWGs; The design parameters are displayed in Table II (the estimation values are based on the V-shaped Rowland AWGs of the same parameters) and the schematic of concept cascaded AWGs are illustrated in Fig. 3.1.

TABLE II DESIGN PARAMETERS OF CONCEPT CASCADED AWGS

Parameters	Description	Design 1 (Primary/Secondary)	Design 2 (Primary/Secondary)
N_{AWG}	Number of AWG	1/51	1/5
N_{in}	Number of input channels	1/1	1/1
N_{out}	Number of output channels	51/5	5/51
FSR	Free spectral range	20/100 nm	100/20 nm
λc	Central wavelength	1550/1550 nm	1550/1550 nm
$\Delta\lambda$	Wavelength spacing	0.4/20 nm	20/0.4 nm
R_{est}	Estimated resolving power	10k/150	150/10k
A_{est}	Estimated Area (for one AWG)	7.5 x 7.5 mm^2/ 0.45 x 0.75 mm^2	0.45 x 0.75 mm^2/ 7.5 x 7.5 mm^2

Design 1 consists of a primary AWG characterized by high resolving power, accompanied by multiple secondary AWGs with lower resolving power. The primary AWG's larger footprint is a result of its intended high resolving power and relatively smaller FSR, while the secondary AWGs possess compact footprints due to their lower performance yet notably larger FSR. The wavelength spacing of the secondary AWGs is

aligned with the FSR of the primary AWG, ensuring that each output channel of the secondary AWGs covers one wavelength within the primary stage's FSR as well as the corresponding spectral orders. The advantage of Design 1 is relatively small overall footprint due to only the primary AWG featuring high resolving power and larger footprint, but the main disadvantage is the discrete output spectrum at the output image surface.

Design 2 presents an opposite arrangement to Design 1, and it is composed of a single primary AWG with lower resolving power and a smaller footprint. This configuration is designed to separate the desired bandwidth into a limited number of channels, directing optical signals to the secondary stage while effectively filtering out unwanted wavelengths. Each channel of the primary AWG covers the entire FSR of the secondary AWG. Consequently, the primary AWG typically boasts a broader FSR, whereas the secondary AWG maintains a considerably smaller FSR, designed with narrower wavelength spacing to achieve the intended resolving power. Design 2 features a significantly larger overall footprint, but it realizes a continuous output spectrum at the image surface.

A continuous output spectrum is preferred for astronomical application due to the convenience of data analysis after acquiring the raw transmission data. Hence, Design 2, which is one small primary AWG with multiple large secondary AWGs, is chosen to be implemented in this chapter despite the relatively large footprint.

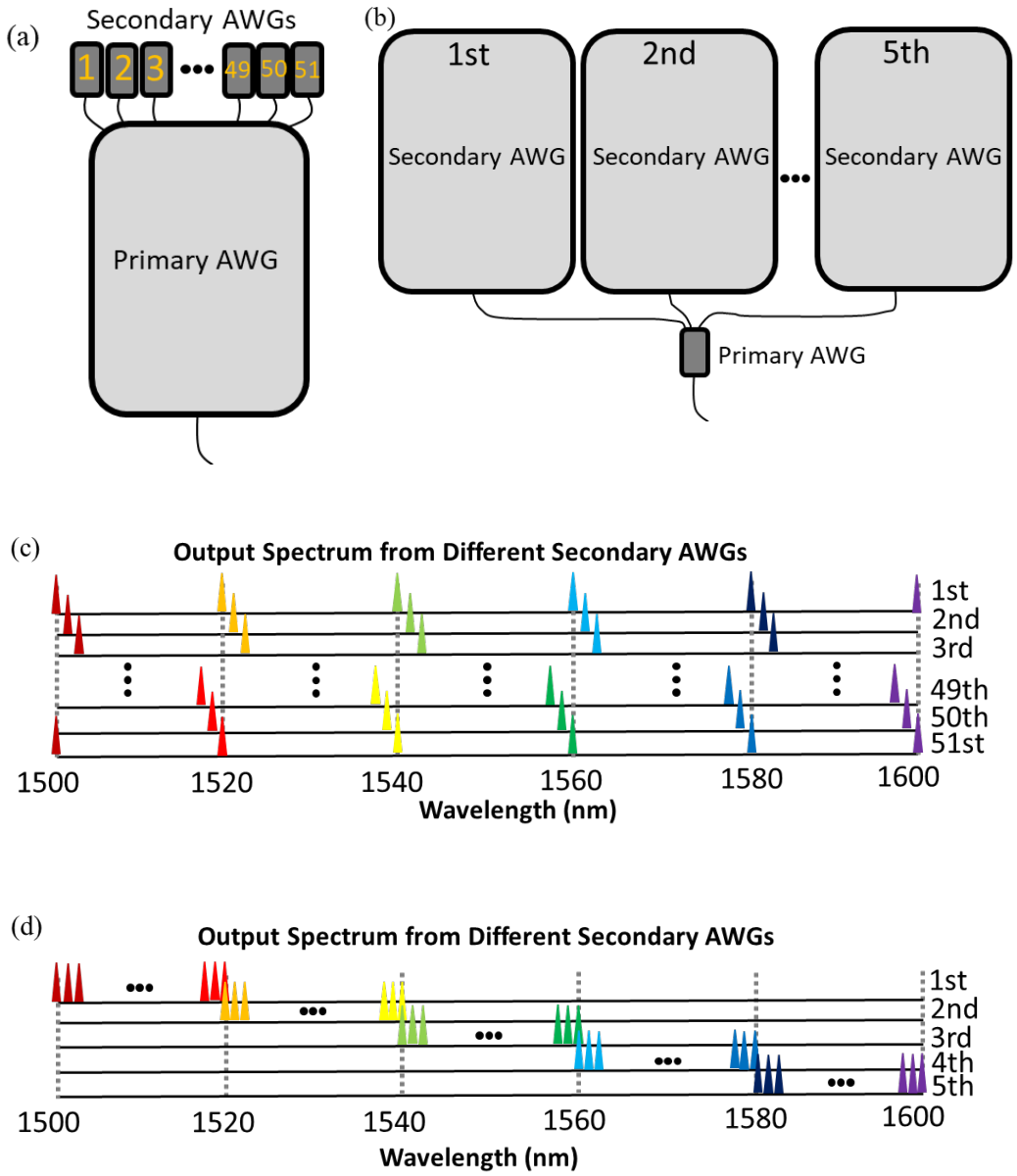

Fig. 3.1. The design concept of cascaded AWGs. (a), (b) illustrates the schematic of Design 1 and Design 2, respectively. And the corresponding output pattern obtained at the output of secondary AWG are shown in (c) and (d).

3.1.2 Flat-Top Arrayed Waveguide Gratings

The previously discussed Design 2 for cascaded AWGs offers a strategy to expand the FSR while maintaining resolving power. As an initial investigation toward realizing this concept, a smaller cascaded AWG is implemented for proof of concept. The primary AWG is configured with an FSR of 50 nm and 5 output channels, while the secondary AWG is targeted to achieve a resolving power of approximately 5,000 with an FSR of 10 nm. The specific design parameters for this cascaded AWG are detailed in the table below.

TABLE III DESIGN PARAMETERS OF IMPLEMENTED CASCADED AWGS

Parameters	Description	Primary	Secondary
N_{AWG}	Number of AWGs	1	5
N_{in}	Number of input channels	1	1
N_{out}	Number of output channels	5	21
FSR	Free spectral range	50 nm	10 nm
λc	Central wavelength	1550 nm	1550 nm
$\Delta\lambda$	Wavelength spacing	10 nm	0.5 nm
R_{est}	Estimated resolving power	250	5k

The inherent output Gaussian profile of the Rowland primary AWG contributes to a significant amount of insertion loss at the channel cross-points. The transmission

spectrum of a primary Rowland AWG with the above parameters from Rsoft simulation is demonstrated in Fig. 3.2 (a). The peak transmission measures about -1.1 dB while it drops to approximately -3.5 dB for the outer channels. But the huge drawback from this primary AWG is the substantial loss at channel cross-points which can reach as bad as -14.1 dB. Therefore, the severe loss poses a huge limitation on the overall performance of the cascaded AWG, given that the input level to the secondary AWG is already below -14 dB for some specific wavelengths around the channel cross-points, even before accounting for the insertion loss of the secondary AWG. The complete response of the corresponding Rowland cascaded AWG for one FSR is shown in Fig. 3.2 (b). The peak transmission is around -2.2 dB, but the outer channels are seriously affected by the low input level from the primary stage, and the lowest transmission is less than -15 dB. As a result, the output response from primary AWG is required to be wider and preferably flat-top profile (flat response) to overcome the large insertion loss at the channel cross-points.

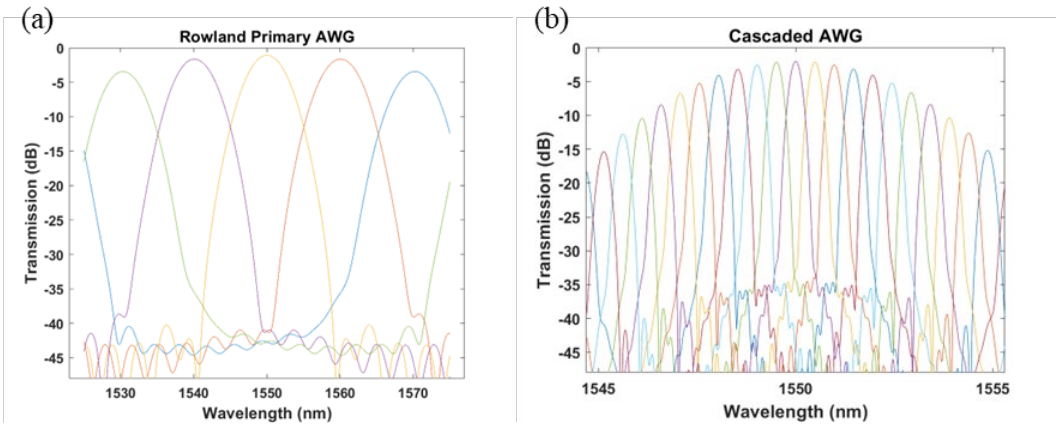

Fig. 3.2. (a) The simulated transmission spectrum of a primary Rowland AWG and (b) the simulated transmission spectrum of a cascaded Rowland AWG with the design parameters provided in Table III.

Several implementations of AWGs have been reported to realize such flat-top output response, including but not limited to changing the geometry of the taper regions [20-21], cascading with some other devices [22-23], redesigning the output Rowland FPR [24], adding an interleave filter in front of the primary AWG [25]. Sheng et al. and Song et al. proposed flat-top AWG by using auxiliary waveguides between arrayed waveguides at output aperture [26-27]. Fondeur et al. added extra loss intentionally to several arrayed waveguides to achieve wide output response [28]. Ho et al. changed the geometry of output FPR by using multiple Rowland circles [29]. MMI was widely adopted to modify input power profile to realize flattened response by several groups, such as Soole et al, and Fan and Gao. [30-31]. Hassan et al. used a cascaded AWG to achieve a flat-top AWG [32].

However, despite the various attempts proposed, none of them have managed to achieve a flat response without encountering trade-offs such as compromising throughput by 5-10 dB or unresolved issues such as significant loss at the channel cross-points. Otherwise, heaters are employed to slightly adjust the refractive index of arrayed waveguides to optimize the phase control by changing the temperature of arrayed waveguides. Hence, in this chapter, a novel approach to attain a flat-top response in primary AWG design is introduced, involving modifications to the power profile of arrayed waveguides along the input aperture and precise control of the phase distribution of arrayed waveguides along the output aperture. Detailed insights into this innovative design will be demonstrated in the upcoming sections.

3.2 The Fabrication Details of Cascaded Arrayed Waveguide Gratings

The cascaded AWGs shares the same 100-nm Si_3N_4/SiO_2 platform mentioned in the previous chapter. The width of the waveguides remains at 2 μm and the input/output waveguides are also tapered down to 0.6 μm. By adopting the same positive resist (ZEP-520A) approach, the complete fabrication details can be found in Chapter 2.2.

3.3 Design of Cascaded Arrayed Waveguide Gratings

There are several design criteria for designing cascaded AWGs tailored for integrated photonic spectrograph applications, including flat-top response for primary AWG and flat image surface at the output of secondary AWG. While the electric field profile at the output image surface can be understood as the Fourier transform of the electric field profile at the output aperture, a flat-top response could be realized once the electric field at the image surface is a square function and the corresponding electric field at the output aperture follows a sinc distribution. The phase distribution is determined by using Gerchberg-Saxton (G-S) algorithm [], which will be introduced in the next section. In addition, it is preferred that all the output FPRs of secondary AWGs can be positioned on the same flat image surface as well as in close proximity to each other. Thus, the TSP AWG is used as secondary AWG and the placement of output FPRs can be carefully designed by changing the routing of arrayed waveguides.

3.3.1 Gerchberg - Saxton Algorithm

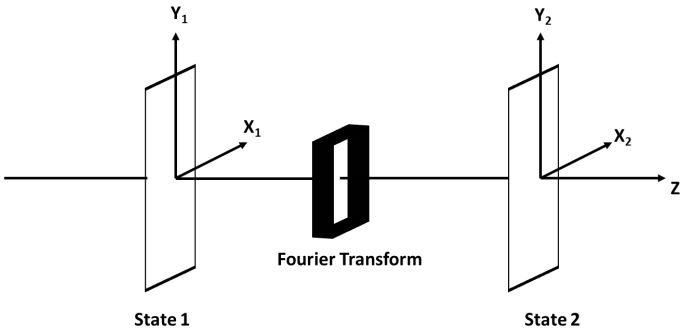

Fig. 3.3. The schematic of an image system to illustrate Gerchberg-Saxton algorithm.

In 1972, Gerchberg and Saxton introduced a groundbreaking algorithm aimed at solving the phase-retrieval problem inherent in Fourier-transform image systems [33], This algorithm computes the phase of a wave function, particularly when the intensities within the diffraction and imaging planes of an imaging system are established. To apply the Gerchberg-Saxton (G-S) algorithm to accommodate the distinctive case of the output FPR, a tactical approach involves assigning state 1 to the output aperture, while the output image surface is designated as state 2. The schematic of the system is illustrated in Fig. 3.3, and the wave function at state 1 (U_1) and 2 (U_2) can be expressed as

$$U_1(\boldsymbol{X_1}) = \rho_1(\boldsymbol{X_1})\exp\left[i\phi_1(\boldsymbol{X_1})\right] \tag{3.1}$$

$$U_2(\boldsymbol{X_2}) = \rho_2(\boldsymbol{X_2})\exp\left[i\phi_2(\boldsymbol{X_2})\right] \tag{3.2}$$

where ρ_1 and ρ_2 is the amplitude profile of the wave function in state 1 and 2, respectively while $\phi_1$and ϕ_2 is the corresponding phase distribution. The coordinate of the points at state 1 and 2 can be expressed as $\boldsymbol{X_1} = (x_1, y_1)$ and $\boldsymbol{X_2} = (x_2, y_2)$.

The relation between wave function at state 1 and 2 can be determined by a linear transfer function *G*, which is Fourier transform in our case, and hence, $U_2(\boldsymbol{X_2})$ can be written as

$$U_2(\boldsymbol{X_2}) = \int G(\boldsymbol{X_2}, \boldsymbol{X_1})\, U_1(\boldsymbol{X_1}) d(\boldsymbol{X_1}) \tag{3.3}$$

And it can be further written in a compact form

$$U_2(\boldsymbol{X_2}) = \hat{G} U_1(\boldsymbol{X_1}) \tag{3.4}$$

In addition, ρ_1, ρ_2, ϕ_1 and ϕ_2 can be expressed as the following.

$$\rho_1 = \left|\hat{G}^{\dagger} U_2\right| \tag{3.5}$$

$$\rho_2 = \left|\hat{G} U_1\right| \tag{3.6}$$

$$\phi_1 = \arg\left(\hat{G}^{\dagger} U_2\right) \tag{3.7}$$

$$\phi_2 = \arg\left(\hat{G} U_1\right) \tag{3.8}$$

where the operator † is the Hermitian conjugate. Both amplitude profiles of the wave function at state 1 and 2 are already known; ρ_2 is the square function while ρ_1 is sinc function. To initiate the iteration, a random phase distribution between $-\pi$ and π is generated for state 1. By doing the Fourier transform of U_1, an U_2 can be obtained. Subsequently, after replacing the calculated ρ_2 with square function and executing an inverse Fourier transform of the updated U_2, an updated U_1 can be derived. Similarly, the calculated ρ_1 is replaced by the sinc function and the procedure completes the first iteration. The repetition of this procedure across multiple iterations leads the phase distributions ρ_1 and ρ_2 to converge toward a specific set of values. Thus, phase distribution at output

aperture ρ_1 can be acquired. The flow chart of the iterative G-S algorithm is shown in Fig. 3.4.

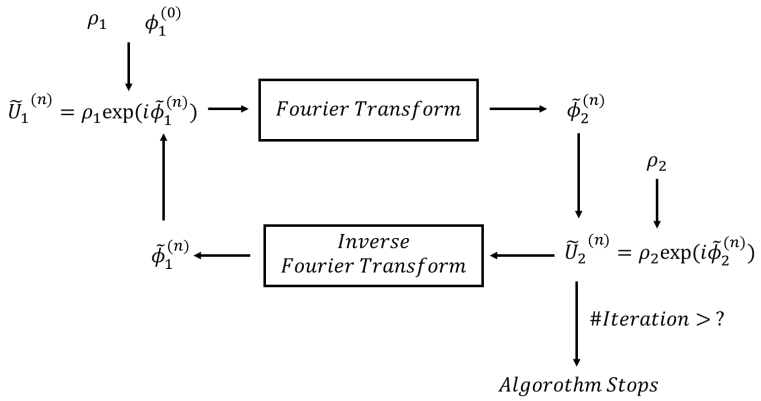

Fig. 3.4. The flow chart of Gerchberg-Saxton algorithm.

3.3.2 Design and Simulation of Flat-Top Primary Arrayed Waveguide Gratings

A simple design principle, based on the power profile of arrayed waveguides along the input aperture and the phase distribution of arrayed waveguides along the output aperture, is proposed to attain a flat-top response for primary AWG. This approach omits the use of multi-mode interferometers (MMIs), Mach-Zehnder interferometers (MZIs), or heaters. The only modification is the taper widths connecting input FPR and arrayed waveguides to create the intended power profile and the lengths of arrayed waveguides to adjust the phases at the output aperture determined by the G-S algorithm.

The primary AWG consists of 5 output channels with wavelength separation of 10 nm and the FSR of 50 nm, and the number of arrayed waveguides is chosen to be 13, 21, 29 and 53. The first three cases features the same radius of input aperture R_a while the

same geometry of input FPR are not able to accommodate more arrayed waveguides, the 53-arrayed waveguide case implements another design with lower grating order. Grating order m can be expressed as

$$m = \frac{\lambda_C}{N_{out} \cdot \Delta\lambda \cdot DF} \tag{3.9}$$

where *DF* is dispersion factor, defined as the ratio of group effective index to the refractive index of array waveguides. In this configuration, the total number of output channels is defined as 21, but the secondary AWGs will be linked to only the central 5 channels. This arrangement is aimed at reducing the transmission loss experienced by the outer channels. The positions of the central 5 channels are relatively well-centered within the larger FPR, which contributes to minimizing losses. The R_a is increased to over 700 μm from 172 μm for the previous three cases. Opting for fewer arrayed waveguides results in a smaller footprint, while a greater number of arrayed waveguides offers increased flexibility when performing the Fourier transform. A Rowland structure is adopted for primary AWG since it does not need to attach cross-dispersion optics. After setting up all the different cases in Rsoft, the power profiles along the input aperture can be simulated by using the BeamPROP tool and the Gaussian power profile can be verified. In addition, the targeted transmission spectrum is a perfect square function and the targeted power profiles can be calculated by simply conducting an inverse Fourier transform. A comparison between the Gaussian profiles simulated using Rsoft and the calculated power profiles is depicted in Fig. 3.5. The simulated power profiles are normalized to 1, while the targeted power profiles are normalized to the total power of the simulated profiles for each case. The x-axis is labeled as the array waveguide index, where 0 represents the central

arrayed waveguide and its nearest neighboring arrayed waveguides are 1 and -1, respectively.

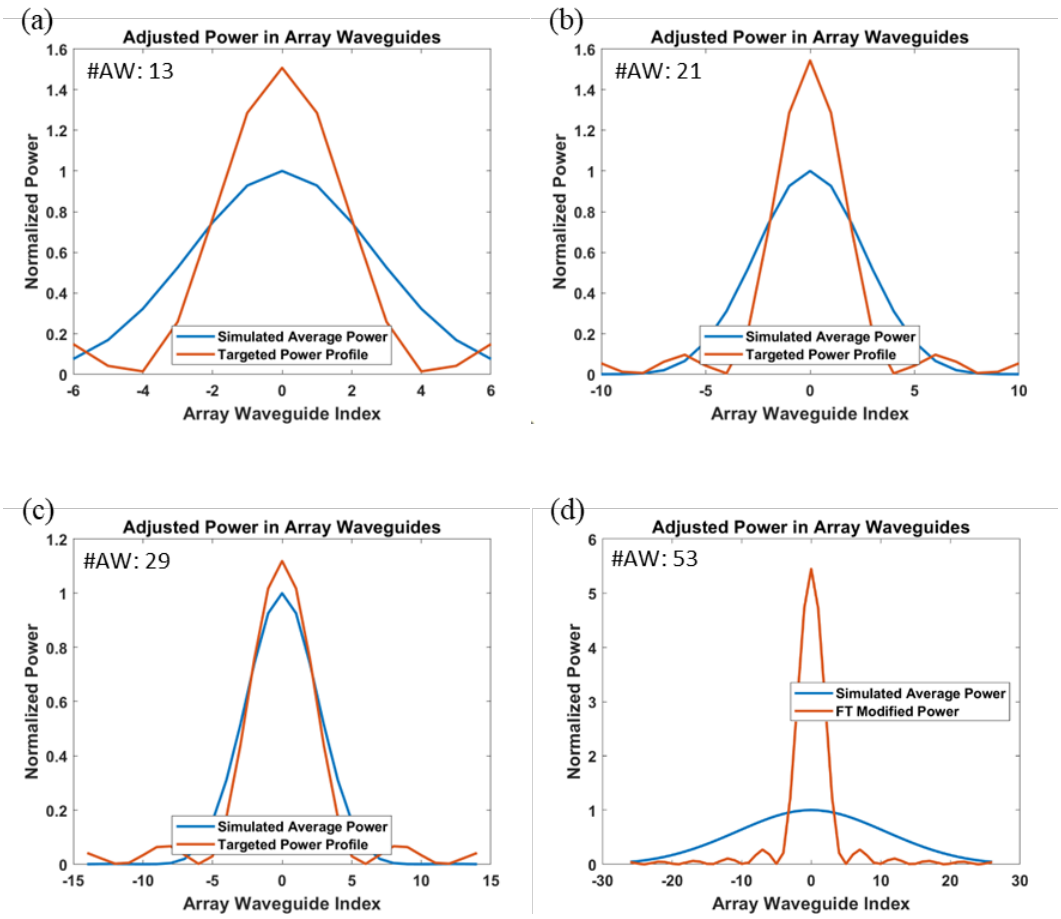

Fig. 3.5. The comparison of power profile at input aperture with the following number of arrayed waveguides: (a) 13, (b) 21, (c) 29, and (d) 53 arrayed waveguides.

The peak of targeted power profile increases with increasing number of arrayed waveguides except for the case of 29 arrayed waveguides. The scenario with 29 arrayed waveguides occupies the majority of the input aperture, resulting in a few outer arrayed waveguides on each side carrying only minimal light. Consequently, this setup generates a relatively narrower Gaussian profile as simulated by Rsoft. This 29-arrayed waveguide

configuration seems promising because the targeted power profile closely resembles the simulated Gaussian profile. On the contrary, achieving the power profile of 53 arrayed waveguides appears challenging, requiring the incorporation of Y-branches to combine the power of multiple central arrayed waveguides. However, this approach could potentially necessitate further investigation to accurately retrieve the power and phase information at the end of the Y-branch waveguides. For the purpose of validating the flat-top primary AWG concept, we aim to maintain simplicity and compactness in the design. Consequently, we will focus on the first three cases for further simulation. Next, to investigate the influence of Gerchberg-Saxton algorithm, an additional simulation was conducted by implementing the algorithm on the output FSR. The simulated output spectrum can be obtained by assigning the power profile at the output aperture to be the Gaussian profile acquired from previous simulation and applying a square function to the power profile at output image surface. After about 100 to 200 iterations, the calculated phase distribution on both output aperture and output image surface converges which allows us to plot the power profile of the output transmission spectrum, demonstrated in Fig. 3.6. The power percentage, defined by the ratio of power within the square function to the total power of the calculated profile, is also included in the figure. The resulting peaks in all three cases exhibit similar broad responses, without showcasing a true flat-top response. Across all three cases, the power percentage remains approximately between 72% to 76%, indicating a degradation in throughput of about 1.5 dB. It can be anticipated that outer channels may experience more significant degradation due to the calculated profile.

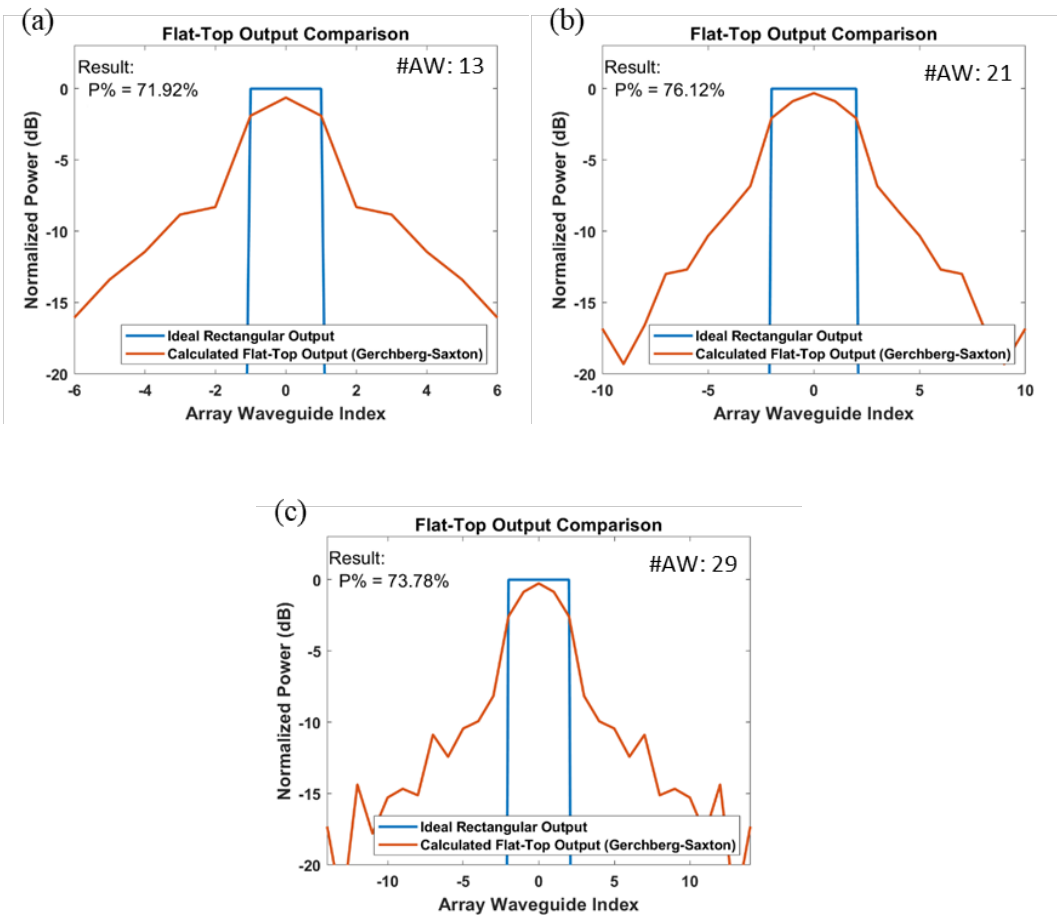

Fig. 3.6. The simulated output power profile based on Gerchberg-Saxton algorithm with the power profile at output aperture set to be Gaussian. (a), (b) and (c) represents the case of 13, 21, and 29 arrayed waveguides.

Achieving a flat-top response requires more than just adjusting the phase distribution; it requires modifications to the power profile as well. This entails the need for a redesign of the geometry of the input FPR or tapers at the input aperture. To streamline the design process, the case of 13 arrayed waveguides is chosen for further consideration. This choice is based on the similarity in simulation results for all three cases, with no observable superior power profile. Additionally, the 13 arrayed waveguides case offers a simpler structure and a smaller footprint. By conducting a Rsoft BeamPROP simulation on

input FPR incorporating linear tapers of varying widths along the entire input aperture, the corresponding power profile with various taper width at different positions can be obtained. The schematic of the taper placement and the corresponding simulated power profile are provided in Fig. 3.7 (a) and (b). The default taper width in Rsoft is set to be 6 μm, and the taper width is varied from 2 μm to 10 μm with a step of 2 μm while taper slope remains unchanged. The narrowest case is 2 mm, which is basically attaching straight waveguides at the input aperture since the width of arrayed waveguides is 2 μm as well.

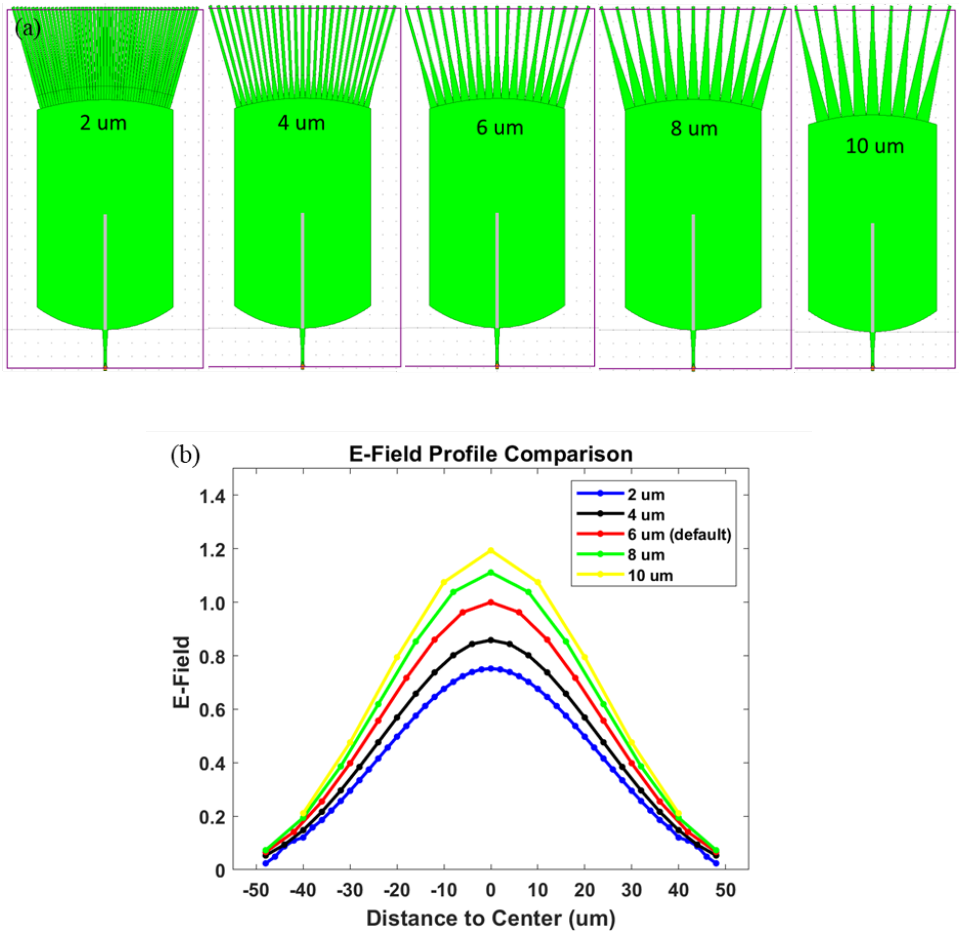

Fig. 3.7. (a) The taper placement along the input aperture with various taper widths and (b) the comparison of the corresponding E-field simulation.

The simulated power profile data from different taper widths are employed to derive the optimal taper width, as depicted in Fig. 3.8. However, narrower than 0.2 μm, the two tapers, the third tapers on both sides, have been intentionally deleted due to two specific reasons. The first reason for excluding these tapers is the minimal power that is guided through the narrowest tapers, making their omission negligible in terms of the power profile. The second reason is related to potential concerns about coupling between the arrayed waveguides. Based on the coupling test of straight waveguide demonstrated in previous chapter, the smallest gap between straight waveguides while remaining coupling free is 6 μm. Considering the geometry of the input FPR and the curvature of input aperture, the tapers are fan-out while reducing the width down to the width of arrayed waveguides, 2 μm. As a result, the gaps between these tapers exceed the 6 μm threshold over a short distance. However, if a taper were to widen as it fans out, the gaps between that taper and its adjacent tapers would remain narrow for a more extended distance. This could increase the risk of coupling between the tapers, potentially leading to a compromised designed power profile.

The calculated taper width is presented in Fig. 3.8 (a) and the FPR layout is provided in (b) featuring the same radius of input aperture of R_a. Due to the two dropped tapers, the number of arrayed waveguides reduces to 11. The power simulation by Rsoft BeamPROP tool has been carried out to demonstrate the comparison between the simulated power profile from the designed tapers and the targeted sinc power profile. The total power guided through arrayed waveguides is expected to be less than 90% which is the total power obtained by using default 6 μm tapers with Rowland structure without any modification. The power profile comparison is illustrated in Fig. 3.8 (c), where the targeted sinc power

profile is normalized to be around 90%, the power obtained by default tapers. The total power from our design is simulated to be around 82%, which represents less than 0.5 dB loss due to the imperfection of power profile. By the way, the propagation loss along the arrayed waveguides is neglected and the power profile simulated at the input aperture will be carried over to the output aperture.

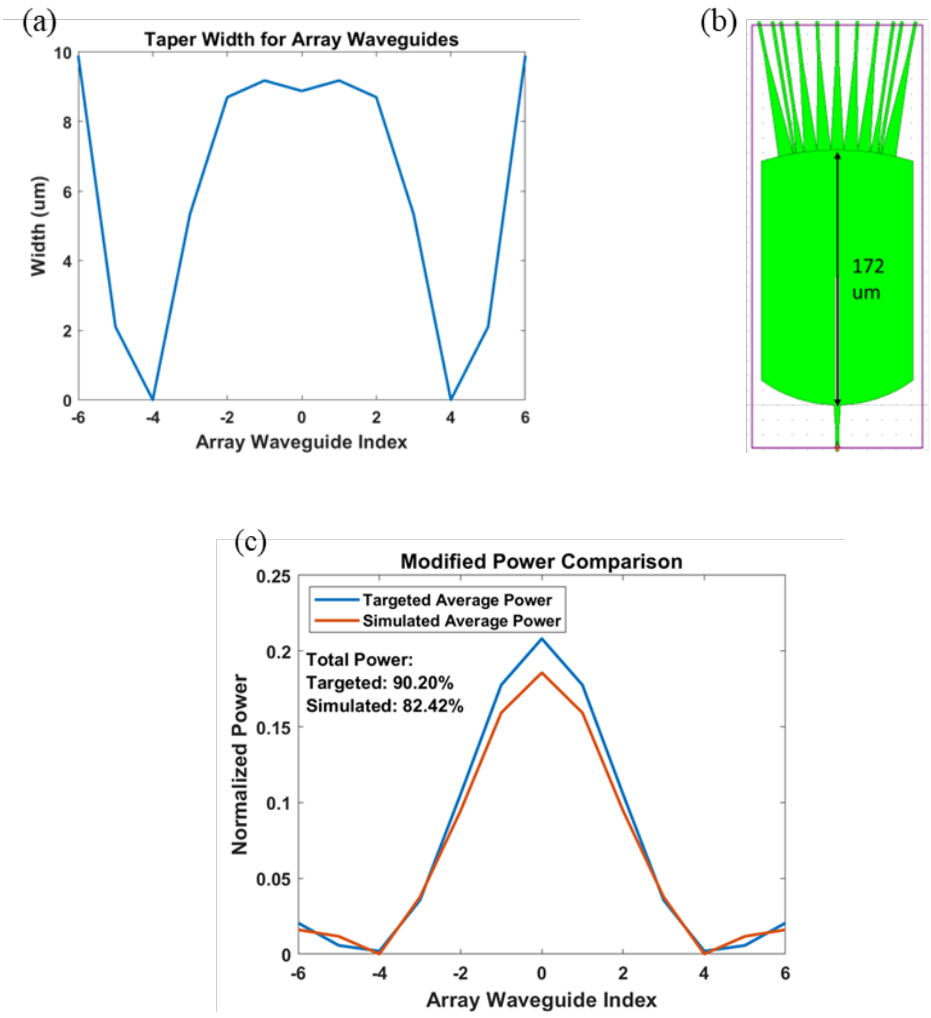

Fig. 3.8. (a) The calculated taper widths for each arrayed waveguide, and (b) the schematic of input FPR with reduced number of arrayed waveguides. (c) The comparison of targeted and designed power profiles

Subsequently, employing the G-S algorithm and integrating the simulated power profile at the output aperture with the square function at the output image surface, the phase distribution at the output aperture can be established after approximately 100 to 200 iterations. Notably, since two arrayed waveguides have been omitted, the associated phase information for those waveguides holds no significance. The phase distribution along output aperture derived from G-S algorithm is demonstrated in Fig. 3.9 (a), while the output power profile derived from G-S algorithm is in Fig. 3.9 (b), indicating that over 89% of the power will be inside the square function, showing a promising sign for an actual flat-top AWG simulation or even fabricated AWG device.

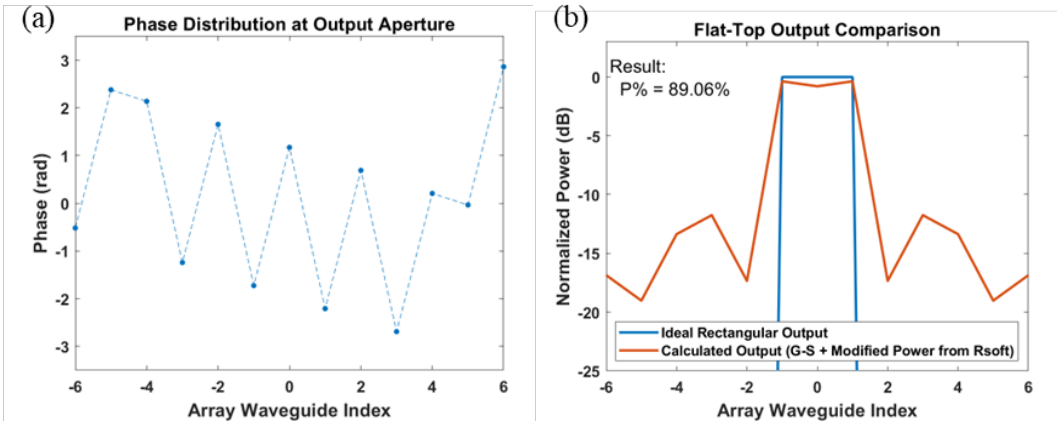

Fig. 3.9. (a) The phase distribution along output aperture derived from G-S algorithm and (b) the output power profile derived from G-S algorithm.

Prior to the final output transmission spectrum simulation, it is necessary to account for the phase difference between the calculation based on aberration theory and the simulation executed using Rsoft, as elaborated in section 5.3.2. In the case of flat-top primary AWG, the tapers along the input aperture and those along the output aperture exhibit significant differences. Specifically, while the taper slopes remain consistent with

those from the Rowland AWG, the taper widths and positions along the input aperture have been adjusted. Consequently, the compensation needed to mitigate the phase error at the input/output aperture varies. By considering both the phase error at the input/output aperture and the predetermined phase distribution at the output aperture, an array of additional lengths is computed and subsequently incorporated into the total lengths of the arrayed waveguides.

Lastly, the output transmission spectrum of the designed flat-top primary AWG can be simulated using the BeamPROP tool within Rsoft, controlled by a custom MATLAB script. In the case of the flat-top primary AWG, the output transmission spectrum is achieved through the execution of BeamPROP on the output FPR. This involves utilizing the modified power profile and the meticulously designed phase distribution.

Additionally, the taper width along the output image surface (the interface between the output FPR and output waveguides) is typically set to 4 μm, linearly tapering down to 2 μm to match the width of the output waveguides. However, a noticeable gap between adjacent tapers, measuring 2 μm, has been observed, as illustrated in Fig. 3.10 (a). In an effort to maximize light collection, the tapers are widened to 6 μm, effectively covering all gaps between tapers, while retaining the original taper slope, as depicted in Fig. 3.10 (b). The corresponding effect will be evaluated by the simulation of the output transmission spectrum.

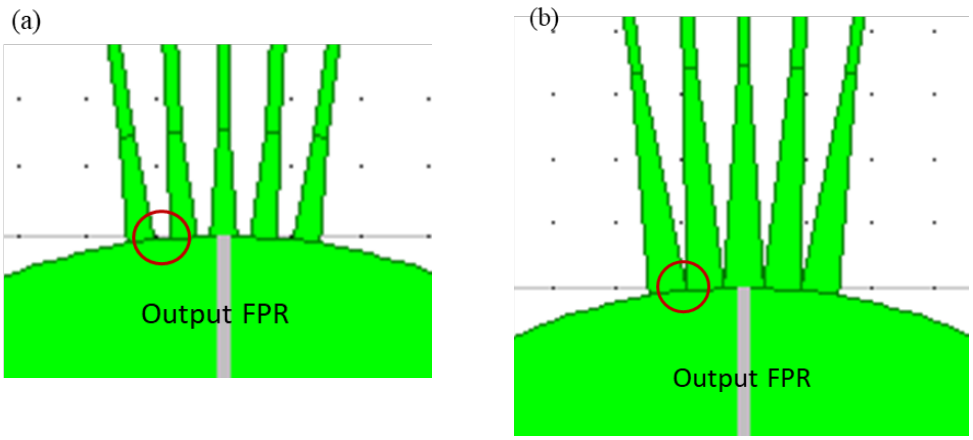

Fig. 3.10. (a)The original tapers along output aperture are 4 μm in width and leaving some gaps, as in the circle, between tapers. (b) The tapers are widened to cover the gaps between tapers, as in the circle.

The simulated transmission of primary AWG derived by G-S is plotted in Fig. 3.11 (a) as well as the modified wider taper counterpart in (b). (c) shows the AWG derived by the combination of G-S algorithm and modified power profile (d) is the wider taper counterpart. As is observed from the figures, primary AWGs derived by both G-S and modified power profile perform the best in terms of flattened response. The peaks are widened, and the 3-dB bandwidth is enlarged to 9-10 nm. The peak transmission is about -2.4 dB with original tapers and -1.6 dB with widened tapers, which is impressive. Especially when it comes to transmission at channel cross-points, the lowest transmission is improved to around -8 dB. The AWGs derived only by the G-S algorithm perform a lot worse though. The peak transmission is not as high compared to the AWGs modified by both G-S and the power profile. The 3-dB bandwidth is not as broad either. Besides, the crosstalk is only -17 to -18 down. Overall, the performance is worse in almost every

category. The wider output taper variant displays higher transmission at the center of the peaks, suggesting that the broader output taper enhances light collection.

In order to compare how much improvement those modified primary AWGs show, the transmission of Rowland AWG is provided in Fig. 3.11 (e), from which the highest peak transmission can be observed around -1 dB and the outer channels being 2 to 3 dB lower. In addition, Rowland AWG has the best crosstalk, showing almost 40 dB lower. The most significant drawback lies in the substantially reduced throughput observed at the channel cross-points, plummeting to levels as low as -14 dB. Flat-top primary AWGs are designed to overcome the low throughput at channel cross-points. The maximum transmission profile is plotted in Fig. 3.11 (f) to compare the peak profiles. As can be observed, the Rowland AWG features very high peak transmission but performs poorly at channel cross-points. In contrast, the primary AWG employing both the G-S algorithm and the modified power profile demonstrates significant enhancement in terms of 3-dB bandwidth and transmission at channel cross-points. The peak transmission is lowered by only 1 to 2 dB but the improvement at channel cross-points is about 6 dB. As for resolving power, it is not a big concern for our primary AWG because it is designed to feature flattened response and wide 3-dB bandwidth. Among all the primary AWGs discussed here, only the Rowland AWG has resolving power higher than 250. In contrast, the AWGs with both the G-S algorithm and the modified power profile exhibit lower resolving power, ranging from 160 to 170. A table summarizing the simulated results from all AWGs is listed below.

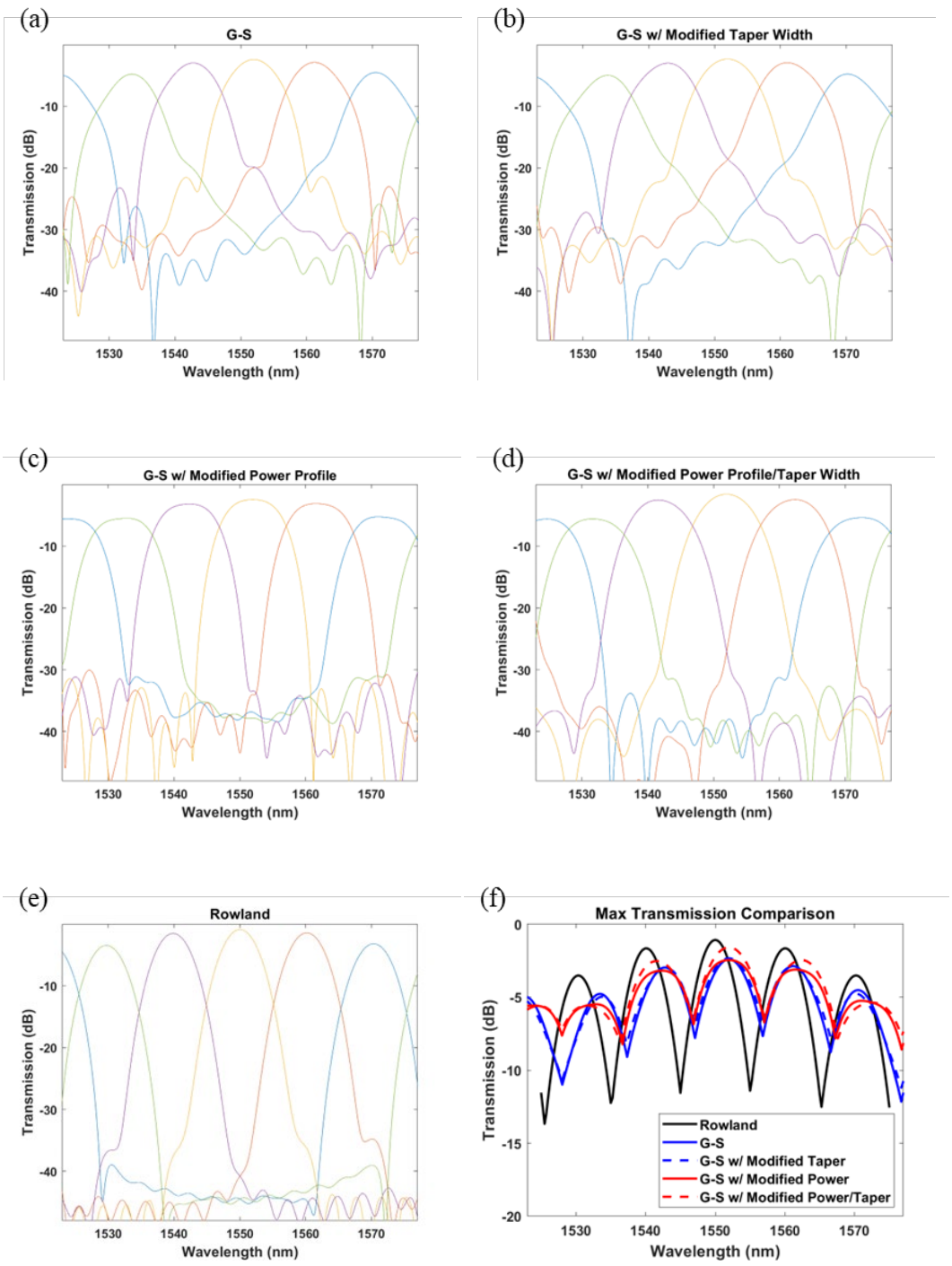

Fig. 3.11. The stimulated transmission of primary AWGs with various design; (a) G-S algorithm, (e) G-S algorithm w/ modified tapers, (c) G-S w/ modified power and (d) G-S w/ modified power and tapers, (e) Rowland and (f) the comparison of max transmission across the bandwidth

TABLE IV SUMMARY OF PERFORMANCE OF PRIMARY AWGS SIMULATED BY RSOFT

	Rowland	G-S	G-S w/ Modified Taper	G-S w/ Modified Power	G-S w/ Modified Power and Taper
Peak Transmission	-1.07 dB	-2.4 dB	-2.34 dB	-2.4 dB	-1,6 dB
Outer Channel Transmission	-3.5 dB	-4.78 dB	-4.97 dB	-5.49 dB	-5.58 dB
Crosstalk	-35 dB	-17 dB	-18 dB	-24 dB	-16 dB
Resolving Power	250 - 270	210 - 230	194 - 212	163 - 173	155 -190
3-dB bandwidth	5.6 - 6.1 nm	6.8 – 7.4 nm	7.2 – 8.0 nm	8.9 – 9.6 nm	8.1 – 10 nm
Lowest @ Max. Transmission Profile	-14.1 dB	-12.1 dB	-11.2 dB	-8.2 dB	-8.1 dB

3.3.3 The layout of Flat-top Primary Arrayed Waveguide Gratings

In the proposed design, a small primary AWG is accompanied by several larger secondary AWGs. As a result, the footprint of the small primary AWG is not a significant concern, given that its size is typically compact for a low resolving power AWG. The primary considerations involves using minimum bending radius over 1000 μm and maintaining the gap between waveguides above 6 μm threshold.

To incorporate the primary AWG design utilizing the G-S algorithm and the adjusted power profile through taper width modifications along the input aperture, the

tapers are no longer uniform in length. This variation in taper length results in different phases at the end of each taper. To address this, BeamPROP is employed to simulate the phase at the end of each taper. By comparing these phase values with those from a Rowland AWG of identical parameters but without taper modifications, the necessary additional compensation length for each arrayed waveguide can be calculated. Furthermore, it's essential to determine the phase distribution at the output aperture. This can be achieved by utilizing Eq. (2.26), which enables the calculation of the extra lengths required for the arrayed waveguides. The Rowland AWG benefits from superior phase distribution control due to its symmetrical FSRs with identical taper sizes. Any phase errors occurring within an FSR are doubled as the light travels through both FPRs. This mainly leads to a slight shift in the image position on the image surface. However, in the case of the flat-top primary AWG, where each FPR has distinct taper designs and the length variation between adjacent arrayed waveguides is not uniform, the resulting phase errors don't simply double. Instead, they become significantly complex, resulting in a convoluted phase distribution. This complexity is the reason behind the absence of simulation results for an AWG with only a modified power profile but without controlled phase information.

In designing the routing of arrayed waveguides, V-shaped structure discussed in previous chapter is adopted. The arrayed waveguide is still composed of three parts, one straight waveguide on each end connecting to input/output FPRs, and the central curve connects the two straight parts. The bending angle between adjacent arrayed waveguides is no longer a constant step since the asymmetrical taper design at input/output apertures. Therefore, the routing depends on the positions of input/output FPRs and the rotation angles and can be solved by using a MATLAB program. In most cases, the addition or

subtraction of an additional length, which could range from several dozen to a few hundred micrometers (adjusted to align with an integer multiple of the optical path of the central wavelength), must be implemented across all arrayed waveguides to determine an optimal routing solution. The configuration of the flat-top primary AWG layout intended for fabrication is depicted in Fig. 3.12, which includes close-up views of both input and output FPRs. It is important to note that there is no singular solution for the layout routing; varying the separation between input and output FPRs, as well as the rotation angles, can result in different feasible routing solutions.

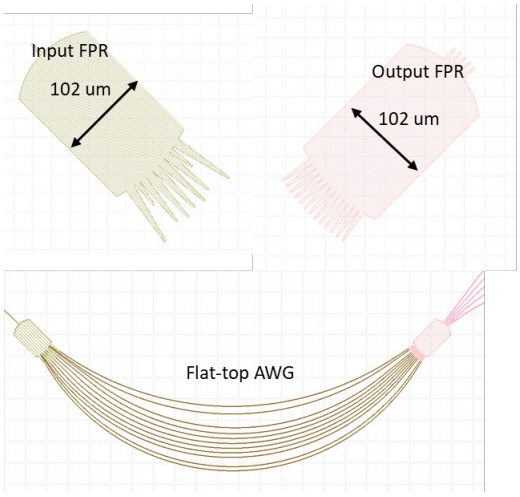

Fig. 3.12. The V-shaped layout of the flat-top primary AWG with zoom-in for input/output FPRs.

3.3.4 The Experimental Results of Flat-Top Primary Arrayed Waveguide Gratings

Both the Rowland and the flat-top primary AWGs are fabricated on 100-nm Si_3N_4/SiO_2 platform with the parameters provided in TABLE III. The power profile along the input aperture is obtained by directly measuring the optical power of each arrayed

waveguide. The measured power profile for both Rowland and flat-top AWGs is shown in Fig. 3.13 (a) and (b), respectively. In addition, the simulation result is also included in the figure for comparison.

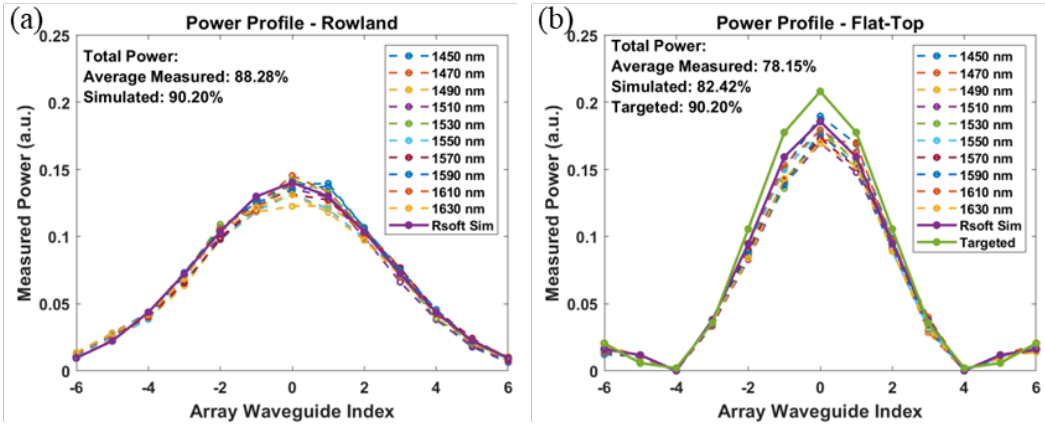

Fig. 3.13. The power profile along input aperture of (a) Rowland and (b) flat-top AWG.

In this figure, the dash lines represent the power profile obtained from different wavelengths. The solid lines are the simulation results discussed in the previous section. Theoretically, Rowland AWGs exhibit Gaussian power profiles, which can be verified through experimental results. Notably, the measured profile closely matches the simulation. The total power shown in the plot is the average value across various wavelengths, which is measured just a little less than the simulation value. Regarding the case of flat-top AWG, the measured power profile aligns closely with the simulation outcome, with lower power observed in several central arrayed waveguides. This observation implies that the wider taper has a lower coupling efficiency compared to the default taper of 6 μm. The reduced power in central arrayed waveguides leads to slight

alterations in the power profile, potentially influencing the output profile of the flat-top AWG.

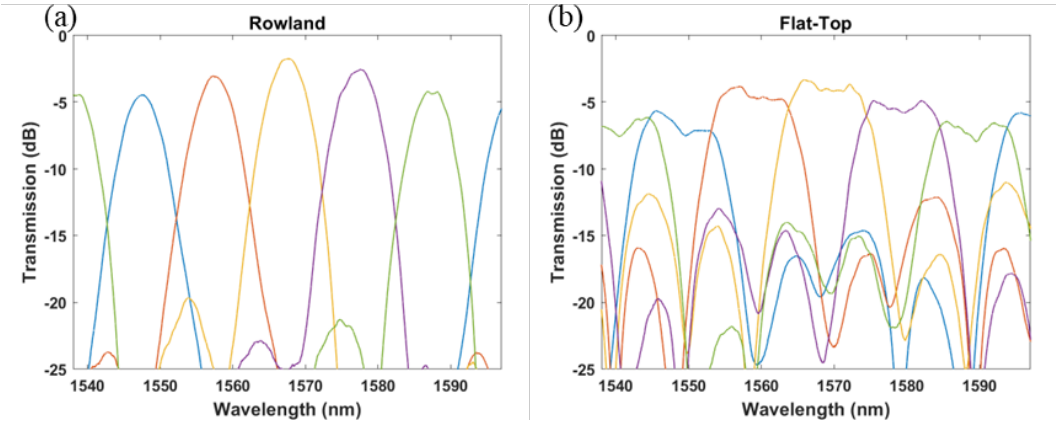

Fig. 3.14. The measured transmission spectrum of (a) Rowland and (b) flat-top AWG.

V-shaped structures are adopted for both the Rowland and the flat-top primary AWGs with default output taper (4 μm). The transmission spectrum of both Rowland and flat-top AWGs is demonstrated in Fig. 3.14 (a) and (b), respectively. The peak transmission of Rowland primary AWG is measured to be -1.77 dB, around half a dB lower than simulation. Outer channels are 2.5 dB lower than center channels. Crosstalk is only -20 dB lower, while in simulation, it is about -40 dB lower, indicating the phase error is a lot larger. The lowest transmission at channel cross-points is -18 dB. On the other hand, flat-top AWG demonstrates a lower peak transmission, about 1.5 dB lower than the Rowland counterpart. The same situation occurs for outer channels as well, and they are 2.5 to 3 dB lower than the central channels. However, the lowest transmission at channel cross-point can be greatly improved to -7.9 dB, which is more than 10 dB better as compared to the Rowland AWG. The 3-dB bandwidth is 11 to 12 nm for the flat-top AWG, and it is more than 6 nm

broader. The crosstalk of the flat-top AWG is only -7 dB down for some wavelength, meaning that the phase control needs to be better because the side lobes are evident. Overall, a flattened response is realized experimentally.

The maximum transmission profile is provided in Fig. 3.15, which offers a clear view of peak transmission and lowest transmission at channel cross-points. The flat-top AWG improves significantly at channel cross-points by sacrificing only around 1.5 dB at peak transmission.

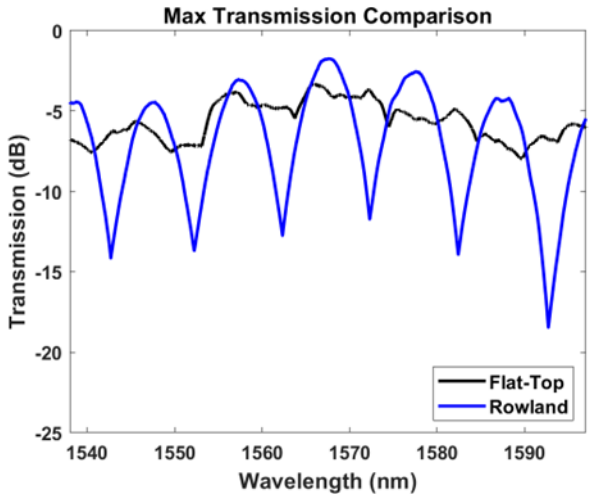

Fig. 3.15. The maximum transmission profile of both Rowland and flat-top AWG

3.3.5 Design and Simulation of Three-Stigmatic-Point Secondary Arrayed Waveguide Gratings

The secondary AWG is designed to be a higher resolving power AWG with larger footprint. In order to apply cross dispersion optics at the output image surface of secondary AWG, a flat image surface is required. The design rule of TSP AWG has been discussed

in Chapter 2, so there will be no in-depth discussion about the design procedure. Instead, in this section, only quick reviews will be provided.

In designing secondary TSP AWG, the same procedure has been conducted and the design parameters are listed in Table III. Only one design parameter is changed as that the separation of arrayed waveguide is enlarged from 6 to 9 μm, which will be discussed in the coming section. First, the geometry of input/output FPRs are calculated by our MATLAB program and the original Rowland FPRs are replaced by the calculated geometry. Next, the power and phase information at the input aperture are obtained by running the BeamPROP in Rsoft. After replacing the original output FPR with the new geometry, the extra lengths of arrayed waveguides are calculated to compensate the geometry difference of FPRs and the phase error between the calculation from aberration theory and the simulation from Rsoft. At last, a launch field, including the power profile and phase information, is ready for final simulation by running our MATLAB script to execute BeamPROP tool to get the output transmission spectrum. For comparison purposes, a Rowland AWG counterpart with the same design parameters described in Table III, are created and simulated in Rsoft as well. Fig. 3.16 shows the simulated transmission spectrum of the Rowland and the TSP AWG (a and c) and their calculated resolving power (b and d).

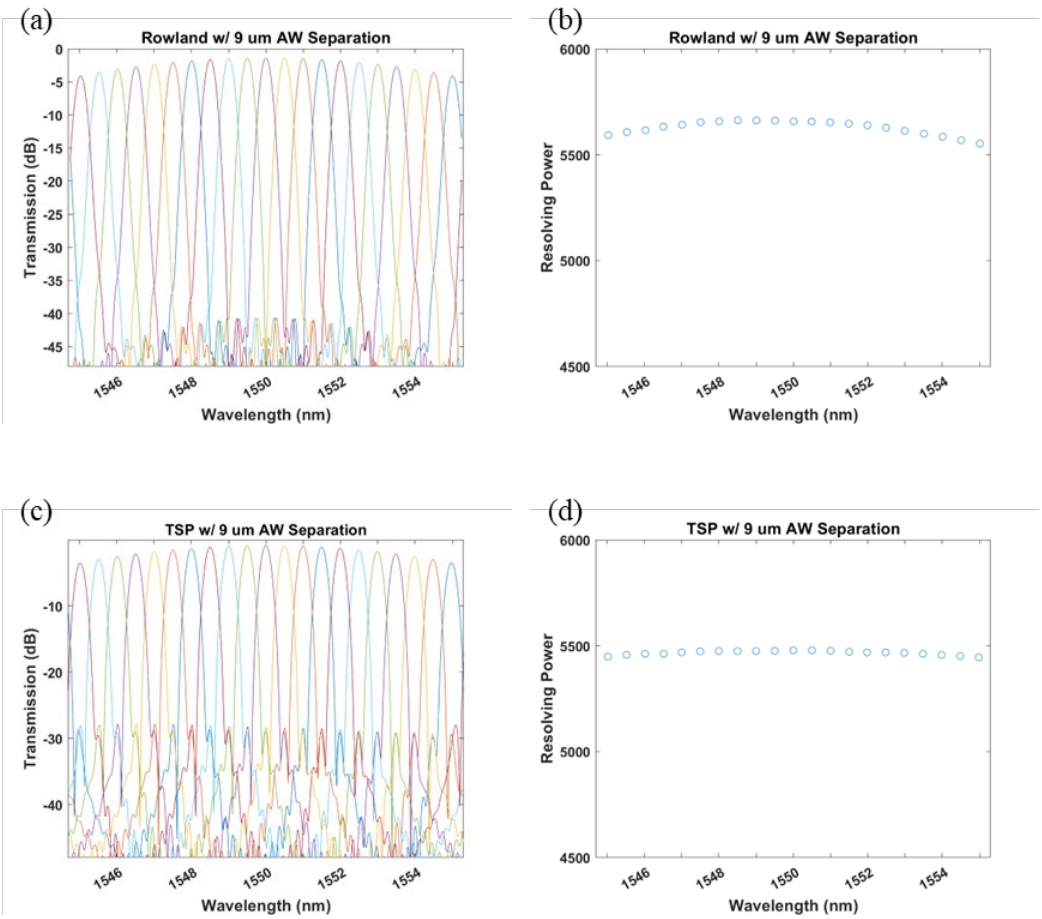

Fig. 3.16. The simulated transmission spectrum of (a) Rowland AWG and (b) its corresponding resolving power; the TSP AWG counterpart in (c) and (d).

The peak transmission of Rowland AWG is -1.4 dB and is lowered to -4.1 dB for outer channels. The crosstalk is about -40 dB and the resolving power is above 5,500 across the bandwidth with the largest resolving power of 5,660. The transmission of TSP AWG is slightly higher with the peak transmission near -0.9 dB and the transmission at outer channels is -3.9 dB. The crosstalk is worse than the Rowland counterpart, and only around -28 dB can be observed. The resolving power is slightly lower than Rowland across the bandwidth. The largest resolving power is around 5,500.

3.3.6 The Layout of Three-Stigmatic-Point Secondary Arrayed Waveguide Gratings

There are five secondary AWGs with flat image surface in the proposed design. In terms of layout structure, V-shaped and crossover structure has been introduced. However, with either of the previous two layout structures, arranging the five output FPRs in close proximity on the same image surface proves to be a challenge. Aligning all five output FPRs side by side and on the same image surface is highly desirable since it simplifies the cross-dispersion setup alignment. To address this, an alternative layout structure known as the "Top-Hat" configuration is introduced. The top-hat AWG design involves positioning the input/output FPRs in close alignment, and the routing of the arrayed waveguides resembles the shape of a top hat.

While the closely aligned FPRs in the top-hat configuration offer the advantage of easier cross-dispersion setup, there are some trade-offs to consider. The routing distance of the arrayed waveguides increases significantly due to the requirement of maintaining a minimum gap of 7 μm between each arrayed waveguide to prevent mutual coupling. Given that the arrayed waveguide width is 2 μm, the separation between arrayed waveguides (center to center) is set to 9 μm for simulation purposes. Moreover, it's important to note that the top-hat structure comes with a larger footprint as the arrayed waveguides need to be significantly extended. This larger footprint could pose challenges during fabrication, making it more complex to produce such a large device. The top-hat layout is displayed in Fig. 3.17.

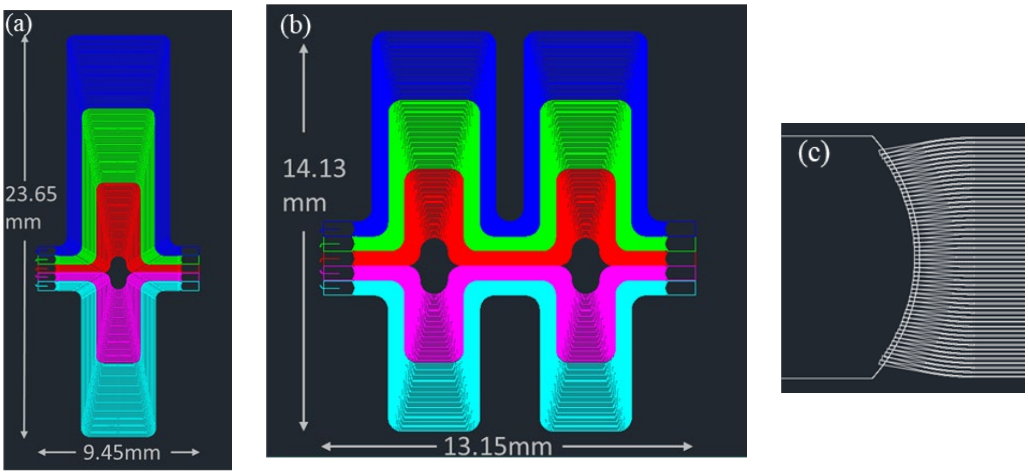

Fig. 3.17. (a)The one top-hat layout schematic, (b) two top hat layout and (c) zoom-in view of an input/output aperture.

Fig. 3.17 (a) shows one top-hat structure where one color represents one TSP AWG. In this particular design, the light is guided through a single top-hat-shaped arrayed waveguide path before reaching the output FPR. This configuration offers several notable advantages. Firstly, it enables the closely aligned positioning of the output FPRs on the same image surface. Additionally, a significant benefit lies in the fact that all arrayed waveguides possess the same number of bends, minimizing the potential for phase errors to accumulate. The only variation in bending occurs near the input/output apertures, as depicted in Fig. 3.17 (c). To connect the tapers at input/output aperture and the arrayed waveguide, a bend is adopted where each bend has a different bending radius. Except for these two bends, every arrayed waveguide consists of the same four 90^{o} bends. However, it's important to highlight that due to accommodating all five TSP AWGs, the length of the arrayed waveguide can become exceptionally long in comparison to the original TSP AWG or Rowland AWG designs. In fact, the longest arrayed waveguide in this layout extends to approximately 28 mm, whereas the longest arrayed waveguide in a V-shaped AWG with

similar parameters is a mere 14 mm. This elongated design leads to a large rectangular footprint, which, in turn, could potentially lead to non-uniformity issues during the fabrication process, particularly in situations involving e-beam resist spinning.

To overcome the large rectangular footprint, a two-top-hat structure is developed. This approach aims to achieve a more square-like overall layout, thereby mitigating the challenges posed by the elongated footprint of the one-top-hat design. For a two-top-hat TSP AWG, each arrayed waveguide is designed to have a routing composed of eight 90^{o} bends and other connecting straight waveguides. Although the length of the longer side is reduced by 40% when compared to the one-top-hat design, the total length of the arrayed waveguide increases. This is due to the necessity of traversing through two distinct "hats" in the routing path. Consequently, the longest arrayed waveguide in this two-top-hat design reaches a substantial 36 mm in length, which is almost three times the length of an ordinary Rowland AWG.

3.3.7 The Experimental results of Secondary Arrayed Waveguide Gratings

The one-top-hat structure of TSP AWG is fabricated to evaluate the performance and a Rowland counterpart with V-shaped structure is also fabricated for comparison. The measured transmission spectrum for both AWGs is illustrated in Fig. 3.18. (a) and (c) while the resolving power is in (b) and (d).

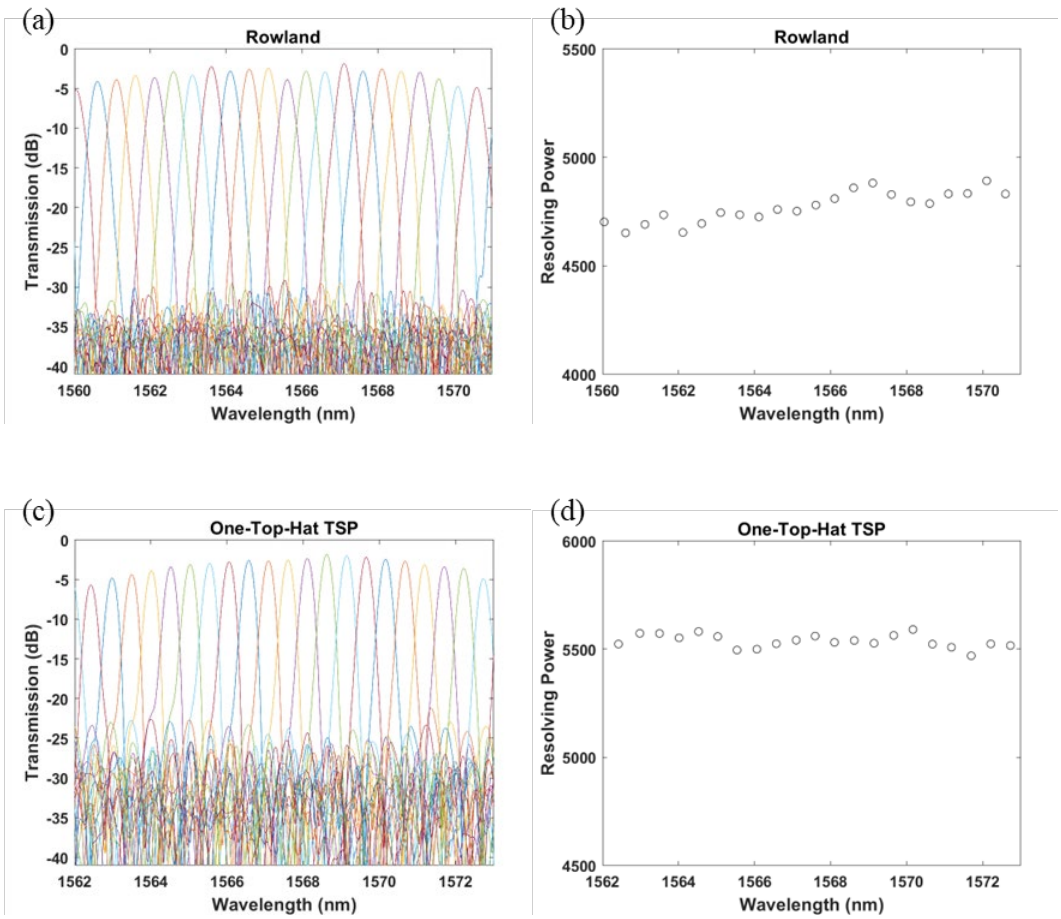

Fig. 3.18. The measured transmission spectrum of (a) V-shaped Rowland AWG and (b) its corresponding resolving power; the one-top-hat TSP AWG counterpart in (c) and (d).

The peak transmission of Rowland AWG is measured to be -1.84 dB. However, it seems there is defect at central channel, causing a lower transmission. So, the peak transmission is expected to be higher. The transmission at outer channels is about 3.0 dB lower. The crosstalk is at least -25 dB. But the resolving power is lower than expected. It can reach over 5,500 in simulation but for this device, the largest resolving power is only near 4,900. As for one-top-hat TSP AWG, the peak transmission is -1.81 dB, and it reduced by 3 to 4 dB for outer channels. The crosstalk is worse than the Rowland counterpart since

the length of arrayed waveguide of one-top-hat AWG is significantly longer than that of Rowland AWG. The resolving power of one-top-hat AWG is very good, with the largest being near 5,600 and above 5,470 across the whole band. The results confirm that top-hat design is achievable and can be used in a cascade AWG design.

3.3.8 The Experimental results of Cascaded Arrayed Waveguide Gratings

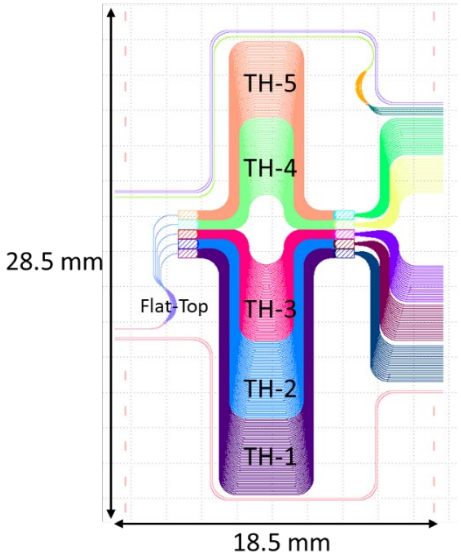

Fig. 3.19. The layout of fabricated cascaded AWG, consisting of one flat-top primary AWG (labeled as Flat-Top) and five one-top-hat TSP secondary AWGs (labeled as TH-1 to TH-5).

The fabricated cascaded AWG devices fabricated comprises one flat-top primary AWG, connected by five one-top-hat TSP secondary AWGs. The complete layout is displayed in Fig. 3.19, and the corresponding chip size is provided. For comparison, a cascaded AWG featuring Rowland as the secondary AWG has also been fabricated. However, owing to the constraints imposed by chip size, both of these cascaded AWGs

cannot be accommodated within a single chip. Consequently, two distinct chips have been employed to house the individual cascaded AWGs. In addition, multiple input channels are added to secondary AWGs. The strategic addition serves to provide flexibility in the experimentation process. Specifically, one of the input channels can be directly used to introduce the light source, while the remaining input channels can be linked to the primary AWG.

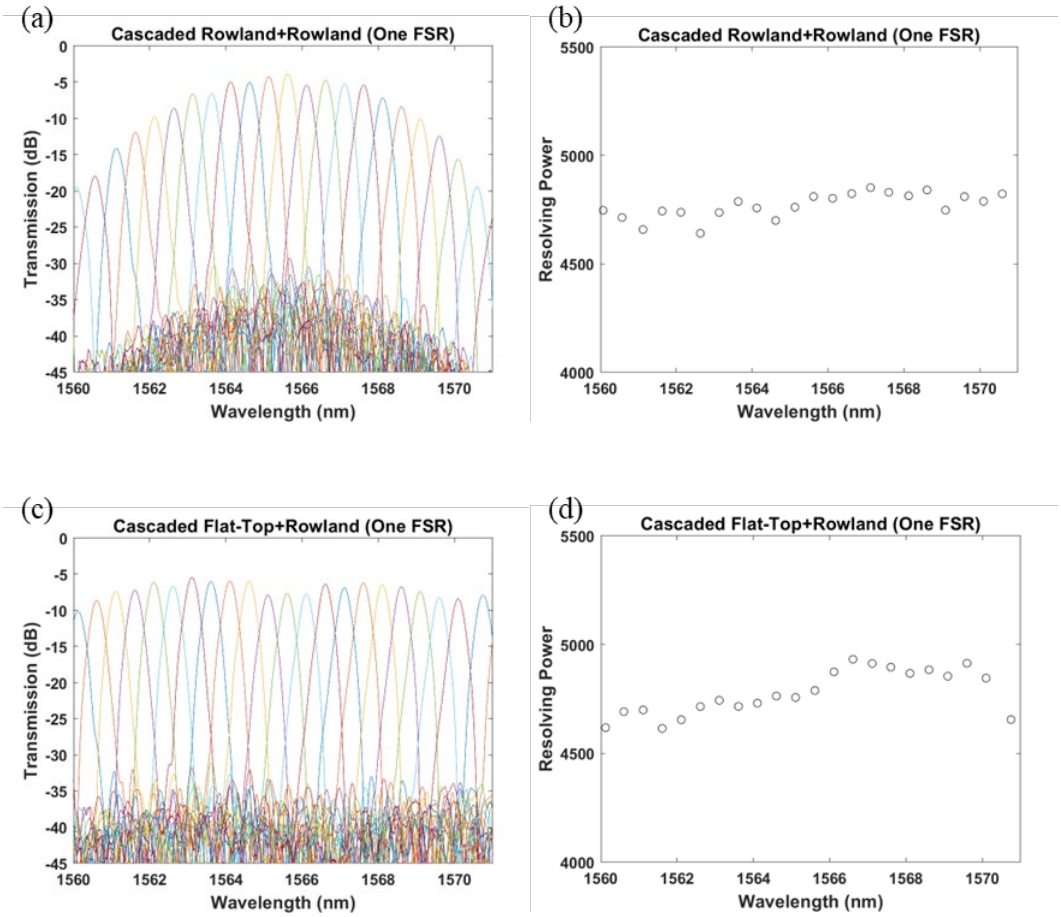

Fig. 3.20. The measured transmission spectrum of (a) Rowland+Rowland AWG and (b) its corresponding resolving power; the flat-top+Rowland AWG counterpart in (c) and (d).

Fig. 3.20 shows the measured transmission spectrum and corresponding resolving power of a cascaded AWG with Rowland structure as secondary stage. Two different structures of primary AWGs are connected to the Rowland secondary AWG via different input channels. One primary AWG is the Rowland structure and the other is the flat-top AWG. The design parameters of these AWGs are the same parameters listed in Table III. Fig. 3.20 (a) and (b) represent measured transmission spectrum and resolving power of Rowland+Rowland cascaded AWG. And those of the flat-top+Rowland cascaded AWG are displayed in (c) and (d).

The cascaded AWG utilizing the Rowland+Rowland configuration exhibits a notably diminished transmission at the channel cross-points, registering around -20 dB. In contrast, the peak transmission for the central channels is substantially higher, reaching approximately -3.8 dB. The resolving power of this configuration falls below 5,000. Even though the peak transmission remains pretty good, the low throughput at outer channels renders it unsuitable for applications in astronomical observations. On the other hand, the flat-top+Rowland AWG configuration displays a more desirable response across the entire bandwidth. Despite a slightly reduced peak transmission of -5.47 dB, which is 1.6 dB lower than the Rowland+Rowland counterpart, the outer channels' performance is improved with a transmission level of -8.5 dB. This remarkable enhancement of 14 dB in certain outer channels is achieved without compromising the performance of the central channels to a significant extent. The uniform response across the spectrum renders this configuration far more appealing and practical for astronomical applications. The resolving power of the

flat-top+Rowland cascaded AWG configuration falls within the range of 4,600 to 4,900, demonstrating a satisfactory performance metric.

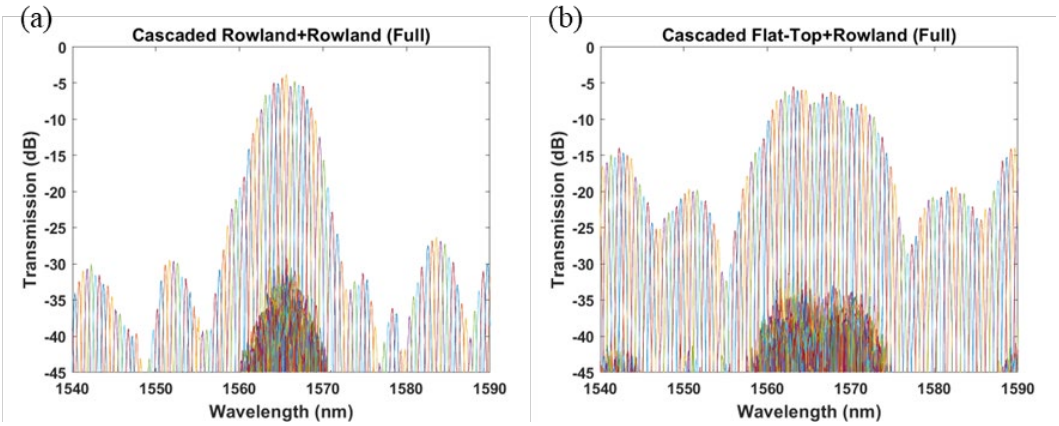

Fig. 3.21. The measured transmission spectrum of cascaded AWG across the bandwidth of 50 nm. (a) represent Rowland+Rowland AWG and (b) is flat-top+Rowland AWG.

The transmission spectrum across the bandwidth of 50 nm, the FSR of the primary AWG, is plotted in Fig. 3.21, where (a) represents the Rowland+Rowland configuration and (b) is the flat-top+Rowland configuration. The distinction between the Rowland+Rowland and flat-top+Rowland cascaded AWG configurations is quite evident. The Rowland+Rowland cascaded AWG has higher peak transmission, but it drops significantly at the outer channels. Because the side lobes of the Rowland primary AWG are much lower compared to that of the flat-top primary AWG, Rowland primary AWG demonstrates superior ability to filter out extraneous signals beyond the passband of the channels connected to the secondary AWG. As a result, the Rowland+Rowland AWG is capable of generating a cleaner spectrum, characterized by a noise level ranging between -25 and -30 dB. As for flat-top+Rowland cascaded AWG, the flat-top+Rowland cascaded

AWG configuration demonstrates a flattened response within the designated passband. However, its capacity to filter out undesired signals is somewhat restricted due to the evident side lobes present in the flat-top primary AWG. This results in a higher noise level, exceeding -15 dB for certain wavelengths. This discrepancy is only 9-10 dB lower than the signals within the designated passband. Upon comparing the noise profile with the side lobes of the central channel in Fig. 3.14 (b), a resemblance in profiles becomes apparent. This correlation substantiates that the increased noise level can be attributed to the side lobes originating from the flat-top primary AWG. To mitigate the side lobes of the flat-top primary AWG, a more comprehensive investigation is necessary. Enhanced understanding of the phase information along the arrayed waveguides will enable more accurate compensation for phase errors. Consequently, refining this compensation process has the potential to reduce the side lobe issues associated with the flat-top+Rowland cascaded AWG configuration.

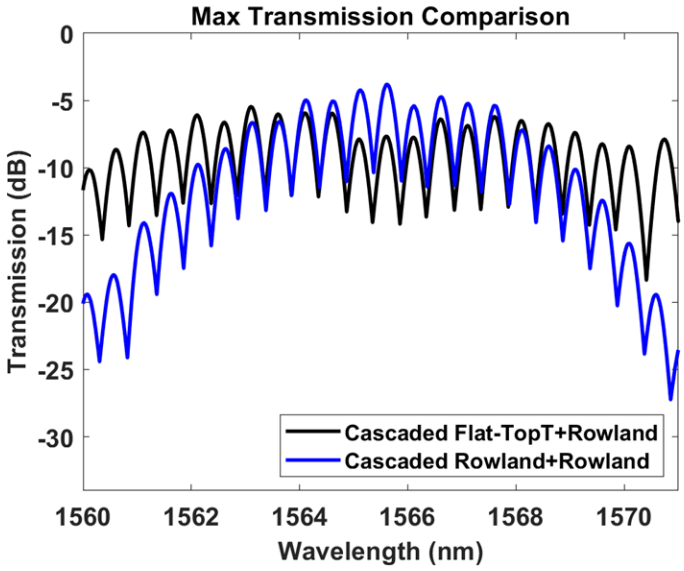

Fig. 3.22. The comparison in transmission within the passband between both cascaded AWGs with Rowland configuration as secondary AWG

Comparing the maximum transmission profile within the passband between two cascaded AWG, as displayed in Fig. 3.22, the flat-top+Rowland configuration exhibits a flattened response across the passband despite slightly lower peak transmission. In contrast, the Rowland+Rowland configuration suffers significant loss at outer channels. The discrepancy can easily exceed 12 dB at some outer channels, indicating that the flat-top primary AWG is more suitable in the application to astrophotonics.

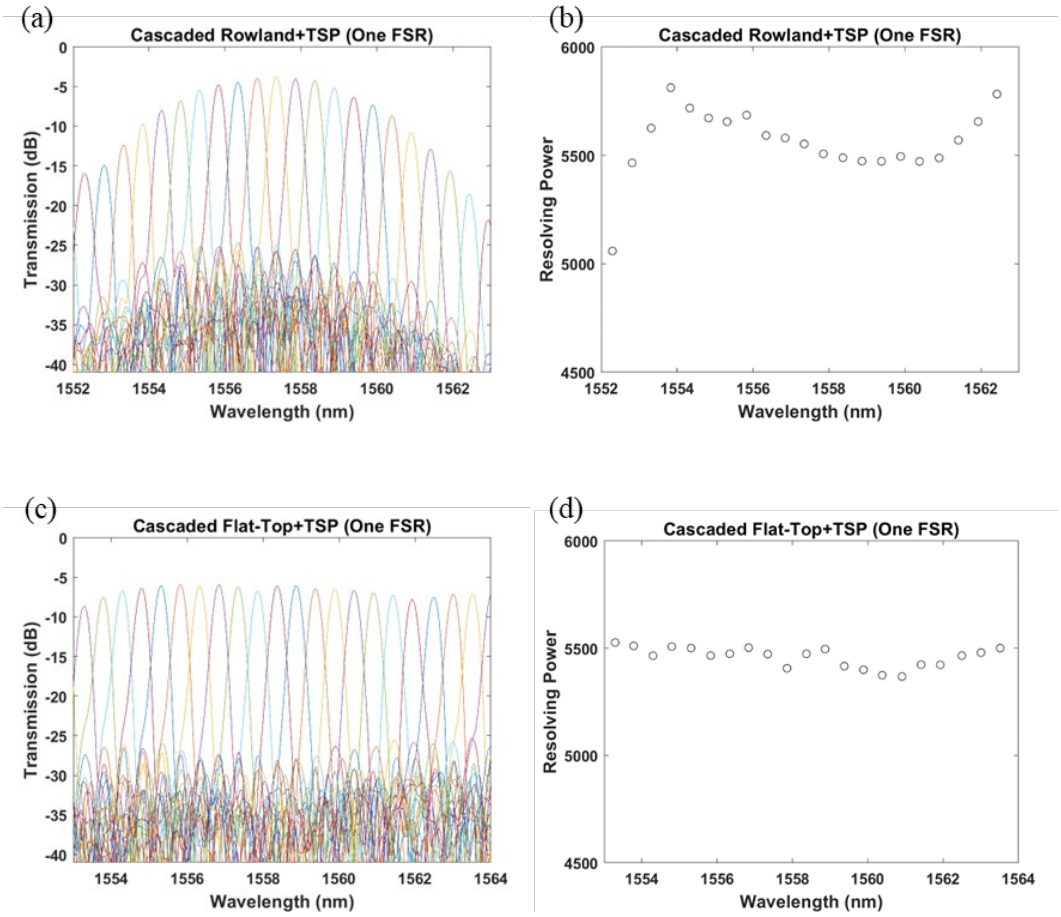

Fig. 3.23. The measured transmission spectrum of (a) Rowland+one-top-hat TSP AWG and (b) its corresponding resolving power; the flat-top+one-top-hat TSP AWG counterpart in (c) and (d).

Proceeding with the examination of alternative devices, the Rowland secondary AWG has been substituted with a one-top-hat structure. The measured transmission spectra are illustrated in Fig. 3.23. In (a), the primary AWG remains a Rowland structure, while in (b), the primary AWG adopts a flat-top design.

The measured transmission spectrum of the two cascaded AWG share the same trend or behavior as the previous set of cascaded AWG. Rowland+one-top-hat TSP AWG shows higher peak transmission of -3.7 dB which is 2 dB higher than the flat-top+one-top-hat counterpart. Again, at outer channels, flat-top+one-top-hat AWG has the huge advantage of over 12 dB. Regarding resolving power, both cascaded AWG features around 5,000 to 5,500. Flat-top+one-top-hat AWG performs more consistent, showing similar resolving power across the bandwidth. The crosstalk for the cascaded AWG can reach over 20 dB down.

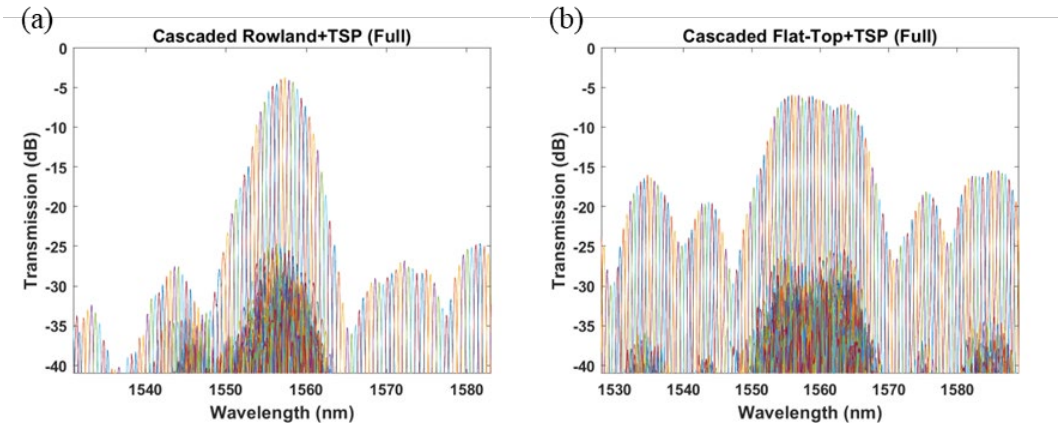

Fig. 3.24. The measured transmission spectrum of cascaded AWG across the bandwidth of 50 nm. (a) represent Rowland+one-top-hat AWG and (b) is flat-top+one-top-hat AWG.

The measured transmission spectrum across the bandwidth of 50 nm, is demonstrated in Fig. 3.24, where (a) represents the Rowland+one-top-hat cascaded AWG and (b) is the flat-top+one-top-hat cascaded AWG. Similarly, when analyzing the cascaded AWGs with Rowland as the primary stage, a trend emerges wherein higher peak transmission is achieved but with a much narrower bandwidth. The effectiveness in filtering out unwanted signals is still remarkable, with unwanted noise being at least 20 dB lower. In contrast, the cascaded AWG featuring a flat-top primary stage displays a broader passband and a more flattened response. However, it also exhibits a higher noise level, with only around a 9-10 dB difference from the main signals. This measurement serves as additional evidence that the flat-top primary AWG has advantageous features such as a flattened response, yet it is susceptible to larger side lobes in the presence of larger phase errors. Comparing the maximum transmission profile within the passband between two cascaded AWG, the flat-top+one-top-hat configuration exhibits a flattened response across the passband despite the lower peak transmission. In contrast, the Rowland+one-top-hat configuration suffers significant loss at outer channels, leading to narrower bandwidth. The difference in transmission can easily exceed 12 dB at some outer channels. The transmission comparison is plotted in Fig. 3.25.

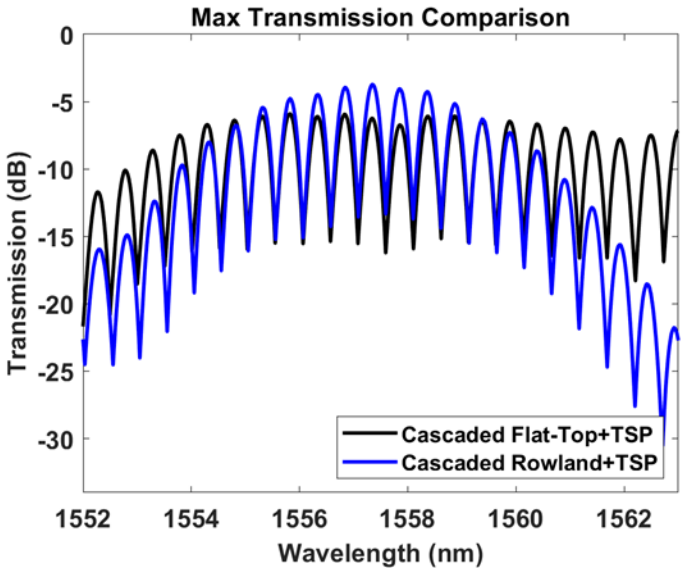

Fig. 3.25. The comparison in transmission within the passband between both cascaded AWGs with one-top-hat configuration as secondary AWG

Consequently, a cascaded AWG configuration has been successfully fabricated and tested, as shown in Fig. 3.19, featuring a flat-top primary stage coupled with five distinct one-top-hat secondary stages. These secondary AWGs, denoted as top-hat-1, to top-hat-5, incorporate varying lengths of arrayed waveguides, enabling a valuable comparison to gauge the impact of extended arrayed waveguide lengths on cascaded AWG performance. The output transmission spectra and the resolving power of the cascaded AWG is demonstrated in Fig. 3.26, where (a), (c), (e), (g), and (i) represent the transmission spectrum measured from the flat-top+top-hat-1 to flat-top+top-hat-5, and the corresponding resolving power of each case is provided in (b), (d), (f), (h), and (j). Across all five configurations, the cascaded AWGs exhibit peak transmission levels ranging from -5 to -8 dB, with a subsequent 2 to 3 dB reduction observed for outer channels. The cascaded flat-top+top-hat-3 and flat-top+top-hat-4 possess the highest transmission while the flat-top+top-hat-1 and flat-top+top-hat-5 showcase the lowest transmission. This

decreasing transmission can be attributed to the combination of the lower transmission level of the flat-top primary stage at outer channels and the increasing lengths of arrayed waveguides routings for the top-hat secondary stage. Notably, all five cascaded AWGs exhibit a flattened response profile, and a relatively consistent transmission level is still maintained for outer channels. A noteworthy distinction between the five configurations is the crosstalk levels. As the length of arrayed waveguide increases, a progressively more pronounced crosstalk phenomenon is observed. In this fabricated device, the top-hat-3 and top-hat-4 secondary AWGs are located at the center of the whole cascaded AWG and therefore possess the shorter routing length of arrayed waveguides. This advantageous placement contributes to a notably low crosstalk level, exhibiting a reduction of at least 18 to 20 dB for both the flat-top+top-hat-3 and flat-top+top-hat-4 cases. As we move to configurations such as flat-top+top-hat-2 and flat-top+top-hat-5, where the alignment of output FPRs necessitates longer routing paths for the arrayed waveguides, the crosstalk slightly increases to approximately 12 to 17 dB. The most pronounced crosstalk, with a modest margin of only 6 to 8 dB, is observed in the flat-top+top-hat-1 AWG configuration, characterized by the longest routing lengths for the arrayed waveguides. This phenomenon indicates the potential enlargement of phase errors with the propagation of light over longer distances, which can subsequently lead to increased crosstalk.

The resolving power across all five configurations exhibits a notable similarity, showing around 5,500. However, slightly higher resolving power for the flat-top+top-hat-1 and lower resolving power for the flat-top+top-hat-4 can be observed. The resolving power is determined by the secondary AWGs and the subtle variation in these values is presumed to stem from potential fabrication-related factors.

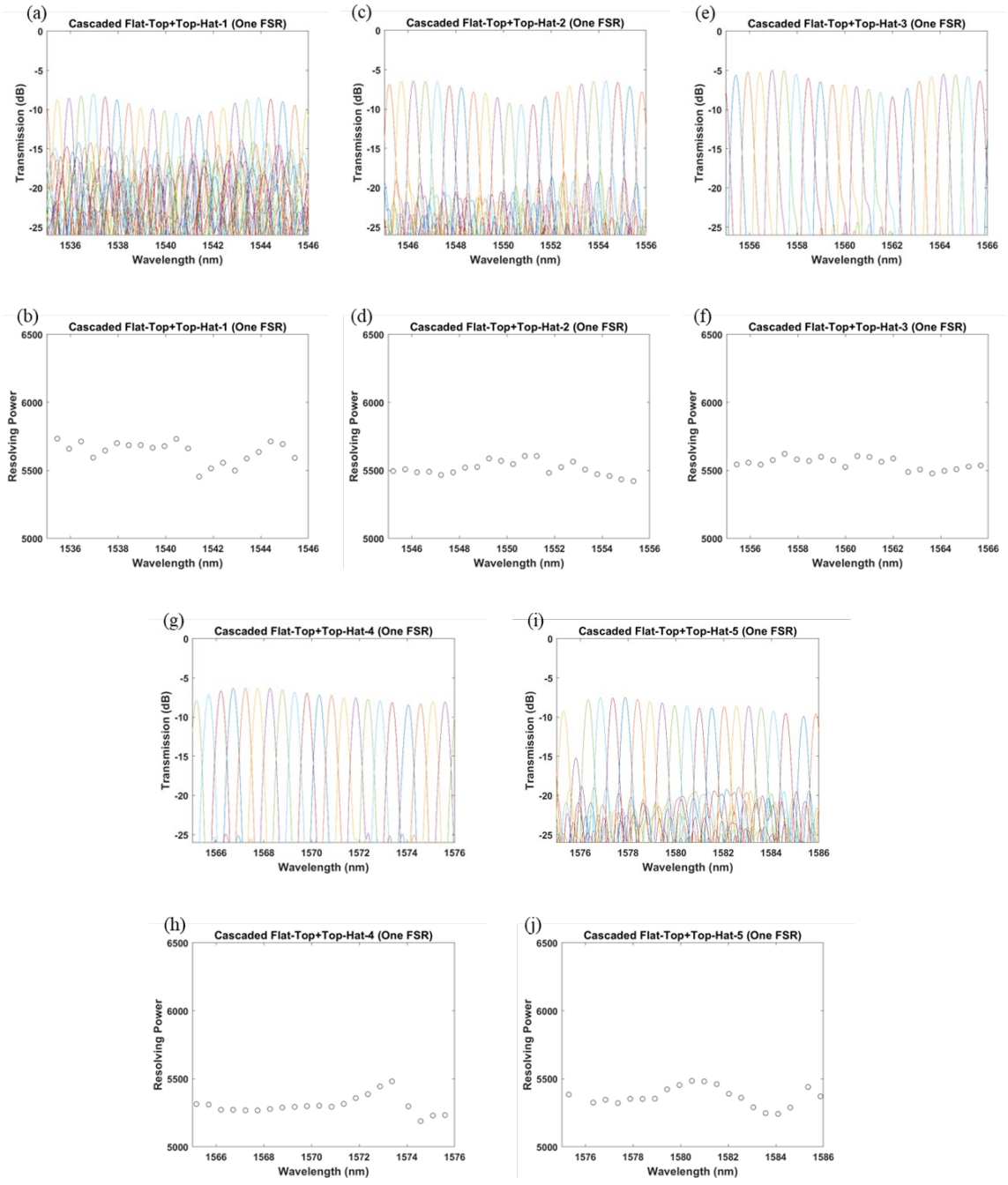

Fig. 3.26. The measured transmission spectrum of a set of flat-top+one-top-hat cascaded AWGs. (a), (c), (e), (g), and (i) correspond to the flat-top+one-top-hat-1 to flat-top+one-top-hat-5. The resolving power is also displayed in (b), (d), (f), (h), and (i).

The maximum transmission comparison across one FSR of the flat-top primary AWG is displayed in Fig. 3.27. A flattened response across all five configurations can be

observed, yielding a uniform output transmission level over a broad bandwidth. This outcome is pivotal as it lays the groundwork for the exploration of higher resolving power AWGs. Consequently, the cascaded AWG configuration holds promise for meeting the requirements of astronomical instrumentation demanding high resolving power over a wide bandwidth.

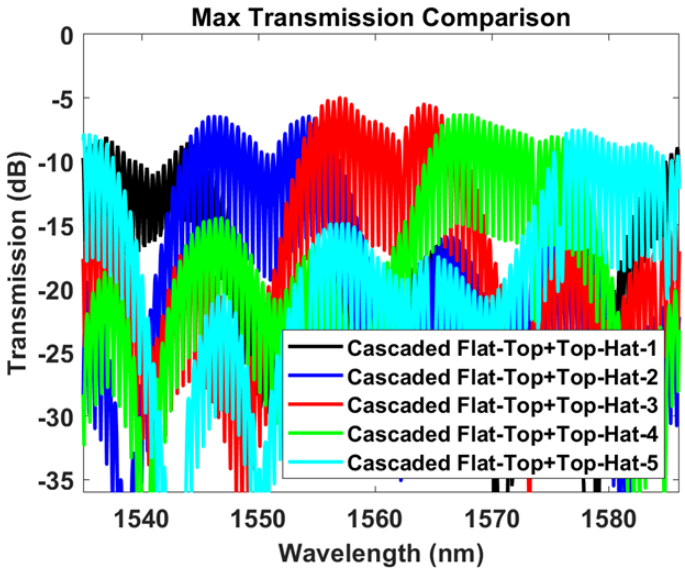

Fig. 3.27. The maximum transmission across one FSR of flat-top primary AWG.

3.4 Summary

In this chapter, the concept of cascaded AWGs is introduced as a solution to address the challenges associated with simultaneously achieving high resolving power and a broad FSR in integrated photonic devices. The proposed design employs a compact primary AWG with a wide FSR, complemented by several larger secondary AWGs to fulfill the necessary resolution criteria.

A key consideration in the design of these cascaded AWGs revolves around achieving a flat response within the primary stage. This becomes crucial to prevent substantial losses both at the outer channels and the channel cross-points. The interplay between the primary and secondary AWGs requires precise control over the power distribution and phase behavior of the optical signal. Flat-top primary AWG has been discussed comprehensively, covering from the Gerchberg-Saxton algorithm to the simulation, layout design and experimental results. The core design philosophy of the flat-top primary AWG centers around two critical modifications: adjusting the power profile at the input aperture and manipulating the phase distribution at the output aperture. Through these adjustments, the primary AWG transforms the input signal into a sinc function, which in turn results in a square function at the output image surface. The power profile is modified by using tapers with various widths and the phase distribution is calculated by the Gerchberg-Saxton Algorithm.

The V-shaped structure is adopted when designing flat-top primary AWG. Due to the altered geometry of tapers along the input aperture, the geometry of input/output FPR is no longer the same, leading to additional phase difference to be compensated.

TSP AWG is employed as secondary AWG to enhance the cross-dispersion optics setup. In addition, the preference is for all the output FPRs of secondary AWGs to be positioned closely and aligned on the same image surface. To achieve this, the design incorporates the use of top-hat layout configurations.

Fabricated and characterized cascaded AWGs employing different combinations of Rowland, flat-top, and top-hat AWGs have provided valuable insights. Experimental results showcase that while the Rowland primary AWG exhibits higher peak transmission,

it also exhibits significant losses at channel cross-points. Conversely, the flat-top primary AWG displays slightly lower peak transmission but substantially improves losses at channel cross-points by over 12 dB in experimental observations. However, the presence of phase errors generates noticeable side lobes, thereby degrading crosstalk performance. The cascaded AWG with a flat-top primary stage demonstrates a flat output profile within the passband yet struggles in effectively filtering out unwanted signals beyond the passband. In contrast, the Rowland primary AWG excels in terms of signal filtering, showcasing a noise level that is experimentally at least 20 dB lower. Further explorations are required to comprehensively address phase errors in flat-top AWGs and enhance compensation strategies.

Chapter 4 Perovskite Solar Cell

4.1 Introduction of Perovskite Material and its Photovoltaic Application

Various chemicals will be discussed in the following chapters. The table below provides the name, chemical formula, and abbreviation for some chemicals to prevent some possible misleading abbreviation.

TABLE V MATERIAL INFORMATION

Name	Chemical Formula	Abbreviation
2,3,5,6-Tetrafluoro-7,7,8,8-tetracyanoquinodimethane	$C_{12}F_4N_4$	F4-TCNQ
4,4',4"-Tris[(3-methylphenyl)phenylamino]triphenylamine	$C_{57}H_{48}N_4$	m-MTDATA
[5,6]-Fullerene-C_{60}	C_{60}	
[6,6]-Phenyl-C61-butyric acid methyl ester	$C_{72}H_{14}O_2$	PCBM
Ammonia	NH_4OH	
Bathocuproine	$C_{26}H_{20}N_2$	BCP
Calcium titanium oxide	$CaTiO_3$	
Copper indium gallium selenide	$CuIn_xGa_{(1-x)}Se_2$	CIGS
Copper indium selenide	$CuInSe_2$	CIS
Dimethyl sulfoxide	C_2H_6OS	DMSO
Formamidinium	$HC(NH_2)_2^+$	FA^+
Methylammonium	$CH_3NH_3^+$	MA^+

N,N-Dimethylformamide	C_3H_7NO	DMF
Poly(3,4-ethylenedioxythiophene) polystyrene sulfonate	$(C_8H_8O_3S)_n$:$(C_6H_6O_2S)_n$	PEDOT:PSS
Poly[bis(4-phenyl)(2,4,6-trimethylphenyl)amine	$(C_{21}H_{19}N)_n$	PTAA
poly[N,N'-bis(4-butylphenyl)-N,N'-bis(phenyl)benzidine]	$(C_{22}H_{21}N)_n$	poly-TPD
Tetramethylammonium	$((CH_3)_4N)^+$	TEA^+
Thiourea	NH_2CSNH_2	

4.1.1 Perovskite Materials Used in Solar Cell

Organometal halide perovskites have captivated researchers in recent years due to their enticing material properties that hold potential for high-efficiency photovoltaic devices at a low fabrication cost. In the solar cell technology landscape, perovskite photovoltaic devices have demonstrated remarkable progress in power conversion efficiency (PCE) over the last decade. Notably, the PCE of perovskite-based solar cells has witnessed a substantial rise from an initial 3.8% in 2009 [35] to an impressive 26.1% by 2023 [36].

The name "Perovskite" is a tribute to the Russian mineralogist Lev A. Perovski. A perovskite material possesses a structure similar to that of calcium titanium oxide ($CaTiO_3$), represented as ABX_3 [37], as depicted in Fig. 4.1 (a). In the context of photovoltaic applications, A site accommodates a polyatomic organic cation, usually methylammonium ($CH_3NH_3^+$ or MA^+), formamidinium ($HC(NH_2)_2^+$ or FA^+) [38], or tetramethylammonium ($((CH_3)_4N)^+$ or TEA^+) as well as cesium (Cs^+) and rubidium (Rb^+). Among these, methylammonium (MA^+) prevails in perovskite solar cells. A larger or smaller A cation can cause the whole lattice to expand or contract. Formamidinium (FA^+) boasts a slightly larger effective ionic radius than methylammonium (MA^+), resulting in a slightly expanded lattice constant, a correspondingly reduced bandgap, and consequently, a red shift in the absorption onset. Tetramethylammonium ($((CH_3)_4N)^+$ or TEA^+) exhibits an even larger effective ionic radius, further reducing the bandgap and shifting the absorption onset to longer wavelengths. The B site is occupied by a metal cation, such as lead (Pb), tin (Sn), or germanium (Ge). Among these, lead-based perovskite solar cells

exhibit the highest PCE. However, lead is one of the most toxic elements, raising concerns about health risks from lead exposure. The X site represents an anion, usually a halogen like chlorine, bromine, or iodine, or sometimes a combination thereof. The optical bandgap of a perovskite material, which incorporates more than one cation or halide, can be finely adjusted. This enables precise tuning of optical absorption to span the entire visible spectrum [39]. Noh et al. and Eperon et al. have demonstrated the tunability of perovskite bandgap through varying I^- and Br^- composition ratios with methylammonium based and formamidinium based active materials, respectively. [40-41]. Ge-based perovskites exhibit the smallest bandgap, followed by Sn-based perovskites, and Pb-based perovskites possess the largest bandgap due to the increasing radius from Ge to Pb [42]. It has been observed that $CH_3NH_3PbI_3$ ($MAPbI_3$) goes through a phase transition from orthorhombic to tetragonal at around 140 to 161.4K and from tetragonal to cubic at around 295 to 338K [43-46], which is shown in Fig. 4.1(b). Structural phase transitions play a pivotal role in altering the lattice constant, which in turn leads to bandgap variations. Besides, in summer, a device can easily surpass this temperature and the corresponding impact on the electrical or optical properties needs to be addressed.

Methylammonium (MA) lead halide is still the dominant active layer being used today in most perovskite solar cell research since the active layer has remarkable properties, such as high absorption coefficients, long carrier diffusion length, large carrier mobility, tunable optimal bandgap with tunability and low-temperature solution process with potential application to flexible solar cell [40, 47-48]. Nowadays, the perovskite active layer has evolved from methylammonium lead iodide to the complex mixed halide compound $FA_{1-n}Cs_nPb(I_{1-x}Br_x)_3$. This transition was driven by the discovery of enhanced

light absorption and improved stability when employing formamidinium (FA) based perovskite materials [49-50]. Numerous investigations into lead-free perovskite materials, including $CH_3NH_3SnI_3$, $CsSn_{0.5}Ge_{0.5}I_3$, black orthorhombic $CsSnI_3$ or $CsSnI_{3-x}Br_x$ [51-55] have been proposed. However, these materials face challenges of poor stability and relatively low power conversion efficiency, just exceeding 10%. Addressing these primary challenges in the realm of lead-free materials remains an ongoing pursuit.

There are a large number of materials that are promising candidates for hole transport layer (HTL) or electron transport layer (ETL). Optimal energy-band alignment at the heterojunction between the perovskite and the ETL facilitates efficient electron extraction and minimizes energy losses. In an inverted planar structure, some inorganic material choices such as NiO_x, CuI, C_{60} coated-ZnO and C_{60} [56-60] have been reported. Recently, Chen et al. has shown significant interest in doped NiO_x, specifically focusing on the doping technique within NiO_x. Chen's work has reported a power conversion efficiency (PCE) of around 20% by employing various dopants such as Cu and Cs [61-63]. Yao et al. transplanted fullerenes onto ZnO through the binding of catechol on ZnO to improve the electron density and demonstrated a PCE up to 21.1% [59]. In addition, Yang et al. demonstrated a general passivation strategy by forming a thin, compact inorganic lead oxysalt layer on the perovskite surface in order to improve the interface quality with C_{60}, and the corresponding PCE reached 21.1% as well [60]. Unlike inorganic hole transport layers (HTLs), organic HTLs are more commonly used due to their advantages in achieving improved film coverage and better control over doping levels. Among these, PEDOT:PSS is a popular choice as a hole transport material (HTM) due to its favorable characteristics of high conductivity and cost-effectiveness. However, PEDOT:PSS's work

function is comparatively lower than other HTMs like PTAA and NiO_x, resulting in poor compatibility with typical perovskite materials. Consequently, the open-circuit voltage (V_{OC}) is limited to around 0.9V [64]-[68]. Extensive research has been conducted on various organic hole transport materials (HTMs) to achieve improved band alignment. Conductive polymers such as poly [N,N'-bis(4-butylphenyl)-N,N'-bis(phenyl)benzidine] (poly-TPD) [69]-[71] and poly(triaryl amine) (PTAA) [72]-[75] stand out as promising candidates due to their compatibility as anti-solvents to DMF or DMSO, solvents used for the perovskite active layer precursor, makes them attractive options. Nonetheless, their surfaces exhibit a non-wetting nature, resulting in adhesion challenges during the spin-coating process of the perovskite precursor. This issue contributes to inadequate perovskite film coverage, increased pin-hole density, and relatively small perovskite grain sizes. Bi et al. have showcased the influence of the hydrophobicity of the bottom layer surface on the perovskite grain size. They found that HTM surfaces with improved hydrophilicity are capable of facilitating the formation of larger perovskite grain sizes [72]. Recently, several significant advancements have emerged in the enhancement of conducting polymer HTMs. Xu et al. have reported that poly-TPD based perovskite solar cell with an inverted planar structure can have a PCE exceeding 18% [71] after an ultraviolet-ozone surface treatment. Hu et al. investigated the influence of molecular weight of poly-TPD and demonstrated that poly-TPD with 75 kDa possesses superior conductivity and the PCE can reach over 19% [72]. Furthermore, Macdonald et al. incorporated phosphorene nanoribbons (PNRs) into PTAA film to enhance hole extraction and Wu et al. inserted and alkylammonium interlayer between PTAA and perovskite layer to reduce the non-radiative energy loss. Both cases recently propelled the PCE to 21.14% [76] to 22.31% [77].

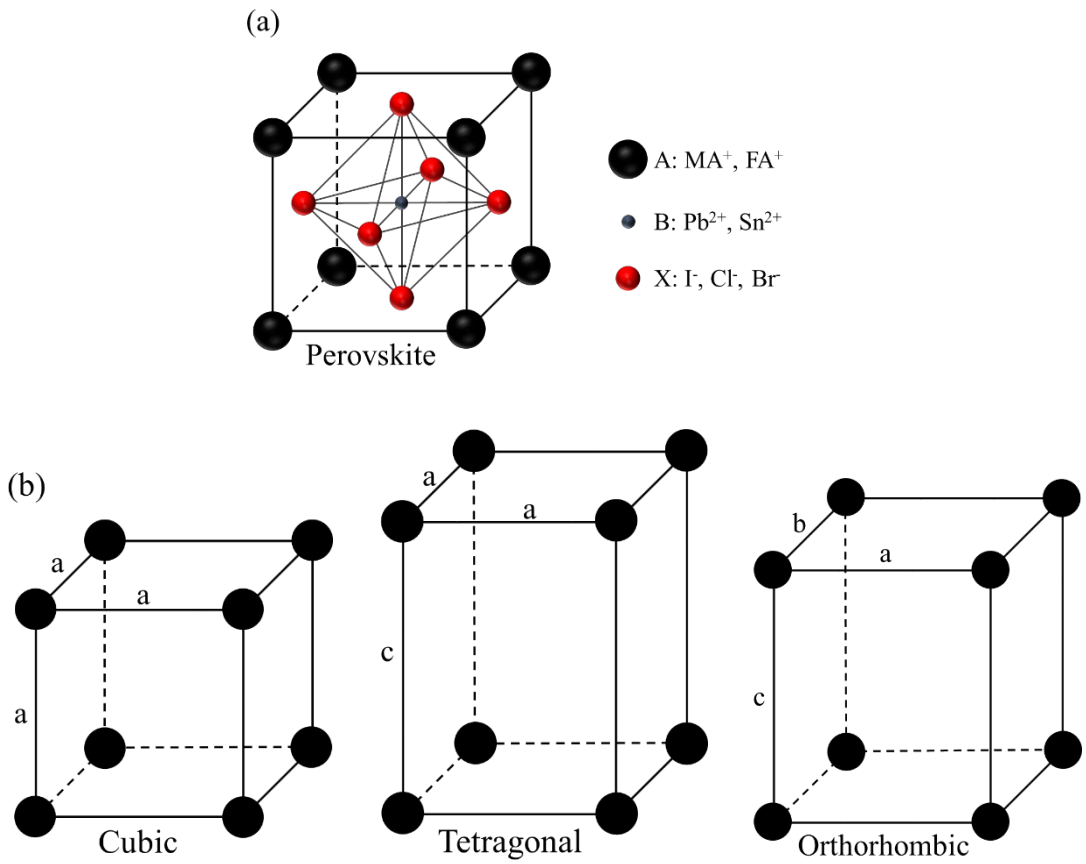

Fig. 4.1. (a) The structure of perovskite (b) Structure of cubic, tetragonal, and orthorhombic, where a ≠ b ≠ c.

A big advantage of perovskite material is the ambipolar charge transport property which allows them to effectively transport both types of charge carriers and enable them to function as both an active layer and a charge transport layer. This property is particularly crucial in perovskite solar cells, where perovskites can serve not only as the light-absorbing layer but also as the hole transport layer (HTL) and electron transport layer (ETL). Ambipolar transport can lead to enhanced charge extraction, reduced recombination losses, and improved overall device performance. Empirical findings have indicated impressive electron-hole diffusion lengths, surpassing 100 nm in solution-processed $CH_3NH_3PbI_3$, exceeding 150 μm in single crystals, and even reaching over 1 μm in mixed halide

$CH_3NH_3PbI_{3-x}Cl_x$. [78-81]. Perovskites exhibit significantly longer electron-hole diffusion lengths compared to typical solution-processed materials, which usually have diffusion lengths in the range of tens of nanometers. This enhanced performance is attributed to the relatively small effective masses of electrons and holes in $MAPbI_3$, calculated as m_e=0.23 m_o and m_h=0.29 m_o, respectively, facilitating their efficient ambipolar charge transport over long distances. [82]. The measured Auger recombination rate is on the order of 10^{-29} cm^6s^{-1} [82], which is comparable to a value of 7 x 10^{-30} cm^6s^{-1} for GaAs and 2-3 x 10^{-29} $cm^2V^{-1}s^{-1}$ for InGaAsP. The carrier mobility has been determined to be 11.6 $cm^2V^{-1}s^{-1}$ for $CH_3NH_3PbI_{3-x}Cl_x$ and 8 $cm^2V^{-1}s^{-1}$ for $CH_3NH_3PbI_3$, respectively [82]. The extended electron-hole diffusion length is attributed to the combination of low charge recombination rates and high charge carrier mobility within perovskite materials. Furthermore, perovskites exhibit a substantial absorption coefficient of over 5 x 10^5 cm^{-1}, particularly just above the band gap, characterized by a remarkably sharp onset.

4.1.2 Structural Configuration of Perovskite Solar Cell

Perovskite solar cells are typically designed in two configurations. The first is the superstrate configuration, where light enters the cell through the substrate. In this setup, the choice of substrate is restricted to transparent materials with high transmittance. The second configuration is the substrate configuration, in which light enters the cell from the opposite side. This configuration permits the use of substrates like stainless steel or metal foil; however, it necessitates the incorporation of transparent or semi-transparent top contacts. There are two dominant structures for the perovskite solar cell: the meso-porous (n-i-p) structure and the inverted (p-i-n) planar structure. The meso-porous structure, such as TiO_2 or Al_2O_3, usually requires a condensed base layer under high-temperature (usually

500ºC) annealing to minimize the leakage paths from the perovskite layer to the carrier transport layer [83-86]. Yang et al. and Min et al. from UNIST utilized perovskites with the conventional TiO_2 based structure, showing an improvement of PCE from 22.1% in 2017 [86] to 25.5% in 2021 [87]. In contrast, the inverted planar perovskite structure streamlines the fabrication process and allows for the utilization of lower-temperature techniques, all while maintaining a competitive power conversion efficiency (PCE). In this configuration, the hole transport layer (HTL) is deposited initially, with incident light first interacting with the HTL before reaching the perovskite and electron transport layer (ETL) components. The capability of perovskite materials to transport holes themselves led to the development of planar heterojunction inverted p-i-n perovskite solar cells. In recent developments, Wu et al. managed to elevate the power conversion efficiency (PCE) to 22.31% in 2020 [77], marking an improvement from the 21% achieved in 2018 [88]. Notably, both studies employed an inverted structure featuring a mixed-cation, mixed-halide lead perovskite material.

4.1.3 Perovskite Fabrication Methods

Various fabrication techniques have been developed to enhance the performance of thin-film perovskite solar cells in a planar configuration. These methods can be broadly categorized into three main approaches: one-step solution coating, two-step sequential deposition, and vapor phase deposition. One-step solution coating mixes all precursors into one solution and then applies the solution onto the substrate by using one of the following ways: spin coating, blade coating [90-91], spray-on coating [92-93] or even screen printing [94-95]. The two-step method involves sequentially applying two precursor solutions, allowing them to react and form the perovskite material. Techniques like spin coating or

dipping are commonly employed for this type of deposition process. Vapor phase deposition converts solid powder to vapor in a dedicated zone of a tube and then deposits onto substrates in another zone [96-97]. Several techniques have been introduced to improve the perovskite thin film morphology by solvent engineering [83] and precursor composition engineering. For example, incorporating HI as additives into the one or mixed perovskite precursors proves to enhance solution solubility, leading to a significant enhancement in the uniformity of the resulting perovskite thin films. By utilizing a solvent-assisted annealing technique, the crystallinity of the perovskite can be precisely tailored and optimized. During the annealing process, the presence of solvent vapor (such as DMF or IPA) assists in the crystallization of the perovskite film, resulting in the formation of larger perovskite grain sizes.

In the thesis, inverted planar structure is adopted due to the following advantages. Firstly, it simplifies the fabrication process, making it more efficient and cost-effective. Secondly, it allows for a lower temperature processing, which is beneficial for compatibility with various substrate materials and even flexible substrates. The sequentially doped PTAA, we previously proposed [98], was adopted. And a two-step sequential spin-coating inter-diffusion method with MAI/FAI composition engineering, followed by a solvent-assisted annealing technique is demonstrated for the fabrication of our perovskite solar cell.

4.2 Fabrication Details of Perovskite Solar Cell

In this section, the fabrication process of our perovskite solar cell is going to be presented in detail, which includes the materials, vendor information, and the detailed fabrication process.

4.2.1 Material and Equipment

A compact glove box was purchased from Changshu Willfo and paired with Neoprene dry-box gloves from Sigma Aldrich. FTO glass substrates and PbI_2 are also from Sigma Aldrich. PTAA is from Solaris Chem Inc. while m-MTDATA, F4-TCNQ and PCBM are from Lumtec. MAI, FAI, MABr are from Greatcell Solar Materials. The solvents, including DMF, 2-Propanol, Chlorobenzene, Toluene are from Alfa Aesar. The detailed information on all materials and equipment used during the fabrication process of perovskite solar cell are listed in the Table VI.

TABLE VI MATERIAL, EQUIPMENT AND VENDORS INFORMATION FOR PEROVSKITE SOLAR CELL

Name	Vendor	Specification
Compact Glove Box	Changshu Willfo	Size:W55xD44xH41cm
Neoprene Dry-Box Gloves	Sigma Aldrich	Size 9, Port size 6 inch
FTO Glass	Sigma Aldrich	13 Ω/sq sheet resistance
PTAA	Solaris Chem Inc.	5-20 kDa
F4-TCNQ	Lumtec, tw	Sublimed, >99%
m-MTDATA	Lumtec, tw	Sublimed, >99%

Lead iodide (PbI_2)	Sigma Aldrich	>99,99%
Methylammonium iodide (MAI)	Greatcell Solar Materials	>99.99%
Formamidinium iodide (FAI)	Greatcell Solar Materials	>99.99%
Methylammonium bromide (MABr)	Greatcell Solar Materials	>99.99%
(6,6)-phenyl-C61-butyric acid methyl ester (PCBM)	Lumtec, tw	>99.99%
N,N-Dimethylformamide (DMF)	Alfa Aesar	99.7+%, spec grade
2-propanal	Alfa Aesar	99.7+%, spec grade
Chlorobenzene	Alfa Aesar	99.9%, spec grade
Toluene	Alfa Aesar	99%, spec grade
Polyvinylidene (PVDF) Syringe Filter	Sterli Tech	0.45 μm
SCK-300 Spin Coater Kit	Instras Scientific	500-6000 rpm

4.2.2 Solution Preparation

The concentration of PTAA and F4-TCNQ are 2 mg/mL in toluene (with 0.2 mg/mL m-MTDATA as additive) and 1 mg/mL in 2-propanol, respectively. Both of these solutions require overnight stirring prior to use, ensuring thorough dissolution of all constituents. PbI_2 solution is 500 mg/mL in DMF and is ultra-sonicated in warm/hot water

(60°C) for at least an hour before filtered by using a 0.45 µm syringe filter. MAI (85 mg/mL in 2-propanol), FAI (92 mg/mL in 2-propanol) or MABr (5mg/mL in 2-propanol) is ultra-sonicated around room temperature for an hour. PCBM (20 mg/mL in chlorobenzene) needs to be ultra-sonicated in warm water (40-50°C) for at least an hour. In the case of the mixed MAI/FAI solution, MAI and FAI solutions are initially prepared separately and then blended with different volume ratios. Finally, an ultrasonic bath is employed for a duration of 30 minutes.

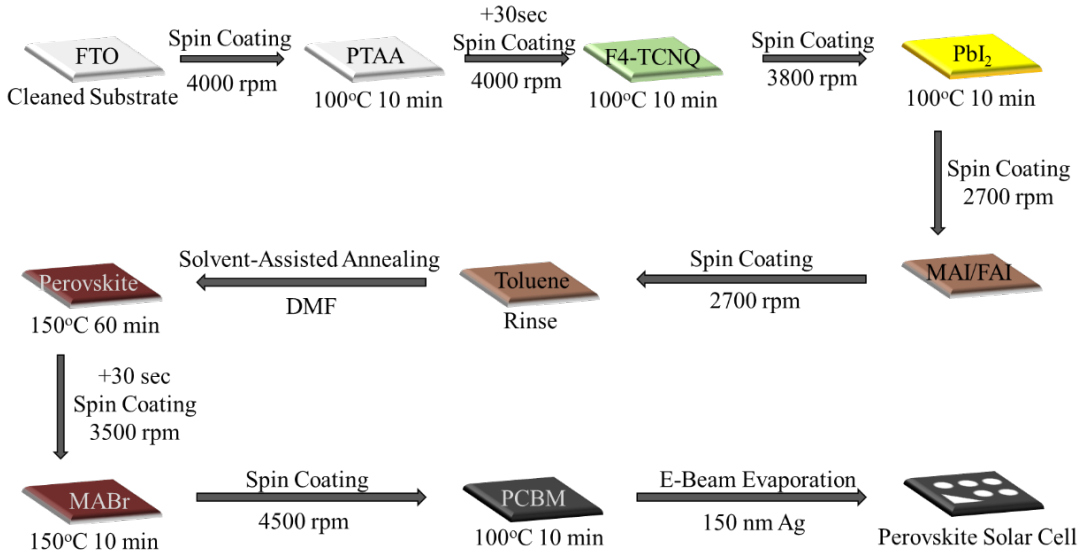

Fig. 4.2. The fabrication process of perovskite solar cell.

4.2.3 Perovskite Solar Cell Fabrication

Fig. 4.2 shows the fabrication process. First, in a clean room, the FTO glass substrates are cleaned with acetone, methanol and isopropanol, in that order, for 5-10 mins each in an ultra-sonic cleaner, followed by a deionized water rinse. Then The FTO substrates undergo a 24-minute Ultraviolet-Ozone (UV Ozone) treatment to decompose surface contaminants into volatile compounds, which then evaporate from the substrate surface. Prior to transferring the substrates to our compact glove box, it's essential to

eliminate any surface contaminants. Failure to do so could result in the marks on the substrates during the spin coating process, significantly compromising the uniformity and yield of the perovskite solar cell. Once the FTO substrates are inside our nitrogen-filled compact glove box, both the substrates and the PTAA solution undergo preheating at 100°C on a hot plate. Sequential doped PTAA is performed. 20 μL hot PTAA solution is spin-coated on the hot substrate at 4000 rpm for 45 s, followed by annealing at 100ºC for 10 mins. This PTAA layer is the hole transport layer of the perovskite solar cell. After the substrates are cooled down to room temperature, 25 μL F4-TCNQ doping solution is spread on the PTAA surface and left for 30 s before spin-coated at 4000 rpm for 45 s. The doped PTAA layer is dried by annealing at 100ºC for 10 mins.

The perovskite active layer is fabricated by our modified inter-diffusion method. Highly concentrated PbI_2 solution is pre-heated on a 100ºC hot plate along with the PTAA-coated substrate for 10 minutes. 25 μL hot PbI_2 solution (60-70ºC) is spin-coated at 3800 rpm for 35 s on the hot PTAA-coated substrate, followed by a 10-minute post annealing at 100ºC to dry out the DMF solvent in order to form a crystallized PbI_2 film. After the sample is cooled down to room temperature, 25 μL warm MAI or MAI/FAI mixed solution (around 50ºC) is spin-coated on the PbI_2 layer at 2700 rpm for 2 mins. As MAI is applied onto the PbI_2 surface, the sample's appearance transitions from transparent golden yellow to a matte light brown. Throughout the spin coating process, the color progressively deepens into a glossy brown, reflecting the ongoing reaction between PbI_2 and MAI as they form the perovskite film. 25 μL toluene is then spin-coated on to the sample for 30 s before the MAI spin coating ends. Toluene serves the purpose of eliminating any remaining MAI residue and passivating the perovskite active layer. Without this step, the presence of MAI residue

could notably degrade both the quality of the perovskite active layer and the interface between the perovskite active layer and the PCBM layer. The as-grown perovskite active layer is then annealed on a 150ºC hot plate for 60 mins by using our solvent-assisted annealing technique that facilitates the crystallization process with some solvent vapor (DMF) in the annealing environment. Fig. 4.3 shows the setup for the solvent-assisted annealing process. Some amount of solvent (DMF, typically from 5 to 30 μL) is dropped on to the cover glass in the middle while perovskite samples are around the cover glass. Then a large beaker is used to cover the solvent vapor. The amount of solvent vapor can be precisely controlled. As a result, solvent-assisted annealing is able to reduce the amount of pin-hole in the perovskite crystal and enlarge the grain sizes. However, the solvent amount must be precisely controlled since pin holes would start to emerge if too much solvent is added on to the cover glass.

After 60 mins of solvent-assisted annealing, the crystallized perovskite samples are cooled down to room temperature, followed by a diluted MABr solution treatment. Basically, diluted MABr solution is spread onto the perovskite surface for 30 s before spin-coated at 3500 rpm for 35 s. The incorporation of MABr into the perovskite film leads to the penetration of bromine, which in turn reduces the presence of dangling bonds along the grain boundaries. This is due to the smaller size of bromine compared to iodine, resulting in stronger binding energy. As a result, bromine can effectively recover the dangling bonds or replace weaker iodine bonds. For the electron-transport layer, 15 μL warm/hot (around 60ºC) PCBM solution is spin-coated at 4500 rpm for 30s, followed by annealing at 100ºC for 10 mins.

Finally, the samples are transferred to the clean room to deposit Ag contact. Before placing the samples into an Angstrom e-beam evaporation machine, a corner of the all the perovskite samples is wiped out to expose the bottom FTO layer. The cathode contact will be deposited directly on the exposed FTO region while the anode contact will be deposited on the PCBM. Both cathode and anode contact are defined through shadow mask with a chosen pattern. 150 nm Ag contact is deposited at a vacuum pressure of $3x10^{-6}$ torr. The effective device area is defined by the anode contact area that can be varied from 0.01 to 0.8 cm^2 with various shadow masks.

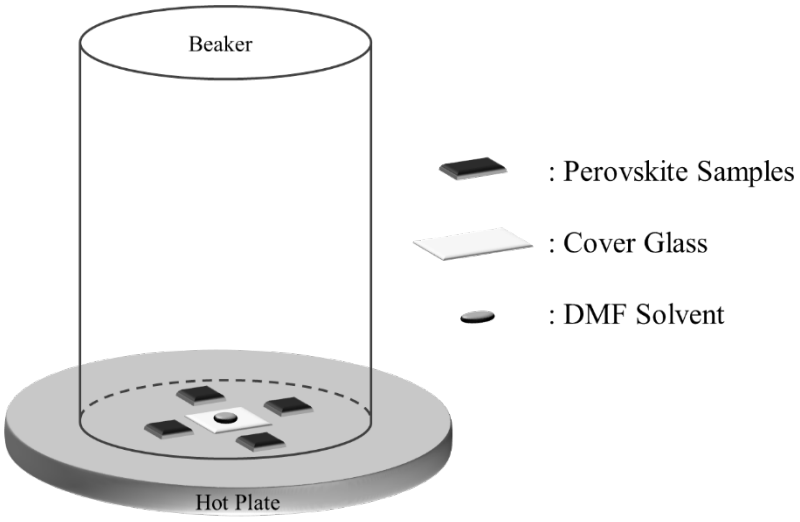

Fig. 4.3. The setup for the modified solvent-assisted annealing process.

4.2.4 Characterization Techniques and Tools

Various analysis tools are used to evaluate the material properties of the perovskite active layer as well as the performance of perovskite solar cell. To investigate the optical bandgap of the perovskite active layer, a Perkin Elmer Lamda 1050 UV/Vis/NIR Spectrophotometer is used to measure the absorbance of the perovskite film. The transmittance of perovskite film is measured by a 150 mm integrating sphere with a

photomultiplier (PMT) and a broadband InGaAs detector. To determine the crystalline structure and grain size, an X-ray diffractometer (XRD) and a Scanning Electron Microscope (SEM) are used. XRD measurements are taken on a Bruker D8 Advance/C2 Discover Parallel Beam Diffractometer using CuKα sealed X-ray tube with a graphite Göbbel mirror. The SEM images are acquired by a Hitachi SU-70 Schottky Field Emission Gun Scanning Electron Microscope. Grain size statistics are obtained by using the software "PhotoImpact X3" in contrast mode. To examine the power conversion efficiency of perovskite solar cell, the Newport Model 91159 Full Spectrum 150 W Solar Simulator is used to generate the appropriate solar spectrum. A KG-5 Si diode paired with one Air Mass 1.5 filter is required to ensure the light spectrum generated is about 1 sun. I-V characteristics of the perovskite solar cell are measured in ambient with a Keithley 2400 source-meter. I-V scanning speed can be adjusted to study hysteresis behavior. The External Quantum Efficiency (EQE) of perovskite solar cell is measured by using Xenon light source from which specific wavelength is selected by a monochromator. Photocurrent generated is measured by Thorlabs DET36A silicon photodetector and amplified with a Stanford Research Systems SR570 pre-amplifier connected to a Stanford Research Systems SR830 lock-in amplifier. For the case of the tandem cell, a Thorlabs DET30B Germanium detector is used instead for the wavelength range from 850 nm to 1350 nm.

4.3 Results and Analysis

4.3.1 Structure of Perovskite Solar Cell

An inverted planar perovskite solar cell with a tunable bandgap for the perovskite active layer that uses the superstrate configuration is proposed in my work. Fig. 4.4 (a) shows the solar cell structure. FTO glass is the substrate while PTAA doped with F4-TCNQ and PCBM are the hole transport layer and the electron transport layer, respectively. $FA_xMA_{(1-x)}PbI_3$ is the active layer with a tunable x value from 0 to 1 which leads to a tunable optical bandgap from 1.59 eV to less than 1.5 eV. Silver is the metal contact for both cathode and anode.

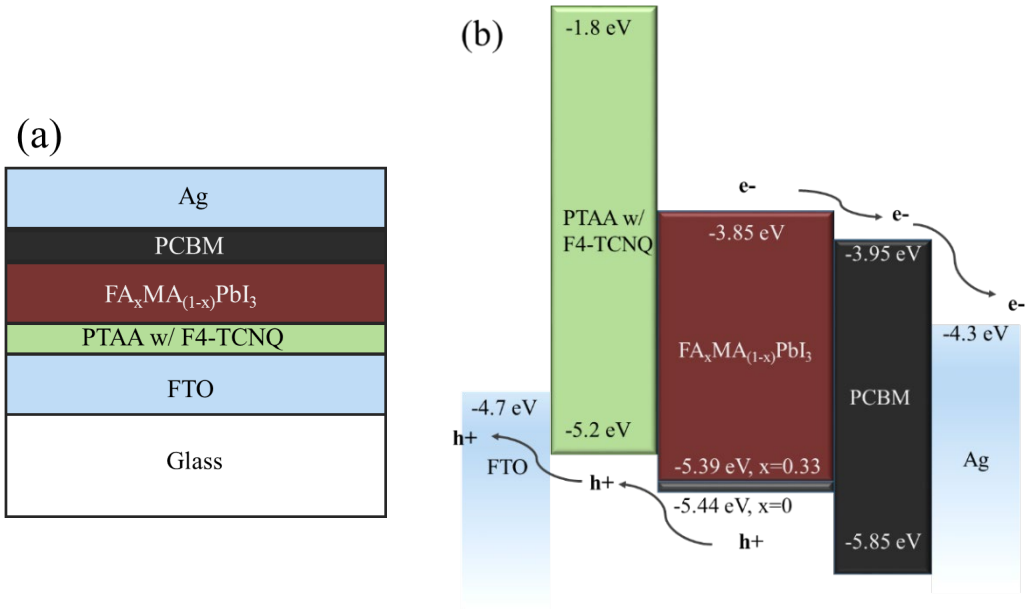

Fig. 4.4. (a) The inverted planar solar cell structure and (b) the corresponding energy band diagram

The corresponding energy band diagram is shown in Fig. 4.4 (b). PTAA is used as the hole transport layer because of a band alignment of PTAA which is more appropriate for our perovskite solar cell. The valance band energy level of PTAA (-5.2 eV) is lower than that of the widely-used PEDOT:PSS (-5.0 eV) and therefore the valance band energy

of PTAA is closer to that of perovskite (-5.3 to -5.44 eV). As a result, a larger quasi-Fermi level separation is created by using PTAA and a smoother pathway for the hole transport is established, which help increase the open-circuit voltage (V_{oc}) of the solar cell. Compared to the results that my colleague and I proposed in 2017 [99] which demonstrated a V_{oc} of 0.92 V for a PEDOT:PSS based perovskite solar cell, PTAA can enlarge the V_{oc} by around 0.1 V. In Fig. 4.3 (b) the valance band of perovskite $FA_xMA_{(1-x)}PbI_3$ layer is presented with the cases of x=0 and x=0.33 which are the best condition for tandem or single-junction solar cell, respectively. The detailed experimental results will be discussed in the following section. Moreover, our perovskite solar cell is illuminated from the FTO glass side so that the metal contact is also a mirror that reflects sunlight which creates more chances to absorb sunlight. The advantage of silver as the contact material is excellent band alignment as well as being an excellent reflector of visible light that leads to more light reflected back to perovskite active layer.

4.3.2 Optical Bandgap of Perovskite Active Layer

One of my goal is to optimize the single-junction perovskite solar cell. According to Shockley-Queisser limit [100], the optimized bandgap for a single-junction solar cell is 1.4 eV. It is well-known that the bandgap of $MAPbI_3$ is around 1.6 eV which is far from being the optimized bandgap. Therefore, FAI is incorporated into our perovskite film to lower the bandgap. Fig. 4.5 shows the Tauc plot for perovskite $FA_xMA_{(1-x)}PbI_3$ material. Fig. 4.5 (a) shows the MA-rich case while (b) shows the FA-rich case. Here, the perovskite $FA_xMA_{(1-x)}PbI_3$ material is assumed to be a direct bandgap material. Most research claim that $FA_xMA_{(1-x)}PbI_3$ material can be taken as a direct bandgap material. However, Ke et al. reported that indirect $MAPbI_3$ existed with increasing MAI content in perovskite precursor

[101]. Our $FA_xMA_{(1-x)}PbI_3$ material is believed to be a direct bandgap since the residual MAI has been washed away by a toluene rinse at the end of the spinning process before the solvent-assisted annealing.

In the case of no FAI incorporation (x=0), the bandgap of $MAPbI_3$ is observed as 1.59 eV, which is very close to the expected value of 1.6 eV. As the ratio of FAI increased, there is a clear trend that the bandgap goes down to 1.53 when the ratio between FAI and MAI becomes 1:1 (x=0.5). If the FAI concentration is further increased, the bandgap can reach 1.50 eV as the ratio between FAI and MAI becomes 5:1 (x=0.83). For a single-junction solar cell, a lower bandgap is preferred so more FAI or even $FAPbI_3$ (x=1) has the potential to out-perform $MAPbI_3$ (x=0) which our previous work has already demonstrated [98]. However, pure $FAPbI_3$ (x=1) has two phases; one is the α-phase which is black trigonal perovskite structure while the other is the δ-phase which is a yellow non-perovskite structure. It has been proposed that the transition temperature of the α-phase of $FAPbI_3$ from the δ-phase is 170°C [102-104]. Nevertheless, in my experiment, the α-phase of $FAPbI_3$ is never realized even though the annealing temperature is increased to over 180°C. The $FAPbI_3$ is still yellow to light brown after high temperature annealing. Despite the failure to fabricate $FAPbI_3$ perovskite film, FAI/MAI mixed perovskite layers with different FAI/MAI ratio ($FA_xMA_{(1-x)}PbI_3$) can be successfully fabricated and taken into further investigation.

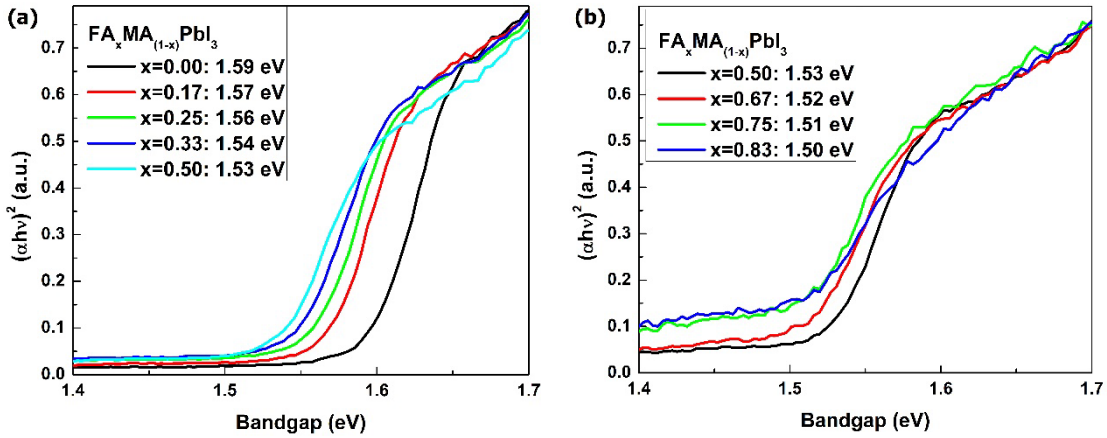

Fig. 4.5. The Tauc plot for perovskite $FA_xMA_{(1-x)}PbI_3$ material. (a) MA-rich case (b) FA-rich case.

4.3.3 I-V Characteristics of Perovskite Solar Cell

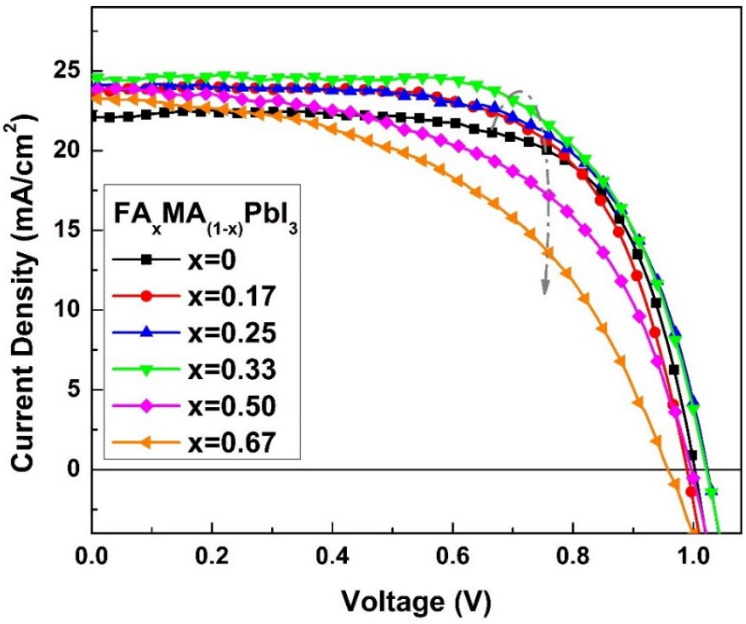

Fig. 4.6. I-V characteristics of $FA_xMA_{(1-x)}PbI_3$ solar cell with various FAI/MAI ratio.

The current-voltage (I-V) characteristics provide insights into the performance of the solar cell. The open-circuit voltage (V_{oc}), short-circuit current (J_{sc}), fill factor (FF),

power conversion efficiency (PCE) and many other parameters can be extracted from the I-V curves. The I-V characteristics of $FA_xMA_{(1-x)}PbI_3$ solar cell with various FAI concentration ratio x is shown in Fig. 4.6. Pure $MAPbI_3$ (x=0) cell has a V_{oc} of 1 V and J_{sc} of over 22 mA/cm^2. The FF is near 70% and the PCE is 15.3%. All of them except FF can be increased to 1.02 V, 24.5 mA/cm^2 and 16.5% respectively when x increases to 0.33, which is a $FA_{0.33}MA_{0.67}PbI_3$ solar cell. This is an improvement of 1.2% in efficiency while still keeping very good FF of 66% when compared to pure $MAPbI_3$ (x=0) cell. However, further increasing the amount of FAI or x does not improve the performance even more and instead, V_{oc}, J_{sc}, FF, and PCE all start to deteriorate. At x=0.67, V_{oc}, J_{sc}, FF, and PCE drop to 0.96 V, 23.3 mA/cm2, 49% and 11.15%, respectively. All of them represent the worst case among the curves show in Fig. 4.6.

Other solar cell parameters, including the series resistance and the shunt resistance can be extracted by using the following 1-diode model equation:

$$\mathrm{I} = I_L - I_0 \exp\left(\frac{q(V+IR_S)}{nkT}\right) - \frac{V+IR_S}{R_{sh}} \tag{4.1}$$

Where I_L is photocurrent, I_0 is reverse saturation current, k is Boltzmann constant, R_s is series resistance and R_{sh} is shunt resistance. When x=0, the reverse saturation current I_0 becomes smaller which means less recombination center inside the perovskite layer. This may indicate that a pure $MAPbI_3$ film has the least number of defects. The series resistance R_s has an increasing trend while the shunt resistance R_{sh} has the opposite trend with more FAI in the perovskite film. The I-V and fitting results are summarized in the table below. All of these results illustrate that incorporating FAI into the $MAPbI_3$ film can gradually deteriorate the $FA_xMA_{(1-x)}PbI_3$ perovskite quality, and some further analysis or material characterization needs to be conducted to verify the reason behind the degradation.

TABLE VII I-V CHARACTERISTICS FITTING RESULTS FOR PEROVSKITE WITH VARIOUS MAI/FAI COMPOSITION

FAI portion	Voc (V)	Jsc (mA/cm^2)	FF (%)	PCE (%)	R_s (Ωcm^2)	R_{sh} (Ωcm^2)	I_0 (mA/cm^2)
x=0	1	22.1	69	15.3	4.8	1120	6.9E-6
x=0.17	0.99	23.78	66.2	15.57	5.2	1038	1.3E-5
x=0.25	1.02	24.2	66	16.3	5.3	890	3.6E-5
x=0.33	1.02	24.5	65.7	16.5	5.6	842	4.3E-5
x=0.50	0.99	23.9	55	13.14	10.7	661	2.6E-4
x=0.67	0.96	23.3	49	11.15	14.1	460	3.9E-4

4.3.4 Crystal Structure and Grain Size Analysis of Perovskite Active Layer

To explore the impact of FAI incorporation on the crystal quality of the perovskite active layer, X-ray diffraction (XRD) analysis is employed to assess the crystalline structure. Fig. 4.7 shows the XRD results for PbI_2 film, and $FA_xMA_{(1-x)}PbI_3$ film when x= 0, 0.33 and 0.67.

All the tested films are fabricated on FTO glass substrate and hence there are peaks, marked with asterisk (*), that are contributed by FTO substrate. The black curve shows PbI_2 film has hexagonal structure with a prominent (001) peak at 12.7° [105]. There is no such peak after the $FA_xMA_{(1-x)}PbI_3$ film is fabricated, which demonstrates all the PbI_2 has fully reacted with the MAI or the FAI/MAI mixed solution. As for the red curve, the

$MAPbI_3$ film, there are several strong peaks at 14.3°, 20.1°, 28.6°, 32°, and 40.7° indicating (110), (112), (220), (310), (224) of cubic structure, respectively [106]. For $FA_xMA_{(1-x)}PbI_3$ film with x=0.33 or 0.67, both of them share almost every peak, indicating that those two films have the same crystal structure. Even though many peaks seem to be similar to the peaks of $MAPbI_3$ film, they are actually slightly off. Some stronger peaks are at 14°, 19.92°, 24.48°, 28.24°, 33.76° and 40.4°, corresponding to (110), (120), (021), (222), (030), (240) of the trigonal structure [106]. Those difference clearly demonstrates that once FAI is introduced into the perovskite film, the crystal structure transforms from the cubic to the trigonal structure.

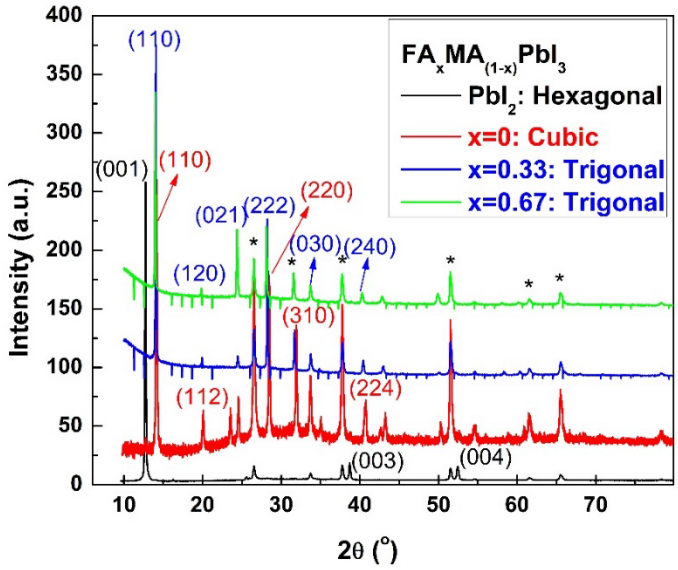

Fig. 4.7. XRD results for PbI_2 film, and $FA_xMA_{(1-x)}PbI_3$ film when x= 0, 0.33 and 0.67. Peaks marked with * are contributed by the FTO substrate.

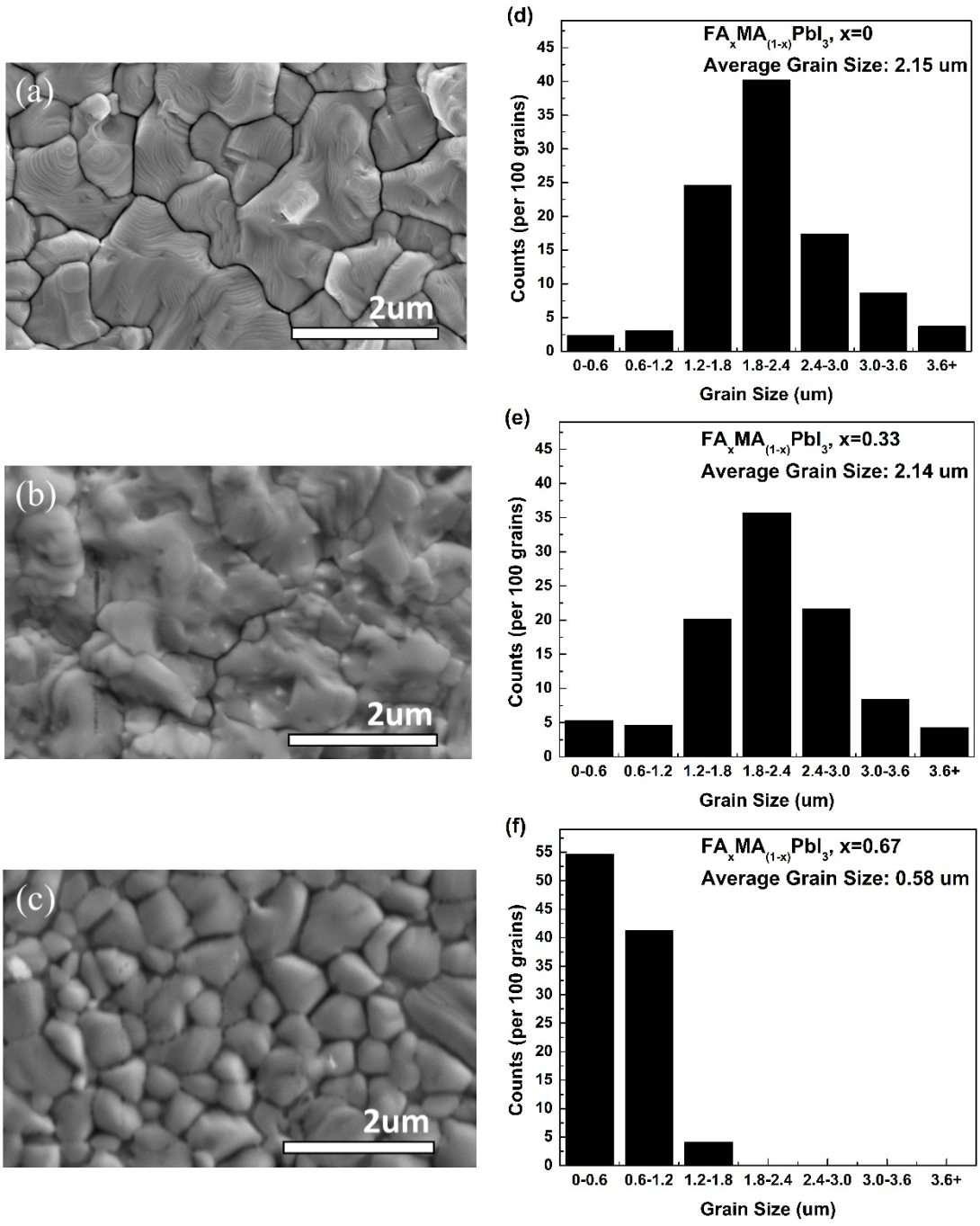

Fig. 4.8. The top view SEM image of $FA_xMA_{(1-x)}PbI_3$ with x=0, 0.33 and 0.67 (a) to (c) and the corresponding grain size distribution (d) to (f).

Besides XRD analysis, SEM images are also used to verify the crystal quality. Fig. 4.8 (a) to (c) displays the top view of $FA_xMA_{(1-x)}PbI_3$ film with x=0, 0.33 and 0.67, respectively. All three images have the same magnification of 20K. The crystal lines are

clearly shown in the image of x=0 film, indicating a very high degree of crystallinity. The crystal lines of the x=0.33 film is less prominent, which means a lower degree of crystallinity. In addition, the surface of the x=0.33 film is not as smooth as that of x=0 film. Even far less degree of crystallinity is observed from the image of the x=0.67 film. Barely any crystal line can be observed. The grains become more like pebble stones with smooth surfaces. Considering the grain size distribution demonstrated by Fig. 4.8 (d) to (f), the x=0.67 film possess average grain size of 0.58 μm that is a lot smaller than the size of the other two films (both over 2 μm). In addition, most of the grains are only less than 1 μm. As a result, there are more grain boundaries in the x=0.67 film, leading to higher potential of recombination due to surface defects and therefore lowering the FF and PCE of $FA_xMA_{(1-x)}PbI_3$ with the x=0.67 solar cell. Though x=0 and x=0.33 films have similar average grain size of over 2 μm as well as grain size distribution, the x=0 film has better crystallinity which contributes to a higher FF and better fitting parameter by using 1-diode model. The x=0.33 film has a lower optical bandgap which can utilize more solar spectrum. Even with less degree of crystallinity, the x=0.33 film still can generate higher J_{sc} (> 24 mA/cm^2) which is the main reason for the higher PCE (> 16%).

4.3.5 Optimization of Single-Junction Perovskite Solar Cell

So far, $FA_xMA_{(1-x)}PbI_3$ with x=0.33 solar cell, which is $FA_{0.33}MA_{0.67}PbI_3$ active layer, has the best performance. The incorporation of FAI into the perovskite active layer leads to a reduction in the optical bandgap to 1.54 eV, resulting in an increase in the short-circuit current to more than 24 mA/cm^2 without compromising the open-circuit voltage. Consequently, the power conversion efficiency surpasses 16%, even though the degree of

crystallinity is not as high as that of the $MAPbI_3$ (x=0) film. To enhance the crystallinity of the $FA_{0.33}MA_{0.67}PbI_3$ (x=0.33) film, varying amounts of solvent during the solvent-assisted annealing are employed to investigate the potential improvement in crystal quality. Fig. 4.9 demonstrates the SEM images of the x=0.33 film with 10, 20 or 30 μL DMF solvent during the solvent-assisted annealing process. Fig. 4.9 (b) shows the x=0.33 film with 20 μL DMF solvent with the same condition as used in the previous section to fabricate the $FA_xMA_{(1-x)}PbI_3$ layer with different x values. Therefore, the grain size distribution can be used here as a reference when the influence of various amounts of DMF solvent is investigated.

The results shown in Fig. 4.9 (a) demonstrate that with only 10 μL of DMF solvent, the grains exhibit the smallest size. The majority of grains measure around 1 μm, with an average grain size of 0.86 μm, suggesting inadequate DMF solvent for effective crystallization. Upon increasing the DMF solvent to 30 μL, as depicted in Fig. 4.9 (c), the grains remain relatively large, but the appearance of smaller grains indicates the fragmentation of some larger grains due to excessive DMF solvent. The average grain size reduces to 1.68 μm. Consequently, 20 μL of DMF solvent is identified as the optimal quantity for achieving solvent-assisted annealing.

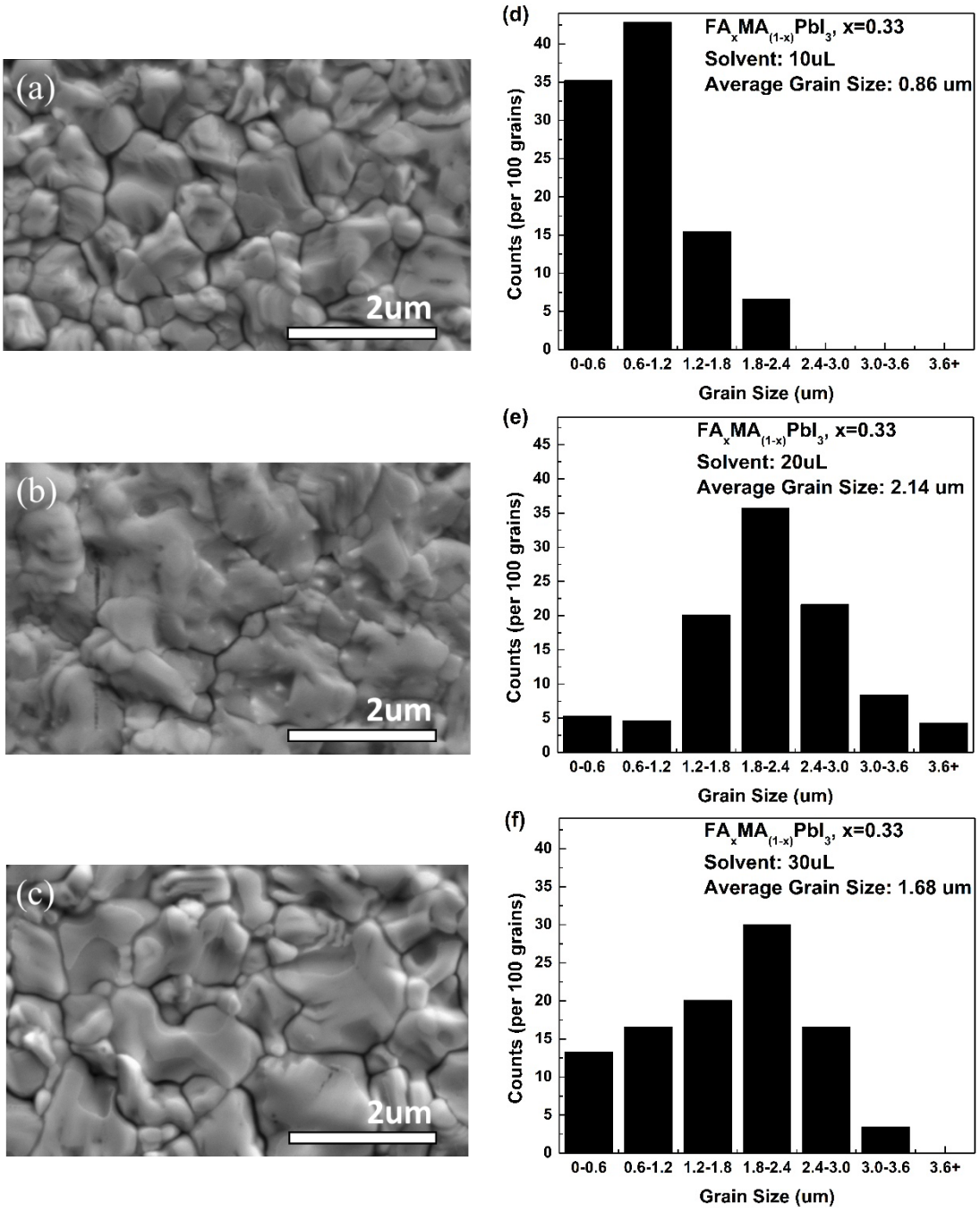

Fig. 4.9. The top view SEM image of $FA_{0.33}MA_{0.67}PbI_3$ with 10, 20 or 30 μL DMF solvent (a) to (c) and the corresponding grain size distribution (d) to (f).

The I-V characteristics of $FA_{0.33}MA_{0.67}PbI_3$ solar cell is shown in Fig. 4.10. The device with 20 μL DMF solvent has the highest power conversion efficiency of 16.5%,

while the other two devices (with 10 or 30 μL DMF) can only reach 14.45% and 15.63% respectively due to smaller grain size and less degree of crystallinity.

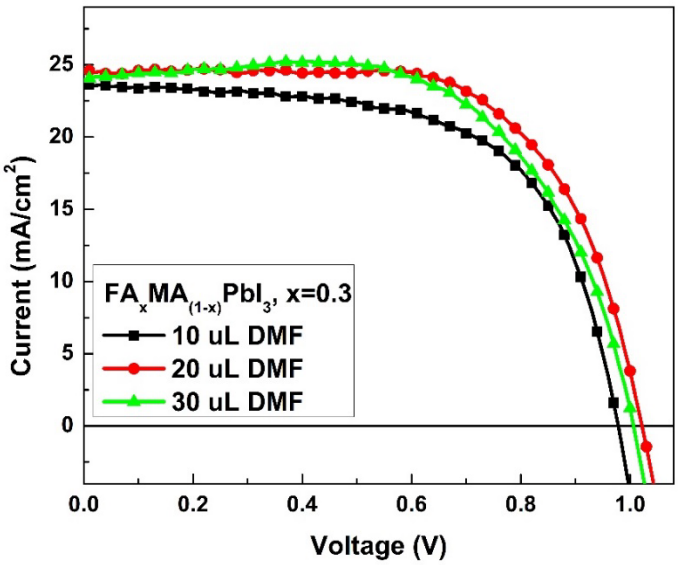

Fig. 4.10. The I-V characteristics of $FA_{0.33}MA_{0.67}PbI_3$ solar cell with various DMF solvent amount during solvent-assisted annealing.

Hysteresis has been observed and reported in most perovskite devices using metal oxide as the carrier transport layer. There is a difference of I-V curves depending on the scan directions. The ion migration hypothesis has been proposed to account for hysteresis effects [107]-[108]. When ions, such as MA^+ and I^-, migrate from one side of the perovskite layer to the other, the device's charge distribution, capacitance, and induced electric field experience corresponding changes. This results in distinct I-V responses when the device is measured in different directions. The phenomenon of ion migration is primarily attributed to light-soaking. After light-soaking, ions within the perovskite layer migrate toward the interface between the perovskite and the carrier transport layers under the

influence of an externally applied voltage, giving rise to the formation of dipoles. These dipoles can impede carrier extraction, leading to the observed hysteresis behavior. Fig. 4.11 illustrates the schematic of ion migration. Prior to light-soaking, positive and negative ions within the perovskite layers are uniformly distributed, and the only existing electric field across the perovskite layer is generated by the externally applied voltage, inducing ion drift. However, after the light-soaking process, ion migration becomes active within the perovskite layer. Consequently, an additional electric field comes into play, influencing the ions' behavior within the layer and contributing to their diffusion, which impedes their extraction.

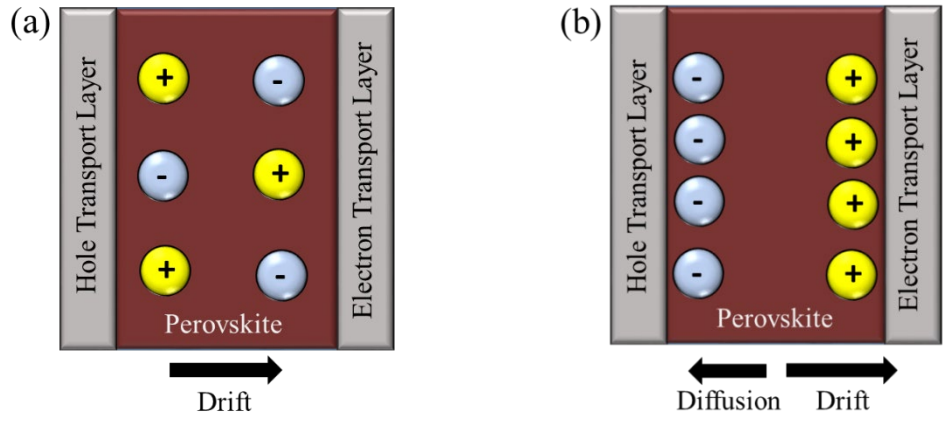

Fig. 4.11.1 The schematic of ion migration in perovskite layer (a) before light-soaking and (b) after light-soaking.

The widely accepted explanation for this phenomenon is ion migration, supported by the development of numerical models that simulate ion migration in perovskites [109], along with photothermal-induced resonance (PTIR) microscopy images that provide evidence of ion migration [110]. The research revealed that the activation energy for ion migration increases with larger grain sizes. Consequently, in order to mitigate ion migration within perovskite solar cells, the focus should be on achieving larger grain sizes.

Our suggested solvent-assisted annealing technique is capable of enhancing grain sizes, thus playing a role in diminishing ion migration.

Moreover, PCBM is employed to effectively mitigate hysteresis and attain hysteresis-free perovskite solar cells. It's crucial that the application of PCBM follows the spin-coating process of the perovskite active layer, as applying it beforehand would lead to the PCBM layer being washed away during the perovskite spin-coating step. Consequently, the use of PCBM is particularly relevant in the inverted structure perovskite solar cells. Unlike other electron transport layers, such as metal oxide materials, PCBM particles have the ability to interact with moving ions, forming a PCBM halide radical [111]. This interaction leads to a reduction in the density of interface dipoles, effectively reducing hysteresis effects. Fig. 4.12 presents the I-V outcomes of the champion cell, displayed in both the forward and reverse directions, highlighting the efficacy of PCBM in diminishing hysteresis. While the forward scan displays slightly less stability compared to the reverse scan, the I-V characteristics for both scan directions exhibit strong correlation. Although a minor level of hysteresis is still observed in half of the devices, the impact of PCBM in reducing hysteresis remains substantial.

However, another perspective has emerged among perovskite researchers, suggesting that the hysteresis effect could stem from electronic defects [112-115]. This notion is particularly relevant due to the low-temperature processes typically involved in perovskite solar cell fabrication, which could lead to an increased presence of defects. These defects might exist within specific material layers or at the interfaces between layers. In particular, interfaces involving metal contacts and semiconductors are more prone to interface defects due to lattice mismatches and electronic disparities. During I-V

measurements under external voltage, carriers can become trapped at these defects and subsequently released, leading to some variations in the I-V curves. Although the specific defect levels remain unidentified, comprehensive research and investigation are necessary to uncover the underlying principles behind hysteresis.

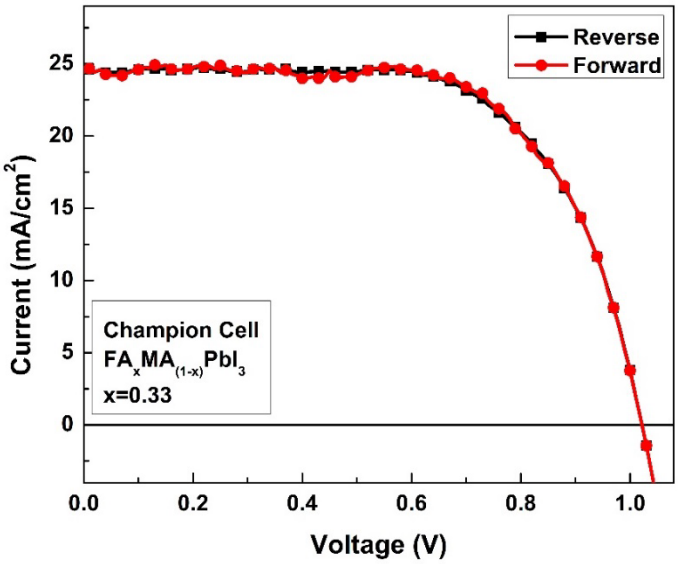

Fig. 4.12. The I-V results of champion cell in both forward and reverse direction.

Finally, the external quantum efficiency (EQE) is measured to compare the optimized single-junction perovskite solar cell with our previous results. Fig. 4.13 compares the EQE of $FA_{0.33}MA_{0.67}PbI_3$ (x=0.33) solar cell and $MAPbI_3$ (x=0) solar cell that my colleague and I had reported. The EQE of $FA_{0.33}MA_{0.67}PbI_3$ (x=0.33) solar cell remains around 90% from around 350 nm and all the way to over 600 nm, and starts to show a decreasing trend from 650 nm. However the EQE can still remain over 80% until 760 nm. Compared to $MAPbI_3$ (x=0) solar cell, the EQE of $FA_{0.33}MA_{0.67}PbI_3$ (x=0.33) solar cell is slightly lower at 300-400 nm region. The two solar cells have similar

performance from 400 to 600 nm; both can achieve around 90%. In the higher wavelength region, the $FA_{0.33}MA_{0.67}PbI_3$ (x=0.33) solar cell starts to shine. The EQE of $FA_{0.33}MA_{0.67}PbI_3$ (x=0.33) solar cell decreases more slowly as compared to that of the $MAPbI_3$ (x=0) solar cell. The absorption onset of $FA_{0.33}MA_{0.67}PbI_3$ (x=0.33) is around 820 nm, which is an improvement from the 790 nm of $MAPbI_3$ (x=0) solar cell. The integrated short-circuit current of the $FA_{0.33}MA_{0.67}PbI_3$ (x=0.33) solar cell is 24.1 mA/cm^2, which is comparable to the I-V measurement mentioned in the previous section. On the other hand, the integrated short-circuit current of $MAPbI_3$ (x=0) solar cell is 21.9 mA/cm^2, which is over 2 mA/cm^2 smaller than the optimized condition. Overall, by introducing FAI, the lower bandgap of $FA_{0.33}MA_{0.67}PbI_3$ film helps to utilize the solar spectrum to a fuller extent, and hence there is a great improvement in the higher wavelength region without sacrificing the EQE too much in the lower wavelength region.

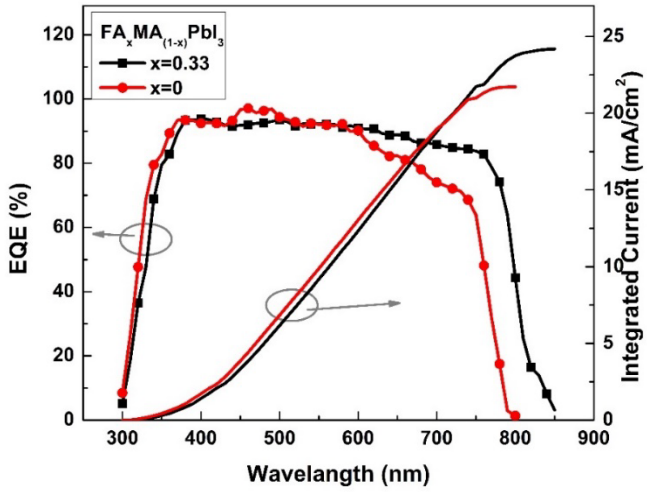

Fig. 4.13. 2Comparison between the EQE of $FA_{0.33}MA_{0.67}PbI_3$ (x=0.33) solar cell and $MAPbI_3$ (x=0) solar cell, and the corresponding integrated current

4.4 Summary

A $FA_xMA_{(1-x)}PbI_3$ perovskite solar cells with a tunable composition x from 0 to 0.83 are fabricated and presented in the chapter and the tunable optical bandgap is achieved. By incorporating FA^+ into $MAPbI_3$ material, the optical bandgap can be reduced from 1.59 to 1.50 eV with increasing composition ratio of FA^+. With lower optical bandgap, more solar spectrum can be absorbed by the $FA_xMA_{(1-x)}PbI_3$ perovskite material. A superstrate configuration, with an inverted planar structure, is adopted in our demonstration to realize a low temperature fabrication. The structure of the $FA_xMA_{(1-x)}PbI_3$ perovskite solar cell is FTO glass/PTAA with F4-TCNQ/Perovskite/PCBM/Ag. PTAA works as the hole transport layer while PCBM is the electron transport layer. Sequential PTAA doping and solvent-assisted annealing techniques are used to improve the performance of $FA_xMA_{(1-x)}PbI_3$ perovskite solar cell.

XRD and SEM are used to investigate the crystal quality of the perovskite film. XRD results indicate that the PbI_2 crystal has a hexagonal structure, and it has fully reacted with MAI or MAI/FAI solution after the spin-coating process. The $MAPbI_3$ (x=0) film is a cubic structure while both the $FA_xMA_{(1-x)}PbI_3$ films with x=0.33 and 0.67 transforms to tetragonal structure after FA^+ incorporation. SEM images clearly demonstrate that $MAPbI_3$ (x=0) film has the highest degree of crystallinity with average grain size over 2 μm. However, the degree of crystallinity declines as the FAI proportion increases, resulting in smaller grain size and more grain boundaries which lowers the fill factor and hence deteriorates the solar cell performance due to more traps and recombination centers. On the other hand, the lower bandgap of $FA_xMA_{(1-x)}PbI_3$ perovskite contributes to higher short-circuit current. Thus, for a single-junction solar cell, $FA_{0.33}MA_{0.67}PbI_3$ perovskite material

is the optimized ratio and the corresponding PCE is 16.5%, with V_{oc} of 1.02 V and J_{sc} of 24.5 mA/cm^2. A fill factor of 66% is calculated due to a slightly lower crystallinity of the film when FAI is incorporated. Compared to $MAPbI_3$ solar cell, there is an improvement of 1.2% in PCE and 2.4 mA/cm^2 for J_{sc} despite a slightly lower FF from 69% to 66%. The EQE of the $FA_{0.33}MA_{0.67}PbI_3$ perovskite solar cell is above 90% over a broad range from 400 to over 600 nm and remains above 80% up to 760 nm. In comparison to $MAPbI_3$ solar cell, it shows a significant improvement in the region around 600 nm. In addition, the absorption onset is pushed further to around 820 nm due to a lower optical bandgap of 1.54 eV.

Chapter 5 Perovskite-CIS Tandem Solar Cell

5.1 Introduction of Perovskite Tandem Solar Cell

Tunable optical bandgap, low-cost and low-temperature process (inverted structure) makes perovskite solar cell a potential candidate for the top cell of tandem solar cell system. In addition, the latest breakthrough reported from NREL has shown that the best PCE of single-junction perovskite cell has recently been boosted to 26% [36], which surpasses the efficiency of CIGS or CdTe solar cell. The perovskite solar cell efficiency will continue to challenge the record of silicon solar cell with heterojunction structure of 26.81% [116]. Therefore, perovskite tandem solar cells will continue to attract much attention. Moreover, gaining advantages from some already established technologies such as Si and CIGS (or CIS) solar cell, perovskite tandem cells can lead to significantly higher power conversion efficiencies and is therefore an appealing approach to consider for commercial applications where one would use a perovskite top cell and a Si or CIGS (or CIS) bottom cell [117-118]. However, additional process cost in making tandem solar cell should be thoroughly considered with the gain of efficiency over the top efficiency of a single-junction cell. Furthermore, both the current matching and the unequal degradation time between the top and bottom cell need to be studied further.

Two-terminal tandem solar cell has the potential to reach higher PCE than that of four-terminal configuration due to less buffer layer or contact layer which inevitably absorb light. Another advantage for a two-terminal tandem cell is lower cost since the power from the tandem cell is collected together, and therefore there is only one pair of ports in comparison to two separate pair of ports needed in the case of the four-terminal counterpart.

However, when talking about degradation or stability in long-term operation, a four-terminal tandem cell has the edge over two-terminal cell. Here, the perovskite top cell and the Si or CIS bottom cell are used as an example. Due to the unbalanced degradation between the perovskite cell and the Si or CIS cell, and since perovskite solar cells deteriorate much faster, a four-terminal configuration might be a safer choice to go. Moreover, since the power generated from the top and bottom solar cells is collected separately, current matching can be avoided.

Perovskite as a top cell has been widely studied for tandem solar cell applications. The low-temperature processed perovskite with an inverted structure is the most popular approach since it is compatible with a Si heterojunction bottom cell. Therefore a variety of optimized techniques have been reported recently. Bush et al. has proposed that by using an ALD SnO_2 buffer layer in the top contact, the underlying layer can be protected from the damage caused by the sputtering system at a later stage in the fabrication and hence an efficiency of 23.6% has reported [119]. Then, Sahli has implemented a n-type nanocrystalline silicon (nc-SiO_x:H) interlayer that enhanced coupling light into the Si bottom cell and demonstrated a 25.2% tandem cell [120]. In addition, by using grain engineering and tuning the bandgap of perovskite top solar cell, Chen et al. proposed a tandem cell with efficiency above 25.5% [121]. Most recently, NREL just revealed that Scientists at King Abdullah University of Science and Technology (KAUST) in Saudi Arabia have developed a perovskite-silicon solar cell with a power conversion efficiency of 33.7% [36].

5.2 Fabrication of CIS Bottom Solar Cell

In chapter 4, the fabrication process of our perovskite solar cell has been presented. Our group has already proposed a mature fabrication approach for realizing a of CIS solar cell [34]. In this section, a brief discussion of the fabrication of $CuInSe_2$ (CIS) solar cell is presented.

5.2.1 Brief Fabrication Process of CIS Solar Cell

Our CIS solar cells are fabricated on soda-lime glass with 400-nm thick molybdenum coating by using a two-step sequential process which is based on annealing and selenization of stacked elemental layers in a partially closed graphite box with Se vapor.

First of all, Cu and In metallic precursor layer are sequentially deposited by using DC magnetic sputtering system to form stacked elemental layers. Precise control is required to form a slightly In-rich CIS film with atomic Cu/In ratio of 0.95. To achieve the ratio of 0.95, Cu/In thickness ratio of 0.4290 is required. Also, the final thickness of the CIS absorber layer is about triple the thickness of the metallic precursor. Therefore, to fabricate a 2-μm thick CIS layer, a total thickness of 200 nm and 466.3 nm is required for Cu and In, respectively. Then, the stacked elemental layers is selenized with Se vapor and hence turns to a CIS film. Basically, this selenization process is a three-step annealing process, which is very crucial to get a p-type CIS film and is conducted in a graphite box with Selenium pellets at the bottom of the box. The temperature is increased from room-temperature to 125°C and kept at a temperature of 125°C for 30 min. Then the temperature is increased again to 250°C and stays at 250°C for another 30 min. Finally, the graphite is

heated up again to 500°C and kept there for another 30 min. Afterwards the graphite box cools down gradually to room temperature.

Next, post-deposition treatment process is performed. 20-nm KF thin layer is evaporated thermally on the surface of CIS active layer and then DI water rinse is necessary to wash the sample. Finally, the sample is annealed in a graphite box at 350 °C for 20min with Se vapor. 60 nm CdS buffer layer is deposited by chemical bath deposition in an alkaline aqueous solution. The solvents are 0.015 M cadmium sulfate ($CdSO_4$), 1.5 M Thiourea (NH_2CSNH_2), 14.8 N, 28-30% Ammonia (NH_4OH). The temperature is kept at 65ºC for 14 mins. The transparent conductive oxide (TCO) layer of 80 nm i-ZnO and 120 nm ZnO:Al are deposited by RF sputtering before 50 nm Ni and 1.3 μm Al layers are deposited by e-beam evaporation as the top metal contact.

5.2.2 Characterization Techniques and Tools

To examine the power conversion efficiency (PCE) of the perovskite-CIS tandem solar cell, the same solar simulator system is used when single-junction perovskite solar cell is tested which includes the same simulator, Air Mass 1.5 filter,Si diode and source-meter. The External Quantum Efficiency (EQE) of perovskite solar cell is measured by using the same self-built EQE system, same light source and monochromator included. However, the generated photocurrent is measured by a Thorlabs DET30B Germanium photodetector for the near-infrared response from 850 nm to 1350 nm. In my research, a four-terminal Perovskite-CIS tandem solar cell is proposed. To measure the I-V and EQE of the top perovskite solar cell, there is no difference as compared to a single-junction solar cell measurement. As for the bottom cell measurement, a top perovskite solar cell is

required to be placed in front of the bottom cell. Then the normal measurement approach is taken to get the characteristics of the CIS bottom solar cell.

5.3 Results and Analysis of Perovskite-CIS Tandem Solar Cell

5.3.1 I-V Characteristics of Perovskite-CIS Tandem Cell

The configuration of the tandem solar cell is perovskite as top cell and CIS as the bottom cell. Due to the fact that the optical bandgap of CIS bottom cell is 1 eV, the optimized bandgap for the perovskite top cell is around 1.6 eV which is discussed in the previous section. Therefore, the material for the perovskite top cell is $MAPbI_3$ with an optical bandgap of 1.59 eV. The I-V characteristics of the perovskite-CIS tandem solar cell is presented in Fig. 5.1. Top $MAPbI_3$ perovskite cell has identical performance as a single-junction cell. V_{oc}, J_{sc}, FF and PCE are 1 V, 22.1 mA/cm^2, 69% and 15.3%, respectively. The bottom CIS cell has a slightly lower V_{oc} of 0.46 V compared to 0.52 V for a single-junction CIS solar cell. J_{sc} drops significantly from 40.5 mA/cm^2 to only 13 mA/cm^2. The FF decreases slightly from 70.7% to 68%. The PCE of the bottom CIS cell is calculated to be 4.2%. Therefore, the total PCE of the perovskite-CIS tandem solar cell is 19.5%. In comparison to the best single-junction $FA_{0.33}MA_{0.67}PbI_3$ perovskite cell, there is a boost of 3%. However, the CIS bottom cell used in the measurement was fabricated more than two years ago and has been kept in ambient since then. As a result, the performance of the bottom CIS solar cell decreases. V_{oc} remains similar to the fresh cell while J_{sc} has decreased by around 5-10 mA/cm^2. Assuming that the CIS bottom cell was recently fabricated, the

PCE of the CIS solar cell could have been around 6%. The total PCE of tandem cell could easily be over 20%, closer to 21-22%.

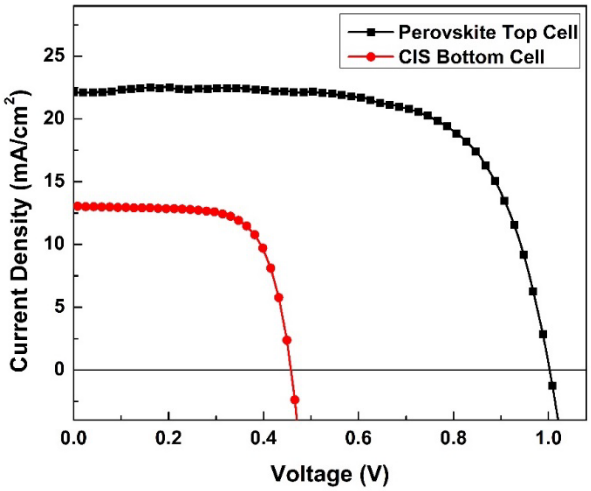

Fig. 5.1. The I-V characteristics of perovskite-CIS tandem solar cell

5.3.2 EQE of Perovskite-CIS Tandem Cell

The external quantum efficiency (EQE) of the perovskite-CIS tandem solar cell is presented in Fig. 5.2. The top $MAPbI_3$ perovskite cell has identical performance as a single-junction cell which is presented by the black. The EQE remains above 90% for the spectral range from 380 nm to 600 nm and then slowly drops to 80% at 680 nm. The EQE decreases drastically beyond a wavelength of 650 nm and eventually cutoff at 800 nm. Referring to the CIS bottom cell, displayed in red color, the performance in 400-800 nm spectral region is limited since most of the light is absorbed by the perovskite top cell. Only a small amount of light can reach the CIS bottom cell, so the EQE of CIS bottom cell in this region is below 20%. When the energy of incident light is below 1.59 eV, which is the optical bandgap of the perovskite top cell, the light is not absorbed by the perovskite top cell and therefore can

reach down to the CIS bottom cell. The EQE starts to increase and remains over 50% from 800 nm to 1000 nm. For the spectral region above 1000 nm, the EQE gradually decreases and finally cutoff around 1300 nm. The overall EQE in the 400-800 nm region remains above 80% and mostly over 90%. Since the tested CIS bottom cell is over two years of age, a better performance can be expected if a freshly fabricated CIS bottom cell was used. There will not be a huge difference in 400-800 nm region, but it is believed that in 800-1100 nm spectral region, the EQE could potentially be above 60%.

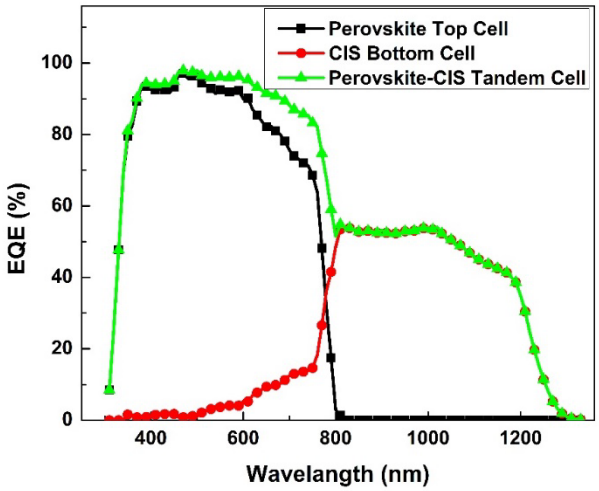

Fig. 5.2. The external quantum efficiency (EQE) of perovskite-CIS tandem solar cell

5.4 Summary

$FA_xMA_{(1-x)}PbI_3$ Perovskite solar cells with a tunable optical bandgap shows great potential in tandem solar cell application. Due to the mature fabrication technology of CIS solar cell in our group with an optical bandgap gap around 1 eV, the $MAPbI_3$ solar cell with optical bandgap of 1.59 eV can be a perfect fit as the top cell. In this chapter, a four-

terminal perovskite-CIS tandem solar cell is proposed with two separate working solar cells. The I-V characteristics and the EQE are measured to characterize the performance of the tandem solar cell. The champion cell demonstrates a PCE of 19.5% which is an improvement from 16.5% in PCE by the optimized single-junction of $FA_{0.33}MA_{0.67}PbI_3$ perovskite solar cells. However, the bottom CIS solar cell was more than two years of age which inevitably shows some performance degradation. The lower J_{sc} of CIS solar cell has been observed by at least 5-10 mA/cm^2 over the two-year period, which lead to significant deterioration of the overall PCE of the tandem cell. As a result, the overall PCE would be expected to be above 20% if a fresh bottom CIS solar cell was adopted in the tandem solar cell. Perovskite solar cell dominates the EQE at lower wavelengths, and CIS bottom cell provides a slight enhancement at 600 to 800 nm region. After the cut-off wavelength of perovskite solar cell around 800 nm, CIS demonstrates an EQE of 40 to 60% until 1200 nm. It is expected that the EQE could be over 60% across 800 to 1100 nm region if a freshly fabricated CIS solar cell is used to further improve the overall performance.

Chapter 6 Conclusion and Future work

6.1 Conclusion

In this work, Arrayed waveguide gratings (AWGs) are introduced, including the working principle, the aberration theory to Rowland AWGs and three-stigmatic-point (TSP) AWGs as well as Gerchberg-Saxton algorithm and cascaded AWG. Rowland AWGs are widely used in optical communication but in the proposed integrated photonic spectrograph, TSP AWG is required to provide flat image surfaces.

The design flow and simulation are discussed in detail. V-shaped and crossover structures are introduced and used to our AWG devices.

The transmission spectrum of TSP AWGs has been demonstrated and the corresponding resolving power has been calculated. For the lower resolving power design, the wavelength spacing is 0.5 nm and a V-shaped structure is adopted. The peak transmission can reach -1.9 dB and the highest resolving power is around 5,300. For the higher resolving power design, the wavelength spacing is 0.15 nm and the crossover structure is used. The peak transmission is -2.0 dB and the maximum resolving power goes above 18,000 and can remain above 17,000 across all channels. The side lobes are prominent due to larger phase error.

Due to the limitations of getting both high resolving and broad FSR, cascaded AWG is developed to broaden the FSR without increasing the footprint too much. Flat response is required for primary stage to prevent large loss at outer channels as well as the channel cross-points.

Design and simulation of flat-top primary AWG has been discussed in detail as well as the layout design and experimental results. The flat-top primary AWG is realized by modifying the power profile at the input aperture and the phase distribution at the output aperture.

TSP AWG is used as a secondary AWG for better cross-dispersion optics setup. In addition, one-top-hat and two-top-hat layout is utilized to closely position and align the output FPRs on the same image surface.

Cascaded AWGs have been fabricated and characterized with various combinations of Rowland, flat-top or top-hat AWG. Experimental results demonstrates that Rowland primary AWG has higher peak transmission but suffer significant loss at channel cross-points while flat-top primary AWG features slightly lower peak transmission but has huge improvement at channel cross-points for more than 12 dB experimentally. Cascaded AWG with flat-top primary stage shows flattened output profile within the passband, but performs poorly in filtering out unwanted signals outside the passband. The Rowland primary AWG filters out unwanted signal very well, with noise level at least 20 dB down experimentally.

A $FA_xMA_{(1-x)}PbI_3$ perovskite solar cells with a tunable composition x from 0 to 0.83 are realized and presented and the corresponding optical bandgap varies from 1.59 to 1.50 eV. By lowering the optical bandgap, the solar spectrum can be better utilized, meaning that more light can be absorbed by the $FA_xMA_{(1-x)}PbI_3$ perovskite material. A superstrate configuration, with an inverted planar structure, is adopted as our structure. The structure of the $FA_xMA_{(1-x)}PbI_3$ perovskite solar cell is FTO glass/PTAA with F4-TCNQ/Perovskite/PCBM/Ag. PTAA works as the hole transport layer while PCBM is the

electron transport layer. Sequential PTAA doping and solvent-assisted annealing techniques are used to improve the performance of $FA_xMA_{(1-x)}PbI_3$ perovskite solar cell.

In order to investigate the crystal quality of the perovskite film, XRD and SEM are used. XRD results indicates that the PbI_2 crystal has a hexagonal structure and it has fully reacted with MAI or MAI/FAI solution after the spin-coating process. The $MAPbI_3$ (x=0) film is a cubic structure while both the $FA_xMA_{(1-x)}PbI_3$ films with x=0.33 and 0.67 have tetragonal structure. SEM images clearly show that $MAPbI_3$ (x=0) film has the highest degree of crystallinity with average grain size over 2 μm. As the FAI proportion increases, the degree of crystallinity declines, resulting in smaller grain size and more grain boundaries which deteriorates the solar cell performance. As a results, for a single-junction solar cell, $FA_{0.33}MA_{0.67}PbI_3$ perovskite material is the optimized ratio and the corresponding PCE is 16.5%, with V_{oc} of 1.02 V and J_{sc} of 24.5 mA/cm^2. A fill factor of 66% is calculated due to a slightly lower crystallinity of the film when FAI is incorporated. Compared to $MAPbI_3$ solar cell, there is an improvement of 1.2% in PCE and 2.4 mA/cm^2 for J_{sc} despite a slightly lower FF. The EQE of the $FA_{0.33}MA_{0.67}PbI_3$ perovskite solar cell is above 90% of efficiency over a broad range from 400 to over 600 nm and remains above 80% around 760 nm. Compared to $MAPbI_3$ solar cell, it is a great improvement in the region around 600 nm, and the absorption onset is pushed to 820 nm due to a lower optical bandgap of 1.54 eV.

$FA_xMA_{(1-x)}PbI_3$ Perovskite solar cells with a tunable optical bandgap shows great potential in tandem solar cell application. Due to the mature fabrication technology of CIS solar cell with an optical bandgap gap around 1 eV, the $MAPbI_3$ solar cell with optical bandgap of 1.59 eV is a great fit as the top cell. In my work, a four-terminal perovskite-

CIS tandem solar cell is proposed. The I-V characteristics and the EQE are measured to investigate the solar cell performance. The champion cell demonstrates a PCE of 19.5% which improves the optimized single-junction of $FA_{0.33}MA_{0.67}PbI_3$ perovskite solar cells by 3%. However, the bottom CIS tested is more than two years of age. And the J_{sc} of CIS solar cell has been lowered by at least 5-10 mA/cm^2over the two year period, which lead to significant deterioration of the overall PCE. Therefore, if a new bottom CIS solar cell was used in tandem solar cell, the overall PCE would be expected to be above 20%.

6.2 Future Work

6.2.1 Polarization-Independent Array Waveguide Gratings

The design of the AWGs proposed in the thesis is based on the aberration theory which solves the optical path functions (OPFs) for the geometry of both input/output free propagation regions (FPRs). Therefore, the proposed AWGs are polarization dependent, and they are designed for TE polarization only. Since the light collected from the telescope is unpolarized, a polarization-independent AWG is required to better utilize the collected light. Several approaches of polarization-independent AWG have been proposed, such as varying waveguide widths for TE and TM to match the refractive index for two polarizations [122], changing the geometry of FPRs to compensate the birefringence dependence [123], and inserting a half-wave plate or polarization rotator at the center of each arrayed waveguide to cancel out the phase difference due to difference polarization [124]. However, changing the geometries of waveguides or FPRs requires precise control

of the thickness of the core layer and inserting new components adds complexity to the fabrication process.

To design a polarization-independent three-stigmatic-point (TSP) AWG can be even more challenging since the additional flat image surface is required. Therefore, it is believed that it is a practical approach to design two TSP AWGs for TE and TM polarization, respectively. The input light is separated by a polarization splitter before injected into the AWGs. However, it is inevitable that these two TSP AWGs must be separated by a few degrees, which leads to a slightly tilted output image surfaces and the corresponding larger defocus aberration compared to the original TSP AWGs. To solve this problem, these two TSP AWGs can be separated vertically into two different layers of Si_3N_4, instead of horizontally at the same Si_3N_4 layer. Another advantage of this design is achieving polarization-independent TSP AWG without increasing the footprint. However, due to the consideration of a pattern application for this novel design, the detail cannot be disclosed in the thesis.

6.2.2 Cascaded AWG with Reusable Delay line AWG

While our cascaded AWGs deliver flat responses inside the passband, the noise level outside the passband still needs to be improved. This is the result of phase errors along the output aperture needed to be compensated. Thus, the phase information at the modified tapers at the interface of input FPR and arrayed waveguides needs further investigation.

Our group has demonstrated a novel AWG with reusable delay lines (RDL AWG) to precisely control the power profile and phase distribution along the output aperture [125], which shows great potential to replace the flat-top AWG as the primary AWG. The traditional AWG creates constant phase difference by using a series of arrayed waveguides

with constant length differences. The RDL AWG utilizes a single waveguide to provide power profile and phase distribution through a series of directional couplers attached at the output aperture. By tuning the coupling lengths of each directional coupler and the phase of the bus waveguide, the power and phase can be precisely controlled along the output aperture. In addition, there is no input FPR and arrayed waveguides and thus, the footprint of RDL AWG is significantly smaller than the Rowland or TSP AWG.

RDL AWG can not only be used as a primary AWG, but it can also be applied to secondary AWG if larger resolving power is preferred. The footprint has been reduced by a factor of 71 with RDL AWG when the resolving power is as high as over 27,000 [126], which proves RDL AWG is also a great fit as a secondary AWG regarding to the application of astronomical observations which requires a continuous output spectrum. Besides, a series of spiral units as the delay line of RDL AWG has been proposed (SRDL AWG) [127], which can further reduce the footprint of the AWG by a factor of over 100 and achieve ultra-high resolving power (> 100,000). Each spiral unit possesses the same length, that can be easily adjusted to achieve different resolving power. A significantly reduced footprint of ARDL AWGs can reduce the chance of potential defects during fabrication as well as the flexure and thermal drift.

6.2.3 Improvement on Carrier Transport Layers of Perovskite Solar Cell

The FF of our $FA_{0.33}MA_{0.67}PbI_3$ perovskite solar cell is only 66% and this limits the PCE to 16.5%. In order to enhance the FF, further investigation of the electron transport layer is required. PCBM is the electron transport layer, and it proves to suppress hysteresis

by forming PCBM halide radical with migrating ions. However, not all $FA_{0.33}MA_{0.67}PbI_3$ perovskite solar cells are hysteresis-free. As a result, there is a possibility that some defects could appear at the interface between PCBM and the metal contact. BCP or C_{60} has been reported to be added as a buffer layer between the PCBM and the metal contact to further eliminate defect trap states at the interface [128-129]. Interface engineering becomes a very crucial field for optimizing the perovskite solar cell. Precise control of the layers thicknesses is necessary to realize better electron transport layers and thus improve the FF of perovskite solar cells.

6.2.4 Stability and Encapsulation

The stability issue has been a serious problem in the perovskite solar cell community. The PCE of our perovskite solar cell drops to 80-90% of its original value when our samples are placed three days in a desiccator, and even drops to 60-70% without desiccator. Recently, Huang et al. proposed that doped PEDOT:PSS effectively enhance the long-term stability without encapsulation [130]. Chiang et al. added a layer of cesium between the PCBM and the metal contact which also improved the stability [131]. Graphene, graphene oxide, and reduced graphene oxides are very promising alternatives as a buffer layer between PEDOT:PSS and FTO/ITO substrate [132-134]. In addition, a PFN-2TNDI or NDI-based polymeric electron transport layer has been proposed to replace PCBM as a new material for the electron transport layer [135].

Moisture is considered one of the most serious issues when talking about stability. $MAPbI_3$ will decompose into PbI_2 and MAI under moisture. To prevent the perovskite solar cell from moisture, fabrication environment must be in dry environment. Then encapsulation is needed after a perovskite film is fabricated. Encapsulation material has to

be against moisture and oxygen. Typically, a perovskite solar cell is sandwiched between two cover glass and is sealed with UV cured epoxy [136]. A variety of materials have been demonstrated as an encapsulation material, including Teflon, PMMA, or aluminum oxide. The effect of each material requires long-term monitoring, and a lot of work needs to be done before perovskite solar cell can be commercialized.

6.2.5 Perovskite-CIS tandem Cell in Two-Terminal Configuration

The perovskite-CIS tandem solar cell proposed in chapter 5 is a four-terminal tandem solar cell, which is basically two self-working solar cell. A better configuration for tandem solar cell is a monolithic two-terminal structure in series which contains fewer layers and potentially lowers the optical losses. Theoretically, the PCE is expected to be higher for a two-terminal tandem cell than that for a four-terminal stacked tandem cell because there is one recombination layer between the top and bottom solar cell in two-terminal configuration. Instead, for a four-terminal tandem cell, there are more transparent electrodes that inevitably absorb some light and therefore the PCE decreases accordingly.

However, to a achieve two-terminal tandem cell, a variety of optimization needs to be considered. For example, current matching needs to be investigated by tuning the effective area of top or bottom cell, adjusting the thickness of each solar cell, or tuning the recombination layer. The choice of recombination layer determines the carrier extraction. The band diagram needs to be matched without introducing any barrier for carrier transport. A potential perovskite-CIS tandem solar cell was proposed with the following structure: ITO/PCBM/ Perovskite/PTAA with F4-TCNQ/ITO (or AZO)/CdS/CIGS/Mo/Soda lime glass. In this structure, both the top and the bottom cells are connected in series by the

recombination layer, or interconnection layer, which consists of a PTAA layer and an ITO or AZO layer. The PTAA layer works as a hole recombination layer while the ITO or AZO layer functions as an electron recombination layer. The thickness of the recombination layer needs further research to increase the short-circuit current and match the current between two sub cells.

Chapter 7 Appendix

A. Chip Cleaving Accuracy Test

The performance characterization of our AWG devices is assessed by using a fiber-chip butt-coupling technique which involves cleaving each chip on both sides by using scribing and cleaving technique to expose the input/output waveguide facets. These facets are then coupled to the output PM fibers in our measurement setup. Most of the time, the cleaved lines don't match the intended lines marked for cleaving. Fortunately, the influence on transmission spectra is little if the output signals are recorded by power meter through output waveguides and the properly applied index-matching liquid. However, the inaccuracy of actual cleaved lines could significantly affect the output transmission spectra if the chip is cleaved at output image surface and the cross-dispersion setup is attached. According to the simulation results from Section 2.3.2, a deviation of the output image surface could lead to defocus aberration and deteriorate the resolving power. In Fig. 2.16, a mere 75-μm deviation in the image surface leads to a reduction of over 50% in resolving power.

The chip is placed on a three-axis moving stage under a microscope. A fixed scribing tip connected to a piezoelectric sensor is set above the chip. Once alignment is achieved through the microscope, the chip is elevated until the scribing tip makes contact with the surface. Subsequently, the chip is moved along the intended line's direction, so the surface of the chip is scratched by the tip. This process is repeated, with the chip being lifted by approximately 0.5 μm before another scratch is made along the cleaved line. This back-and-forth motion is iterated several times, continuing until the tip penetrates the top

cladding SiO_2 layer and reaches the Si substrate underneath. The scratched chip is transferred to another microscope where a razor blade is positioned below the scratched chip. After aligning the scratched line and the razor blade, the chip is manually pressed down against the razor blade, causing the chip to break. This action cleaves one side of the chip. The identical procedure is then employed on the chip's other side, thus finalizing the cleaving process.

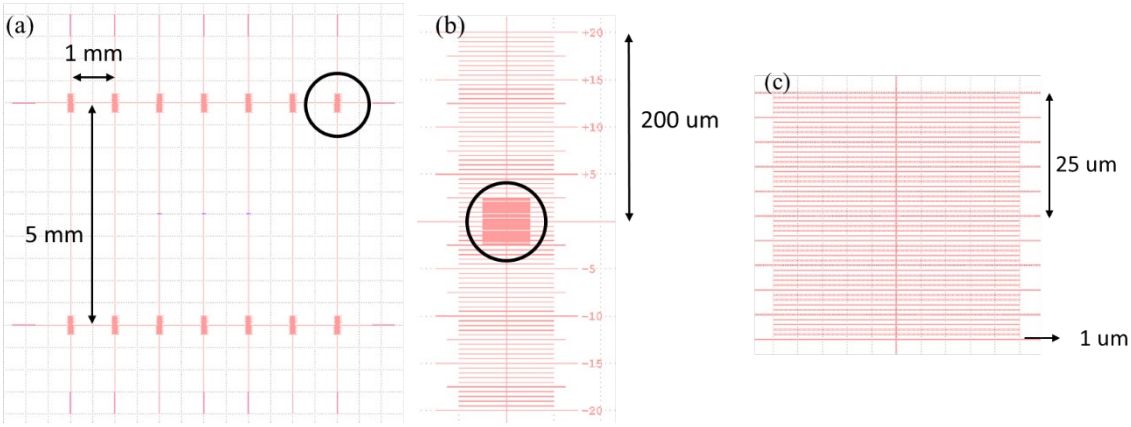

Fig. A.1. (a) Design of ruler set for cleaving line characterization; the black circle represents one ruler. (b) Closer view of one ruler; inside the black circle are the smaller tick marks. (c) The smaller ticks with 1μm separation.

The inaccuracy comes from the alignment using microscope and the force applied to break the chip. It is impossible to have a perfect scratch along the crystalline boundary of Si substrate and moreover, uneven force is applied to both side of the chip when the scratch is not at the center of the chip. This uneven force results in notable deviations in the actual break position. Fig. A.1 shows the design of the rulers used to characterize the cleaved lines. There are two sets of rulers corresponding to the two targeted lines. Each set consists of 7 rulers, spaced 1 mm apart, to record the positions of the cleaved line, as shown in part (a). Part (b) illustrates the ruler design, with tick marks spaced by 5 μm. Part (c)

provides a closer view of the center, displaying smaller ticks separated by 1 μm. Across 6 distinct chips, a total of 12 cleaving tests were conducted, with the outcomes summarized in Fig. A.2. Most of the samples exhibit a deviation ranging from tens to over a hundred μm except for sample 2 which is close to the targeted line within several micrometers. A trend of tilted cleaving lines is apparent, likely stemming from uneven force applied during the cleaving process. To provide a clearer overview, Fig. A.3 displays the average cleaving locations at each ruler's position, accompanied by error bars and standard deviations. The error bars represent the maximum and minimum value at each ruler position. The standard deviation at each ruler position can be calculated around 50 μm, which could significantly affect the resolving power based on the simulation. Therefore, an improvement of cleaving setup is required to attain accurate and consistent cleaving outcomes.

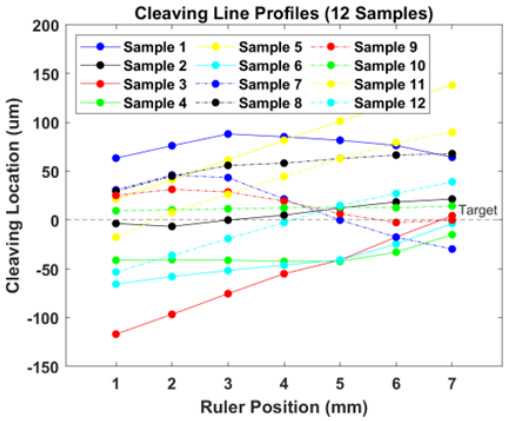

Fig. A.2. The results of 12 cleaving tests; zero represents the intended cleaving line.

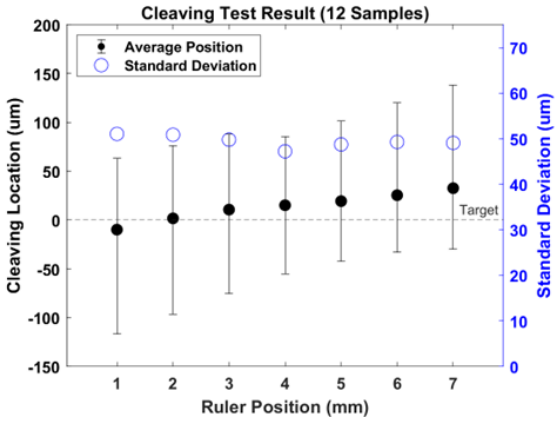

Fig. A.3. Average cleaving location and corresponding error bars and standard deviations.

Now, two strategies aimed at enhancing cleaving accuracy are proposed. The first one involves creating a deeper scratch on the Si substrate, effectively decreasing the thickness that needs to be fractured when pressed against the razor blade. However, there

is a possibility that scribing deeper could generate more cracks around the scratch, which may affect the devices fabricated on the front side of the ship. There larger buffer area between fabricated devices and the intended cleaving lines is required.

The second method centers on mechanically polishing the back side of the Si substrate, thus reducing its thickness. This reduction in the remaining thickness of the Si substrate results in a reduced force requirement for chip breakage. Consequently, it could lower the chance of slight movement of the chip when it is pressed down against the razor blade. Various investigations on wafer thinning have been proposed, such as the topology of the surface and the fracture strength [137], the bow and wrap of the thinned wafer [138], as well as the defects resulting from the thinning process [139]. The fracture strength of Si wafer is determined by the remaining thickness of Si wafer and the surface roughness after thinning process. A thicker silicon wafer offers increased rigidity; however, breaking it demands greater mechanical force. Increased surface roughness contributes to enhanced susceptibility to fracture or break. In addition, the induced compression and tensile stress are needed to be considered to prevent the devices on the front side of the Si wafer from having cracks due to the stress. It is believed that an optimized cleaving thickness often falls within the range of about 200 to 400 μm considering the rigidity, bow and wrap of the Si wafer, and the influence on the front side devices.

Bibliography

[1] A. Lowery, “Design of arrayed-waveguide grating routers for use as optical OFDM demultiplexers,” Opt. Express, vol. 18, no. 13, pp. 14129-14143, 2010.

[2] P. Dumon, W. Bogaerts, D. Thourhout, D. Taillaert, R. Baets, J. Wouters, S. Beckx, and P. Jaenen, “Compact wavelength router based on a Silicon-on-insulator arrayed waveguide grating pigtailed to a fiber array,” Opt. Express, vol. 14, no. 2, pp. 664-669, 2006.

[3] Y. Sano and T. Yoshino, “Fast Optical Wavelength Interrogator Employing Arrayed Waveguide Grating for Distributed Fiber Bragg Grating Sensors,” J. Lightwave Technol., vol. 21, pp. 132, 2003.

[4] J. Capmany, J. Mora, C. Fernández-Pousa, and P. Muñoz, “Quantum model of light transmission in array waveguide gratings,” Opt. Express, vol. 21, no. 12, pp. 14841-14852, 2013.

[5] J. Bland-Hawthorn and A. Horton, “Instruments without optics: an integrated photonic spectrograph,” Proc. SPIE, vol. 6269, no. 62690N, pp. N-14, 2006.

[6] N. Cvetojevic, N. Jovanovic, J. Lawrence, M. Withford, and J. Bland-Hawthorn, “Developing arrayed waveguide grating spectrographs for multi-object astronomical Spectroscopy,” Opt. Express, vol. 20, no. 3, pp. 2062-2072, 2012.

[7] P. Gatkine, S. Veilleux, and M. Dagenais, “Astrophotonic spectrographs,” Appl. Sci., vol. 9, no. 2, pp. 290, 2019.

[8] European southern observatory, 2023,

https://elt.eso.org/

[9] J. Bland-Hawthorn, S. C. Ellis, S. G. Leon-Saval, R. Haynes, M. M. Roth, H.-G. L¨ohmannsr¨oben, A. J. Horton, J.-G. Cuby, T. A. Birks, J. S. Lawrence, P. Gillingham, S. D. Ryder, and C. Trinh, “A complex multi-notch astronomical filter to suppress the bright infrared sky,” Nat. Commun., vol. 2, no. 1, pp. 581, 2011.

[10] T. Zhu, Y. Hu, P. Gatkine, S. Veilleux, J. Bland-Hawthorn, and M. Dagenais, “Arbitrary on-chip optical filter using complex waveguide Bragg gratings,” Appl. Phys. Lett., vol. 108, no. 10, pp. 101104, 2016.

[11] D. Wang, G. Jin, Y. Yan, and M. Wu, “Aberration theory of arrayed waveguide grating,” J. Lightwave Technol., vol. 19, no. 2, pp. 279–284, 2001.

[12] S. Lu, W. H. Wong, E. Y. B. Pun, Y. Yan, D. Wang, D. Yi, and G. Jin, “Design of flat-field arrayed waveguide grating with three stigmatic points,” Opt. Quantum Electron, vol. 35, no. 8, pp. 783–790, 2003.

[13] Y. Zhang, J. Zhan, S. Veilleux, and M. Dagenais, “Silicon Nitride Fabry-Perot Bragg Grating Nanoresonator with Ultrahigh Intrinsic Q,” in Conference on Lasers and Electro-Optics, Technical Digest Series (Optica Publishing Group, 2022), paper SM4G.7.

[14] A. Stoll, K. Madhav, and M. Roth, “Design, simulation and characterization of integrated photonic spectrographs for astronomy II: low-aberration generation-II AWG devices with three stigmatic points,” Opt. Express, vol. 29, no. 22, pp. 36226–36241, 2021.

[15] P. Gatkine, S. Veilleux, J. Mather, C. Betters, J. Bland-Hawthorn, J. Bryant, S. B. Cenko, M. Dagenais, D. Deming, S. Ellis, M. Greenhouse, A. Harris, N. Jovanovic, S. Kuhlmann, A. Kutyrev, S. Leon-Saval, K. Madhav, S. Moseley, B. Norris, B. Rauscher, M. Roth, S. Vogel, “Astro2020: Astrophotonics White Paper,” Submitted to the National Academy of Sciences for Astro 2020 Decadal Survey, Bulletin of American Astronomical Society, 51g.285G, pp. 1-14, 2019

[16] P. Gatkine, N. Jovanovic, C. Hopgood, S. Ellis, R. Broeke, K. Ławniczuk, J. Jewell, J. Wallace, and D. Mawet, “Potential of commercial SiN MPW platforms for developing mid/high-resolution integrated photonic spectrographs for astronomy,” Appl. Opt., vol. 60, no. 19, pp. D15-D32, 2021.

[17] K. Takada, H. Yamada, and K. Okamoto, “320-channel multiplexer consisting of 100 GHz-spaced parent AWG and 10 GHz-spaced subsidiary AWGs,” Electron. Lett., vol. 35, no. 10, pp. 824-826, 1999.

[18] K. Takada, M. Abe, T. Shibata, and K. Okamoto, “A.2.5 GHz-spaced 1080-channel tandem multi/demultiplexer covering the. S-, C-, and Lbands using an arrayed-waveguide grating with Gaussian passbands as a primary filter,” IEEE Photon. Technol. Lett., vol. 14, no. 5, pp. 648-650, 2002.

[19] B. I. Akca, C. R. Doerr, G. Sengo, K. Wörhoff, M. Pollnau, and R. M. de Ridder, “Broad-spectral-range synchronized flat-top arrayedwaveguide grating applied in a 225-channel cascaded spectrometer,” Opt. Express, vol. 20, no. 16, pp. 18313-18318, 2012.

[20] S. Kamei, Y. Doi, Y. Hida, Y. Inoue, S. Suzuki, and K. Okamoto, “Low-loss and flat/wide-passband CWDM demultiplexer using silica-based AWG with multi-mode output waveguides,” in Optical Fiber Communication Conference, Technical Digest (CD) (Optica Publishing Group), paper TuI2, 2004.

[21] S. Li, J. Zhang, L. Wang, J. You, Y. Wang, X. Yin, J. Chen, B. Sun, J. An, Y. Wu, “The O-band 20-channel 800 GHz Arrayed Waveguide Grating based on silica platform for 1 Tb/s or higher-speed communication system,” Opt. Laser Technol., vol. 156, pp. 108475, 2022.

[22] A. Junming, Y. Wu, H. Wang, J. Li, B. Xing, X. Hu, "Flat-top arrayed waveguide grating using a tapered multimode interferometer," Opt. Eng., vol. 45, no. 9, pp. 094601, 2006.

[23] T. Shibata, S. Kamei, T. Kitoh, T. Tanaka, and M. Kohtoku, "Compact and low insertion loss (~1.0 dB) Mach-Zehnder interferometer-synchronized arrayed-waveguide grating multiplexer with flat-top frequency response," Opt. Express, vol. 16, no. 21, pp. 16546-16551, 2008.

[24] Y. P. Ho, H. Li and Y. J. Chen, "Flat channel-passband-wavelength multiplexing and demultiplexing devices by multiple-Rowland-circle design," IEEE Photon. Technol. Lett., vol. 9, no. 3, pp. 342-344, 1997.

[25] M. Oguma, T. Kitoh, K. Jinguji, T. Shibata, A. Himeno and Y. Hibino, "Flat-top and low-loss WDM filter composed of lattice-form interleave filter and arrayed-waveguide gratings on one chip," OFC 2001. Optical Fiber Communication Conference and Exhibit. Technical Digest Postconference Edition (IEEE Cat. 01CH37171), pp. WB3-WB3, 2001.

[26] Z. Sheng, D. Dai and S. He, "Improve Channel Uniformity of an Si-Nanowire AWG Demultiplexer by Using Dual-Tapered Auxiliary Waveguides," y is J. Light. Technol., vol. 25, no. 10, pp. 3001-3007, 2007.

[27] G. Song, S. Wang, J. Zou, T. Lang, J.-J. He, "Silicon-based cyclic arrayed waveguide grating routers with improved loss uniformity," Opt. Commun., vol. 427, no. 15, pp. 628-634, 2018.

[28] B. Fondeur, A. L. Sala, H. Yamada, R. Brainard, E. Egan, S. Thekdi, N. Gopinathan, D. Nakamoto, and A. Vaidyanathan, "Ultrawide AWG with hyper-Gaussian profile," IEEE Photon. Technol. Lett., vol. 16, no. 12, pp. 2628-2630, 2004.

[29] Y. P. Ho, H. Li and Y. J. Chen, "Flat channel-passband-wavelength multiplexing and demultiplexing devices by multiple-Rowland-circle design," IEEE Photon. Technol. Lett., vol. 9, no. 3, pp. 342-344, 1997

[30] J. B. D. Soole, M.R. Amersfoort, H.P. Leblanc, N.C. Andreadakis, A. Rajhel, C. Caneau, R. Bhat, M.A. Koza., "Use of multimode interference couplers to broaden the passband of wavelength-dispersive integrated WDM filters," IEEE Photon. Technol. Lett., vol. 8, no. 10, pp. 1340-1342, 1996.

[31] S. Fan and D. Gao, "A Flat-top Arrayed Waveguide Grating Using A MMI Based on V-shaped Subwavelength Gratings," 2021 International Conference on Communications, Information System and Computer Engineering (CISCE), Beijing, China, pp. 225-228, 2021.

[32] K. Hassan, D. Khalil, M. Malak. and H. Anis, “Design of an arrayed waveguide grating optical demultiplexer for CWDM applications,” J. Opt. A: Pure Appl. Opt., vol. 10, no. 7, pp. 075307, 2008.

[33] R. W. Gerchberg and W. O. Saxton, “A Practical Algorithm for the Determination of Phase from Image and Diffraction Plane Pictures,” Optik, vol. 35, no. 2, pp. 237-246, 1972.

[34] Y. Zhang, R. E. Bartolo, S. J. Kwon, M. Dagenais, “High Short-Circuit Current Density in CIS Solar Cells by a Simple Two-Step Selenization Process With a KF Postdeposition Treatment,” IEEE Journal of Photovoltaics, vol. 7. No. 2, pp. 676-683, 2017.

[35] A. Kojima, K. Teshima, Y. Shirai and T. Miyasaka, "Organometal Halide Perovskites as Visible-Light Sensitizers for Photovoltaic Cells,” Journal of the American Chemical Society, vol. 131, no. 17, pp. 6050-6051, 2009.

[36] NREL.gov, 2023. [Online],

https://www.nrel.gov/pv/cell-efficiency.html

[37] P. Gao, M. Grätzel, and M. K. Nazeeruddin, “Organohalide lead perovskites for photovoltaic applications,” Energy Environ. Sci., Jun. 2014.

[38] J. You, L. Meng, T. Song, T. Guo, Y. Yang, W. Chang, Z. Hong, H. Chen, H. Zhou, Q. Chen, Y. Liu, N. De Marco and Y. Yang, "Improved air stability of perovskite solar cells via solution-processed metal oxide transport layers,” Nature Nanotechnology, vol. 11, no. 1, pp. 75-81, 2015.

[39] B. Suarez, V. Gonzalez-Pedro, T. S. Ripolles, R. S. Sanchez, L. Otero, and I. Mora-Sero, “Recombination Study of Combined Halides (Cl, Br, I) Perovskite Solar Cells,” J. Phys. Chem. Lett., vol. 5, no. 10, pp. 1628-1635, May 2014.

[40] J. H. Noh, S. H. Im, J. H. Heo, T. N. Mandal, and S. I. Seok, “Chemical Management for Colorful, Efficient, and Stable Inorganic–Organic Hybrid Nanostructured Solar Cells,” Nano Lett., vol. 13, no. 4, pp. 1764-1769, Apr. 2013.

[41] G. E. Eperon, S. D. S. , C. Menelaou , M. B. Johnston , L. M. Herz and H. J. Snaith, “Formamidinium lead trihalide: a broadly tunable perovskite for efficient planar heterojunction solar cells,” Energy Environ. Sci., vol. 7, pp. 982-988, 2014.

[42] E. L. Unger, L. Kegelmann, K. Suchan, D. Sörell, L. Korte and S. Albrecht, “Roadmap and roadblocks for the band gap tunability of metal halide perovskites,” J. Mater. Chem. A, vol. 5, no. 23, pp. 11401, 2017.

[43] T. Baikie, Y. Fang, J. M. Kadro, M. Schreyer, F. Wei, S. G. Mhaisalkar, M. Graetzel, and T. J. White, “Synthesis and crystal chemistry of the hybrid perovskite

(CH_3NH_3)PbI_3 for solid-state sensitized solar cell applications," J. Mater. Chem. A, vol. 1, no. 18, pp. 5628-5641, Apr. 2013.

[44] R. L. Milot, G. E. Eperon, H. J. Snaith, M. B. Johnston, L. M. Herz, "Temperature-Dependent Charge-Carrier Dynamics in $CH_3NH_3PbI_3$ Perovskite Thin Films," Adv. Funct. Mater., vol. 25, pp. 6218-6227, 2015.

[45] P. S. Whitfield, N. Herron, W. E. Guise, K. Page, Y. Q. Cheng, I. Milas & M. K. Crawford, "Structures Phase Transitions and Tricritical Behavior of the Hybrid Perovskite Methyl Ammonium Lead Iodide," Sci. Rep., vol. 6, pp. 35685, 2016.

[46] M. N. F. Hoque, N. Islam, K. Zhu and Z. Fan, "Hybrid Perovskite Phase Transition and Its Ionic," Electrical and Optical Properties. MRS Advances 2, pp. 3077–3082, 2017.

[47] G. Xing, N. Mathews, S. Sun, S. Lim, Y. Lam, M. Gratzel, S. Mhaisalkar and T. Sum, "Long-Range Balanced Electron- and Hole-Transport Lengths in Organic-Inorganic $CH_3NH_3PbI_3$," Science, vol. 342, no. 6156, pp. 344-347, 2013.

[48] C. Motta, F. El-Mellouhi and S. Sanvito, "Charge carrier mobility in hybrid halide perovskites," Scientific Reports, vol. 5, no. 1, 2015.

[49] Y. Sun, J. Peng, Y. Chen, Y. Yao and Z. Liang, "Triple-cation mixed-halide perovskites: towards efficient, annealing-free and air-stable solar cells enabled by Pb(SCN)2 additive," Scientific Reports, vol. 7, no. 1, 2017.

[50] L. Gil-Escrig, C. Dreessen, F. Palazon, Z. Hawash, E. Moons, S. Albrecht, M. Sessolo, and H. J. Bolink, "Efficient Wide-Bandgap Mixed-Cation and Mixed-Halide Perovskite Solar Cells by Vacuum Deposition," ACS Energy Lett., vol. 6, no. 2, pp. 827-836, 2021.

[51] N. K. Noel et al., "Lead-free organic–inorganic tin halide perovskites for photovoltaic applications," Energy Environ. Sci., vol. 7, no. 9, pp. 3061-3068, 2014.

[52] M. Chen, M. Ju, H. F. Garces, A. D. Carl, L. K. Ono, Z. Hawash, Y. Zhang, T. Shen, Y. Qi, R. L. Grimm, D. Pacifici, X. C. Zeng, Y. Zhou & N. P. Padture," Highly stable and efficient all-inorganic lead-free perovskite solar cells with native-oxide passivation," Nature Communications, vol. 10, no. 16, 2019.

[53] W. Chen, Y. Wu, Y. Yue, J. Liu, W. Zhang, X. Yang, H. Chen, E. Bi, I. Ashraful, M. Gratzel and L. Han, "Efficient and stable large-area perovskite solar cells with inorganic charge extraction layers," Science, vol. 350, no. 6263, pp. 944-948, 2015.

[54] T. Ye, X. Wang, K. Wang, S. Ma, D. Yang, Y. Hou, J. Yoon, K. Wang, and S. Priya, "Localized Electron Density Engineering for Stabilized B-γ CsSnI3-Based Perovskite Solar Cells with Efficiencies >10%," ACS Energy Lett., vol. 6, pp. 1480-1489, 2021.

[55] W. Zhang, Y. C., H. Liu, Y. Xia, J. Cui, Y. Shi, R. Chen, T. Shi, H.-L. Wang, “Organic-Free and Lead-Free Perovskite Solar Cells with Efficiency over 11%,” Adv. Energy Mater., vol. 12, no. 42, pp. 2202491, 2022.

[56] J. You, L. Meng, T. Song, T. Guo, Y. Yang, W. Chang, Z. Hong, H. Chen, H. Zhou, Q. Chen, Y. Liu, N. De Marco and Y. Yang, "Improved air stability of perovskite solar cells via solution-processed metal oxide transport layers,” Nature Nanotechnology, vol. 11, no. 1, pp. 75-81, 2015.

[57] S. Ye, H. Rao, Z. Zhao, L. Zhang, H. Bao, W. Sun, Y. Li, F. Gu, J. Wang, Z. Liu, Z. Bian and C. Huang, "A Breakthrough Efficiency of 19.9% Obtained in Inverted Perovskite Solar Cells by Using an Efficient Trap State Passivator Cu(thiourea)I,” Journal of the American Chemical Society, vol. 139, no. 22, pp. 7504-7512, 2017.

[58] J. Christians, R. Fung and P. Kamat, "An Inorganic Hole Conductor for Organo-Lead Halide Perovskite Solar Cells. Improved Hole Conductivity with Copper Iodide,” Journal of the American Chemical Society, vol. 136, no. 2, pp. 758-764, 2013.

[59] K. Yao, S. Leng, Z. Liu, L. Fei, Y. Chen, S. Li, N. Zhou, J. Zhang, Y. Xu, L. Zhou, H. Huang, A. K.-Y. Jen, “Fullerene-Anchored Core-Shell ZnO Nanoparticles for Efficient and Stable Dual-Sensitized Perovskite Solar Cells,” Joule, vol. 3, pp. 417-431, 2019.

[60] S. Yang, S. Chen, E. Mosconi, Y. Fang, X. Xiao, C. Wang, Y. Zhou, Z. Yu, J. Zhao, Y. Gao, F. De Angelis, J. Huang, “Stabilizing halide perovskite surfaces for solar cell operation with wide-bandgap lead oxysalts,” Science, vol. 365, pp. 473-478, 2019.

[61] W. Chen, Y. Zhou, L. Wang, Y. Wu, B. Tu, B. Yu, F. Liu, H. Tam, G. Wang, A. Djurišić, L. Huang and Z. He, "Molecule-Doped Nickel Oxide: Verified Charge Transfer and Planar Inverted Mixed Cation Perovskite Solar Cell,” Advanced Materials, vol. 30, no. 20, p. 1800515, 2018.

[62] W. Chen, Y. Wu, J. Fan, A. Djurišić, F. Liu, H. Tam, A. Ng, C. Surya, W. Chan, D. Wang and Z. He, "Understanding the Doping Effect on NiO: Toward High-Performance Inverted Perovskite Solar Cells,” Advanced Energy Materials, vol. 8, no. 19, p. 1703519, 2018.

[63] W. Chen, F. Liu, X. Feng, A. Djurišić, W. Chan and Z. He, "Cesium Doped NiOx as an Efficient Hole Extraction Layer for Inverted Planar Perovskite Solar Cells,” 2019.

[64] J. Seo, S. Park, Y. Chan Kim, N. Jeon, J. Noh, S. Yoon and S. Seok, "Benefits of very thin PCBM and LiF layers for solution-processed p-i-n perovskite solar cells,” Energy Environ. Sci., vol. 7, no. 8, pp. 2642-2646, 2014.

[65] W. Nie, H. Tsai, R. Asadpour, J. Blancon, A. Neukirch, G. Gupta, J. Crochet, M. Chhowalla, S. Tretiak, M. Alam, H. Wang and A. Mohite, "High-efficiency solution-processed perovskite solar cells with millimeter-scale grains," Science, vol. 347, no. 6221, pp. 522-525, 2015.

[66] J. You, Z. Hong, Y. Yang, Q. Chen, M. Cai, T. Song, C. Chen, S. Lu, Y. Liu, H. Zhou and Y. Yang, "Low-Temperature Solution-Processed Perovskite Solar Cells with High Efficiency and Flexibility," ACS Nano, vol. 8, no. 2, pp. 1674-1680, 2014.

[67] S. Sun, T. Salim, N. Mathews, M. Duchamp, C. Boothroyd, G. Xing, T. Sum and Y. Lam, "The origin of high efficiency in low-temperature solution-processable bilayer organometal halide hybrid solar cells," Energy Environ. Sci., vol. 7, no. 1, pp. 399-407, 2014.

[68] P. Liang, C. Chueh, S. Williams and A. Jen, "Roles of Fullerene-Based Interlayers in Enhancing the Performance of Organometal Perovskite Thin-Film Solar Cells," Advanced Energy Materials, vol. 5, no. 10, p. 1402321, 2015.

[69] D. Zhao, M. Sexton, H. Park, G. Baure, J. Nino and F. So, "High-Efficiency Solution-Processed Planar Perovskite Solar Cells with a Polymer Hole Transport Layer," Advanced Energy Materials, vol. 5, no. 6, p. n/a-n/a, 2015.

[70] O. Malinkiewicz, A. Yella, Y. Lee, G. Espallargas, M. Graetzel, M. Nazeeruddin and H. Bolink, "Perovskite solar cells employing organic charge-transport layers," Nature Photonics, vol. 8, no. 2, pp. 128-132, 2013.

[71] X. Xu, C. Ma, Y. Cheng, Y. Xie, X. Yi, B. Gautam, S. Chen, H. Li, C. Lee, F. So and S. Tsang, "Ultraviolet-ozone surface modification for non-wetting hole transport materials based inverted planar perovskite solar cells with efficiency exceeding 18%," Journal of Power Sources, vol. 360, pp. 157-165, 2017.

[72] X. Hu, C. Tao, J. Liang, C. Chen, X. Zheng, J. Li, J. Li, Y. Liu, G. Fang, "Molecular weight effect of poly-TPD hole-transporting layer on the performance of inverted perovskite solar cells," Solar Energy, vol. 218, pp. 368-274, 2021.

[73] C. Bi, Q. Wang, Y. Shao, Y. Yuan, Z. Xiao and J. Huang, "Non-wetting surface-driven high-aspect-ratio crystalline grain growth for efficient hybrid perovskite solar cells," Nature Communications, vol. 6, no. 1, 2015.

[74] Q. Wang, C. Bi and J. Huang, "Doped hole transport layer for efficiency enhancement in planar heterojunction organolead trihalide perovskite solar cells," Nano Energy, vol. 15, pp. 275-280, 2015.

[75] X. Zheng, B. Chen, J. Dai, Y. Fang, Y. Bai, Y. Lin, H. Wei, X. Zeng and J. Huang, "Defect passivation in hybrid perovskite solar cells using quaternary ammonium halide anions and cations," Nature Energy, vol. 2, no. 7, p. 17102, 2017.

[76] T. J. Macdonald, A. J. Clancy, W. Xu, Z. Jiang, C.-T. Lin, L. Mohan, T. Du, D. D. Tune, L. Lanzetta, G. Min, T. Webb, A. Ashoka, R. Pandya, V. Tileli, M. A. McLachlan, J. R. Durrant, S. A. Haque, C. A. Howard, "Phosphorene Nanoribbon-Augmented Optoelectronics for Enhanced Hole Extraction" J. Am. Chem. Soc., vol. 143, no. 41, pp. 21549-21559, 2021.

[77] S. Wu, J. Zhang, Z. Li, D. Liu, M. Qin, S. H. Cheung, X. Lu, D. Lei, S. K. So, Z. Zhu, A. K. Y. Jen, "Modulation of Defects and Interfaces through Alkylammonium Interlayer for Efficient Inverted Perovskite Solar Cells," Joule, vol. 4, no. 6, pp. 1248-1262. 2020.

[78] F. Deschler, M. Price, S. Pathak, L. E. Klintberg, D.-D. Jarausch, R. Higler, S. Hüttner, T. Leijtens, S. D. Stranks, H. J. Snaith, M. Atatüre, R. T. Phillips, and R. H. Friend, "High Photoluminescence Efficiency and Optically Pumped Lasing in Solution-Processed Mixed Halide Perovskite Semiconductors," J. Phys. Chem. Lett., vol. 5, no. 8, pp. 1421-1426, Apr. 2014.

[79] G. Xing, N. Mathews, S. Sun, S. S. Lim, Y. M. Lam, M. Grätzel, S. Mhaisalkar, and T. C. Sum, "Long-Range Balanced Electron- and Hole-Transport Lengths in Organic-Inorganic $CH_3NH_3PbI_3$," Science, vol. 342, no. 6156, pp. 344–347, Oct. 2013.

[80] S. D. Stranks, G. E. Eperon, G. Grancini, C. Menelaou, M. J. P. Alcocer, T. Leijtens, L. M. Herz, A. Petrozza, and H. J. Snaith, "Electron-Hole Diffusion Lengths Exceeding 1 Micrometer in an Organometal Trihalide Perovskite Absorber," Science, vol. 342, no. 6156, pp. 341-344, Oct. 2013.

[81] V. Gonzalez-Pedro, E. J. Juarez-Perez, W.-S. Arsyad, E. M. Barea, F. Fabregat-Santiago, I. Mora-Sero, and J. Bisquert, "General Working Principles of $CH_3NH_3PbX_3$ Perovskite Solar Cells," Nano Lett., vol. 14, no. 2, pp. 888-893, Feb. 2014.

[82] T. C. Sum and N. Mathews, "Advancements in perovskite solar cells: photophysics behind the photovoltaics," Energy Environ. Sci., Jun. 2014.

[83] N. Jeon, J. Noh, Y. Kim, W. Yang, S. Ryu and S. Seok, "Solvent engineering for high-performance inorganic–organic hybrid perovskite solar cells," Nature Materials, vol. 13, no. 9, pp. 897-903, 2014.

[84] N. Jeon, J. Noh, W. Yang, Y. Kim, S. Ryu, J. Seo and S. Seok, "Compositional engineering of perovskite materials for high-performance solar cells," Nature, vol. 517, no. 7535, pp. 476-480, 2015.

[85] W. Yang, J. Noh, N. Jeon, Y. Kim, S. Ryu, J. Seo and S. Seok, "High-performance photovoltaic perovskite layers fabricated through intramolecular exchange," Science, vol. 348, no. 6240, pp. 1234-1237, 2015.

[86] W. Yang, B. Park, E. Jung, N. Jeon, Y. Kim, D. Lee, S. Shin, J. Seo, E. Kim, J. Noh and S. Seok, "Iodide management in formamidinium-lead-halide–based perovskite layers for efficient solar cells," Science, vol. 356, no. 6345, pp. 1376-1379, 2017.

[87] H. Min, D. Y. Lee, J. Kim, G. Kim, K. S. Lee, J. Kim, M. J. Paik, Y. K. Kim, K. S. Kim, M. G. Kim, T. J. Shin and S. Seok, "Perovskite solar cells with atomically coherent interlayers on SnO2 electrodes," Nature, vol. 598, pp. 444. 2021.

[88] D. Luo, W. Yang, Z. Wang, A. Sadhanala, Q. Hu, R. Su, R. Shivanna, G. Trindade, J. Watts, Z. Xu, T. Liu, K. Chen, F. Ye, P. Wu, L. Zhao, J. Wu, Y. Tu, Y. Zhang, X. Yang, W. Zhang, R. Friend, Q. Gong, H. Snaith and R. Zhu, "Enhanced photovoltage for inverted planar heterojunction perovskite solar cells," Science, vol. 360, no. 6396, pp. 1442-1446, 2018.

[89]

[90] S. Tang, Y. Deng, X. Zheng, Y. Bai, Y. Fang, Q. Dong, H. Wei, J. Huang, "Composition Engineering in Doctor-Blading of Perovskite Solar Cells," Adv. Energy Mater., vol. 7, pp. 1700302, 2017.

[91] M. Yang, Z. Li, M. O. Reese, O. G. Reid, D. H. Kim, S. Siol, T. R. Klein, Y. Yan, J. J. Berry, M. F. A. M. van Hest, "Perovskite Ink with Wide Processing Window for Scalable High efficiency Solar Cells," Nat. Energy, vol. 2, pp. 17038. 2017.

[92] D. K. Mohamad, J. Griffin, C. Bracher, A. T. Barrows, D. G. Lidzey, "Spray-Cast Multilayer Organometal Perovskite Solar Cells Fabricated in Air," Adv. Energy Mater., vol. 6, pp. 1600994, 2016.

[93] D.-H. Lan, S.-H. Hong, L.-H. Chou, X.-F. Wang, C.-L. Liu, "High Throughput Two-step Ultrasonic Spray Deposited $CH_3NH_3PbI_3$ Thin Film Layer for Solar Cell Application," J. Power Sources, vol. 390, pp. 270−277, 2018.

[94] K. Cao, Z. Zuo, J. Cui, Y. Shen, T. Moehl, S. M. Zakeeruddin, M. Grätzel, M. Wang, "Efficient Screen Printed Perovskite Solar Cells Based on Mesoscopic $TiO_2/Al_2O_3/NiO$/carbon Architecture," Nano Energy, vol. 17, pp.171−179, 2015.

[95] A. Priyadarshi, A. Bashir, J. T. Gunawan, L. J. Haur, A. Bruno, Z. Akhter, N. Mathews, S. G. Mhaisalkar, "Simplified Architecture of a Fully Printable Perovskite Solar Cell Using a Thick Zirconia Layer," Energy Technol., vol. 5, pp. 1866−1872, 2017.

[96] L. K. Ono, M. R. Leyden, S. Wang, Y. Qi, "Organometal Halide Perovskite Thin Films and Solar Cells by Vapor Deposition," J. Mater. Chem. A, vol. 4, pp. 6693−6713, 2016.

[97] M. R. Leyden, Y. Jiang, Y. Qi, "Chemical Vapor Deposition Grown Formamidinium Perovskite Solar Modules with High Steady State Power and Thermal Stability," J. Mater. Chem. A, vol. 4, pp. 13125−13132, 2016.

[98] Y. Yao, W.-L. Hsu, M. Dagenais, "High-Efficiency Perovskite Solar Cell Based on Sequential Doping of PTAA," IEEE Journal of Photovoltaics, vol. 9, no. 4, 2019.

[99] Y. Yao, W.-L. Hsu, M. Dagenais "High Efficiency Perovskite Solar Cells by a Modified Low-Temperature Solution Process Inter-Diffusion Method," 44th IEEE Photovoltaic Specialist Conference, 2017.

[100] W. Shockley, and H. J. Queisser, " Detailed Balance Limit of Efficiency of p-n Junction Solar Cell," Journal of Applied Physics, vol. 32, no. 3, pp. 510, 1961.

[101] X. Ke, J. Yan, A. Zhang, B. Zhang, and Y. Chen, "Optical band gap transition from direct to indirect induced by organic content of $CH_3NH_3PbI_3$ perovskite films," Applied Physics Letter, vol. 107, no. 9, 2015.

[102] Y. Zhou, J. Kwun, H. F. Garces, S. Pang, N. P. Padture, "Observation of phase-retention behavior of the $HC(NH_2)_2PbI_3$ black perovskite polymorph upon mesoporous TiO_2 scaffolds," Chem. Commun., vol. 52, pp. 7273−7275, 2016.

[103] C. Yi, J. Luo, S. Meloni, A. Boziki, N. Ashari-Astani, C. Gratzel, S. M. Zakeeruddin, U. Rothlisberger, M. Gratzel, "Entropic stabilization of mixed A-cation ABX3 metal halide perovskites for high performance perovskite solar cells," Energy Environ. Sci., vol. 9, pp. 656-662, 2016.

[104] Fusheng Ma, Jiangwei Li, Wenzhe Li, Na Lin, Liduo Wang and Juan Qiao, "Stable α/δ phase junction of formamidinium lead iodide perovskites for enhanced near-infrared emission," Chem. Sci., vol. 8, pp. 800, 2017.

[105] X. Guo, C. McCleese, C. Kolodziej, A. C. S. Samia, Y. Zhao and C. Burda," Identification and characterization of the intermediate phase in hybrid organic–inorganic $MAPbI_3$ perovskite," : Dalton Trans., vol.45, pp. 3806, 2016.

[106] G. Murugadoss, S. Tanaka, G. Mizuta, S. Kanaya, H. Nishino, T. Umeyama, H. Imahori, and S. Ito," Light stability tests of methylammonium and formamidinium Pb-halide perovskites for solar cell applications," J. Journal of App. Phys., vol. 54, pp. 08KF08, 2015.

[107] Y. Yuan and J. Huang, "Ion Migration in Organometal Trihalide Perovskite and Its Impact on Photovoltaic Efficiency and Stability," Acc. Chem. Res., vol. 49, no. 2, pp. 286-293, 2016.

[108] K. Miyano, M. Yanagida, N. Tripathi, and Y. Shirai, "Hysteresis, Stability, and Ion Migration in Lead Halide Perovskite Photovoltaics," J. Phys. Chem. Lett., vol. 7, no. 12, pp. 2240-2245, 2016.

[109] Y, Zhou, F. Huang, Y. Cheng and A. Gray-Weale, “Numerical analysis of a hysteresis model in perovskite solar cells,” Comput. Mater. Sci., vol. 126, pp. 22-28, 2017.

[110] Y. Yuan and J. Huang, “Ion Migration in Organometal Trihalide Perovskite and Its Impact on Photovoltaic Efficiency and Stability,” Acc. Chem. Res., vol. 49, pp. 286−293, 2016.

[111] J. Xu et al., “Perovskite-fullerene hybrid materials suppress hysteresis in planar diodes,” Nat. Commun., vol. 6, pp. 7081, 2015.

[112] B. Chen, M. Yang, S. Priya, and K. Zhu,” Origin of J-V hysteresis in perovskite solar cells,” J. Phys. Chem. Lett. Vol. 7, no. 5, pp. 905-917, 2016.

[113] S. N. Habisreutinger, N. K. Noel, and H. J. Snaith, “Hysteresis index: a figure without merit for quantifying hysteresis in perovskite solar cells,” ACS Energy Lett. vol. 3, pp. 2472-2476, 2018.

[114] S. Ravishankar,S. Gharibzadeh, C. Roldán-Carmona, G. Grancini, Y. Lee, M. Ralaiarisoa, A. M. Asiri, N. Koch, J. Bisquert, and M. K. Nazeeruddin, “Influence of charge transport layers on opencircuit voltage and hysteresis in perovskite solar cells,” Joule, vol. 2, pp. 1-11, 2018.

[115] S. A. L. Weber, I. M. Hermes, S.-H. Turren-Cruz, C. Gort, V. W. Bergmann, L. Gilson, A. Hagfeldt, M. Graetzel, W. Tress and R. Berger,” How the formation of interfacial charge causes hysteresis in perovskite solar cells,” Energy Environ. Sci. vol. 11, pp. 2404-2413, 2018.

[116] H. Lin, M. Yang, X. Ru, G. W., S. Y., F. Peng, C. Hong, M. Qu, J. Lu, L. Fang, C. Han, P. Procel, O. Isabella, P. Gao, Z. Li and X. Xu, ” Silicon heterojunction solar cells with up to 26.81% efficiency achieved by electrically optimized nanocrystalline-silicon hole contact layers,” Nat. Energy, 2023.

[117] S. Albrecht and B. Rech, “Perovskite solar cells: On top of commercial photovoltaics,” Nat. Energy, vol. 2, no. 16196, 2017.

[118] A. R. Uhl, A. Rajagopal J. A. Clark, A. Murray, T. Feurer, S. Buecheler, A. K.-Y. Jen, H. W. Hillhouse, “Solution-Processed Low-Bandgap $CuIn(S,Se)_2$ Absorbers for High-Efficiency Single-Junction and Monolithic Chalcopyrite-Perovskite Tandem Solar Cells,” Advanced Energy Materials, vol. 8, no. 27, 2018.

[119] K. A. Bush, A. F. Palmstrom, Z. J. Yu, M. Boccard, R. Cheacharoen, J. P. Mailoa, D. P. McMeekin, R. L. Z. Hoye, C. D. Bailie, T. Leijtens, I. M. Peters, M. C. Minichetti, N. Rolston, R. Prasanna, S. Sofia, D. Harwood, W. Ma, F. Moghadam, H. J. Snaith, T. Buonassisi, Z. C. Holman, S. F. Bent and M. D. McGehee,” 23.6%-

efficient monolithic perovskite/silicon tandem solar cells with improved stability," Nat. Energy, vol. 2, no. 4, 2017.

[120] F. Sahli, J. Werner, B. A. Kamino, M. Br¨auninger, R. Monnard, B. Paviet-Salomon, L. Barraud, L. Ding, J. J. Diaz Leon, D. Sacchetto, G. Cattaneo, M. Despeisse, M. Boccard, S. Nicolay, Q. Jeangros, B. Niesen and C. Ballif, "Fully textured monolithic perovskite/silicon tandem solar cells with 25.2% power conversion efficiency," Nat. Mater., vol. 17, pp.820–826, 2018.

[121] B. Chen, Z. Yu, K. Liu, X. Zheng, Y. Liu, J. Shi, D. Spronk, P. N. Rudd, Z. Holman and J. Huang," Grain Engineering for Perovskite/Silicon Monolithic Tandem Solar Cells with Efficiency of 25.4%," Joule, vol. 3, no. 1, 2018.

[122] Q. Han, J. St-Yves, Y. Chen, M. Ménard, and W. Shi, "Polarization-insensitive silicon nitride arrayed waveguide grating," Opt. Lett., vol. 44, no. 16, pp. 3976-3979, 2019.

[123] T. Lang, J. He, J. Kuang, and S. He, "Birefringence compensated AWG demultiplexer with angled star couplers," Opt. Express, vol. 15, no. 23, pp. 15022-15028, 2007.

[124] S. Guerber, C. Alonso-Ramos, X. Le Roux, N. Vulliet, E. Cassan, D. Marris-Morini, F. Boeuf, and L. Vivien, "Polarization independent and temperature tolerant AWG based on a silicon nitride platform," Opt. Lett., vol. 45, no. 23, pp. 6559-6562, 2020.

[125] Y. Zhang, J. Zhan, S. Veilleux and M. Dagenais, "Arrayed Waveguide Grating with Reusable Delay Lines (RDL-AWG) for High Resolving Power, Highly Compact, Photonic Spectrographs," 2022 IEEE Photonics Conference (IPC), Vancouver, BC, Canada, 2022.

[126] Y. Zhang, P. Gatkine, S. Veilleux and M. Dagenais, "High Resolving Power and Highly Compact Arrayed Waveguide Grating with Reusable Delay Lines (RDL-AWG)," 2023 IEEE Silicon Photonics Conference, FC-4, Arlington, Virginia, Apr. 4-7, 2023

[127] Y. Zhang, W.-L. Hsu, P. Gatkine, S. Veilleux and M. Dagenais, "High Resolving Power Arrayed Waveguide Grating with Spiral Reusable Delay Lines (SRDL-AWG)," 2023 CLEO: Conference on Lasers and Electro-Optics, SW30.4, San Jose, California, May. 7-12, 2023.

[128] Y. Wang, S. Dong, Y. Miao, D. Li, W. Qin, H. Cao, L. Yang, L. Li, and S. Yin, "BCP as Additive for Solution-Processed PCBM Electron Transport Layer in Efficient Planar Heterojunction Perovskite Solar Cells," IEEE Journal of Photovoltaics, vol. 7, no. 2, 2017.

[129] H. Yoon, S. M. Kang, J.-K. Lee and M. Choi, “Hysteresis-free low-temperature-processed planar perovskite solar cells with 19.1% efficiency,” Energy Environ. Sci., vol. 9, pp. 2262, 2016.

[130] J. Huang, K.-X. Wang, J.-J. Chang, Y.-Y. Jiang, Q.-S. Xiao, Y. Li, “Improving the efficiency and stability of inverted perovskite solar cells with dopamine-copolymerized PEDOT:PSS as a hole extraction layer,” J. Mater. Chem. A, vol. 5, no. 26, 2017.

[131] C.-H. Chiang, Z.-L. Tseng, C.-G. Wu,” Planar heterojunction perovskite/PC71BM solar cells with enhanced open-circuit voltage via a (2/1)-step spin-coating process” J. Mater. Chem. A, vol. 2, pp. 15897-15903, 2014.

[132] A. Agresti, S. Pescetelli, B. Taheri, A. E. Del Rio Castillo, L. Cina, F. Bonaccorso, A. Di Carlo,” Graphene–Perovskite Solar Cells Exceed 18 % Efficiency: A Stability Study,” ChemSusChem, vol. 9, no. 18, 2016.

[133] Q.-D. Yang, J. Li, Y. Cheng, H.-W. Li, Z. Guan, B. Yu, S.-W. Tsang,” Graphene oxide as an efficient hole-transporting material for high-performance perovskite solar cells with enhanced stability,” J. Mater. Chem. A, vol. 5, pp. 9852-9858, 2017.

[134] J.-S. Yeo, R. Kang, S. Lee, Y.-J. Jeon, N. Myoung, C.-L. Lee, D.-Y. Kim, J.-M. Yun, Y.-H. Seo, S.-S. Kim, S.-I. Na,” Highly efficient and stable planar perovskite solar cells with reduced graphene oxide nanosheets as electrode interlayer,” *Nano Energy*, vol. *12*, no. 96, 2015.

[135] C. Sun, Z. Wu, H.-L. Yip, H. Zhang, X.-F. Jiang, Q. Xue, Z. Hu, Z. Hu, Y. Shen, M. Wang, F. Huang, Y. Cao, ”Amino‐Functionalized Conjugated Polymer as an Efficient Electron Transport Layer for Hig‐Performance Planar‐Heterojunction Perovskite Solar Cells,” Adv. Energy Mater., vol. 6, no. 5, 2016.

[136] E. Ramasamy, V. Karthikeyan, K. Rameshkumar, and G. Veerappan,” Glass-to-glass encapsulation with ultraviolet light curable epoxy edge sealing for stable perovskite solar cells,” Materials Letters, vol. 252, pp. 51-54, 2019.

[137] H. H. Jiun, I. Ahmad, A. Jalar, G. Omar, “Effect of wafer thinning methods towards fracture strength and topography of silicon die,”, Microelectron. Reliab., vol 46, no. 5-6, pp. 836-845, 2006.

[138] S. Gao, Z. Dong, R. Kang, B. Zhang, D. Guo, “Warping of silicon wafers subjected to back-grinding process,” Precis. Eng., vol. 40, pp. 87-93, 2015.

[139] F. Inoue, A. Jourdain, L. Peng, A. Phommahaxay, J. D. Vos, K. J. Rebibis, A. Miller, E. Sleeckx, E. Beyne, A. Uedono,” Influence of Si wafer thinning processes on (sub)surface defects,” Appl. Surf. Sci., vol. 404, no. 15, pp. 82-87, 2017.